Alma Mater Studiorum · Università di Bologna

Scuola di Scienze
Dipartimento di Fisica e Astronomia
Corso di Laurea Magistrale in Fisica

Study of the systematics on the precession frequency measurement at the Muon g-2 experiment at Fermilab

Relatore:

Prof. Stefano Zucchelli

Correlatore:

Prof. Marco Incagli

Presentata da:

Paolo Girotti

Sessione IV
Anno Accademico 2017/2018

Sommario

Il momento magnetico anomalo del muone $a_\mu = \frac{g-2}{2}$ è una delle quantità conosciute con più precisione nella fisica, sia sperimentalmente che teoricamente. L'alto livello di accuratezza permette l'uso della misura di a_μ come test del Modello Standard (MS). In particolare, qualsiasi deviazione dal valore teorico del MS potrebbe essere dovuto a contributi fisici Oltre il Modello Standard (BSM). Il notevole risultato ottenuto dall'esperimento E821 nel 2001 presso Brookhaven National Laboratory, con un valore misurato di $a_\mu = 11\,659\,208.0(6.3) \cdot 10^{-10}$ e una precisione complessiva di 0.54 parti per milione, ci ha lasciati con una differenza di 3.4 σ rispetto alla predizione del modello standard. Il nuovo esperimento *Muon g-2* (E989) presso Fermilab (FNAL) mira a ridurre l'errore sperimentale di un fattore 4, con un obiettivo finale di 0.14 ppm, utilizzando lo stesso anello di accumulazione e migliorando le incertezze statistiche e sistematiche. In circa 2 anni di presa dati sarà raggiunto un numero di decadimenti di muone 21 volte maggiore rispetto a E821, ottenendo un'incertezza statistica di 0.1 ppm. Al momento di questa scrittura, l'esperimento è operativo e ha già collezionato due volte la statistica totale di E821. Molti miglioramenti riguardanti i rivelatori implicano una riduzione dell'errore sistematico da 180 ppb a 70 ppb per la misura di ω_a, la frequenza di precessione anomala del muone. In particolare, il nuovo Sistema di Calibrazione Laser ridurrà l'errore sistematico dovuto alle fluttuazioni del guadagno dei fotomoltiplicatori al silicio (SiPM) da 120 ppb a 20 ppb.
Questa tesi descrive l'esperimento e poi discute due analisi effettuate da me utilizzando il Sistema di Calibrazione Laser. La prima è una sincronizzazione dei 1296 rivelatori al livello del nanosecondo, descritta nel capitolo 5. La seconda è uno studio sulla risposta del guadagno dei rivelatori a segnali che sono distanti meno di 100 ns, oltre alla valutazione del suo effetto nella misura di ω_a, descritto nel capitolo 6.

Abstract

The muon anomalous magnetic moment $a_\mu = \frac{g-2}{2}$ is one of the most precise quantity known in physics, experimentally and theoretically. The high level of accuracy permits to use the measurement of a_μ as an important test of the Standard Model (SM). In particular, any deviation from the SM theoretical evaluation could be due to Beyond Standard Model physics contribution. The impressive result obtained by the E821 experiment at Brookhaven National Laboratory in 2001, with a measured value of $a_\mu = 11\,659\,208.0(6.3) \cdot 10^{-10}$ and a total accuracy of 0.54 parts per million, left us with a 3.4 σ difference compared to the SM prediction. The new *Muon g-2* (E989) experiment at Fermilab (FNAL) aims to reduce the experimental error by a factor 4, with a final goal of 0.14 ppm, using the same storage ring and improving both the systematic and the statistical uncertainties. A number of muon decays 21 times higher with respect to BNL will be reached in about 2 years of data taking, improving the statistical uncertainty to 0.1 ppm. At the moment of this writing the experiment is fully operational and it has already collected 2 times the BNL statistics. Many improvements on the detectors involve a systematic error reduction from 180 ppb to 70 ppb for the measurement of ω_a, the anomalous precession frequency of the muon. In particular, the new Laser Calibration System will reduce the systematic error due to gain fluctuations of the silicon photo-multipliers (SiPM) from 120 to 20 ppb.
This thesis will describe the experiment and then discuss two analyses performed by me using the Laser Calibration System. The first is a time synchronization of the 1296 detectors at the nanosecond level, described in Chapter 5. The second is a study on the gain response of the detectors to signals closer than 100 ns in time, together with the evaluation of its effect in the ω_a measurement, described in Chapter 6.

Contents

Chapter 1

Introduction

1.1 The magnetic moment

The magnetic dipole moment $\vec{\mu}$ of an object is a measure of how much torque it experiences when placed in a magnetic field:

$$\vec{\tau} = \vec{\mu} \times \vec{B} \qquad U = -\vec{\mu} \cdot \vec{B} \tag{1.1}$$

It represents a correlation between the motion of its electric charge and the physical space that it occupies. A general expression of the magnetic moment is given by:

$$\vec{\mu} = \frac{1}{2} \int (\vec{r} \times \vec{J}(\vec{r}))dV \tag{1.2}$$

Assuming that the current is composed of a series of point charges with velocity $\vec{v}_i$ and charge q_i, we might rewrite the current distribution as

$$\vec{J} = \sum_i q_i \vec{v}_i \delta(\vec{r} - \vec{r}_i) \tag{1.3}$$

so that, using $\vec{L} = \vec{r} \times \vec{p}$,

$$\vec{\mu} = \frac{1}{2} \sum_i q_i (\vec{r}_i \times \vec{v}_i) = \frac{1}{2} \sum_i \frac{q_i}{m_i} \vec{L}_i \tag{1.4}$$

If all the particles are identical, the magnetic moment is proportional to the total angular momentum of the system $\vec{L} = \sum_i \vec{L}_i$

$$\vec{\mu} = \frac{q}{2m}\vec{L} \tag{1.5}$$

The dawn of the 20^{th} century was a period of strong innovation in the physics world. Names like Einstein, Schrödinger, Dirac, Pauli and Feynman, introduced a revolution in the way of understanding nature: the era of the atom and particle physics started. In 1922 the famous experiment by Stern and Gerlach showed that a beam of identical silver atoms passing through a magnetic field [1] emerged from it physically separated into two different bands along the axis of the magnetic field. What should be inferred by this result is that silver atoms have two possible magnetic moments, equal in magnitude but pointing to opposite directions. One possible source to this magnetic moments could be the electric charge of the nucleus that implies a scaling factor of $1/m_N$, where m_N is the mass of the nucleus. This scaling is not observed in silver and hydrogen experiments. This moved the interest to the orbiting electron in the atom as the possible culprit.

From spectroscopy experiment what came out was that a fourth quantum number, in addition to n, m and l introduced by quantum mechanics, was necessary to remove all the degeneracies in the experimental data. There was a big effort to explain data using different models (e.g Sommerfeld and Lande's *Ersatzmodel*), which were only able to describe just some specific situations. The first solution to this problem, even if only qualitatively, was given by two young physicists, Samuel Goudsmith and George Uhlenbeck, where the idea of the spin with its value of $\pm\frac{1}{2}$ came out. Quantitatively the classical equation of the magnetic moment Eq. 1.5 underestimates the result of experiments like the Stern-Gerlach by a factor 2. The common practice to solve this problem was to incorporate this factor via the Lande *g-factor* or *gyromagnetic ratio*

$$\vec{\mu} = g\frac{q}{2m}\vec{S} \tag{1.6}$$

where g=1 for a classical system and g=2 referring to the electron.

The breakthrough in the mathematical description of spin came in 1928 from Dirac's attempts to create a relativistic extension of Schrödinger's equation that, unlike the Klein-Gordon equation, preserved linearity with respect to time. Existence of spin was therefore predicted together with the existence of anti-particles as a result of Dirac's solution. Furthermore, the equation predicted the correct magnetic moment for the

electron with g=2, even when Dirac's equation is taken to the non-relativistic limit:

$$\left(\frac{1}{2m_e}(\vec{P}+q\vec{A})^2+\frac{q}{2m_e}\vec{\sigma}\cdot\vec{B}-qA^0\right)\Psi_A=(E-m_e)\Psi_A \tag{1.7}$$

Comparing the term proportional to $\vec{B}$ to the equation 1.1

$$U=-\vec{\mu}\cdot\vec{B}=\frac{q}{2m_e}\vec{\sigma}\cdot\vec{B} \tag{1.8}$$

we have

$$\mu=-\frac{q}{2m_e}\vec{\sigma}=-2\frac{q}{2m_e}\vec{S} \tag{1.9}$$

so that $g=2$ (Eq. 1.6).

1.1.1 The anomalous magnetic moment

Given the success in Quantum Mechanics in predicting g to be 2 for the half-integer spin electron, it was natural to assume that the half-integer spin proton would also be a Dirac particle with $g\equiv 2$. Nevertheless, in 1933 Estermann and Stern [2] experimentally found a value of 5.6 for the g-factor of the proton. Shortly thereafter, Rabi measured the magnetic moment of the deuteron and from that a g-factor of 3.8 could be inferred for the neutron. Of course, it is now known that the neutron and proton are composite particles containing moving, fractionally-charged quarks: with the current loops induced by the quarks it is no wonder that the magnetic moment for nucleons deviates strongly from the prediction for a point-like particle.

If it were not for the quantum world of virtual particles, the g-factor of the electron would be identically 2 and any deviation would be a strong indication of internal structure, as in the proton and neutron. However, the magnetic moment cannot be measured without the influence from virtual exchanges made explicit in quantum field theories. All particles are shrouded in a cloud of virtual particles pulled from the vacuum. The screening effect of the virtual particles leads to a slight change (anomaly) in the observed magnetic moment from what would be expected for a bare particle. The extent to which g differs from 2 is called the anomalous magnetic moment and is conventionally written as a fractional deviation:

$$a_e=\frac{g-2}{2} \tag{1.10}$$

The first evidence of this anomaly is due to Kusch and Foley [3] who measured in 1948 a

value of $a_e = 0.00119(5)$, giving no space to doubt in the result given such a small error. At about the same time, quantum electrodynamics (QED) was reaching a turning point. For almost two decades, QED had been impeded by the problem that any attempt to calculate measurable physical properties resulted in non-convergent infinite series. The solution of renormalization was proposed by Feynman, Schwinger, and Tomonaga, and by the end of 1948 Schwinger had calculated [4] the first-order correction to the magnetic moment to yield $a_e = \frac{\alpha}{2\pi} = 0.00116$, which is within the quoted error of the Kusch and Foley experiment. The complete QED calculation is a sum over terms of the fine structure constant $\alpha = 2\pi q^2/hc$. The most recent calculation comes from the computation of the fifth order in α [5, 6]

$$\begin{aligned} a_e^{th}(2017) =& 0.5\left(\frac{\alpha}{\pi}\right) - 0.328478965579\left(\frac{\alpha}{\pi}\right)^2 + 1.181241456\left(\frac{\alpha}{\pi}\right)^3 - 1.912245764\left(\frac{\alpha}{\pi}\right)^4 \\ &+ 6.599(223)\left(\frac{\alpha}{\pi}\right)^5 + 1.74(2)\cdot 10^{-12} = 0.001\,159\,652\,182\,031\,(720) \end{aligned} \tag{1.11}$$

The last term arises from the exchange of heavier particles from the hadronic and electroweak sectors. The experimental measurement on a_e has reached an incredible precision of 4 ppb even compared to the amazing precision obtained in the theoretical calculation of 20 ppb. The experimental setup used at Washington, by H. Dehmelt and his group [7], consist of a Penning trap and they were able to obtain the values of

$$\begin{aligned} a_{e+}^{exp} &= 0.0011596521884(43) \\ a_{e-}^{exp} &= 0.0011596521879(43) \end{aligned} \tag{1.12}$$

with a difference between the theoretical and the experimental value of the electron anomaly at the 1.7σ level. Table 1.1 shows the measured values of the g-factor for different particles, as well as the theoretical calculation as of 2017.

Particle	Experimental value	Precision	Ref.	Theoretical prediction	Ref.
Electron	2.0023193043738(82)	$4 \cdot 10^{-12}$	[8]	2.002319304364(2)	[6]
Muon	2.0023318418(13)	$6 \cdot 10^{-10}$	[10]	2.0023318338(14)	[11]
Tau	2.008(71)	$4 \cdot 10^{-2}$	[12]	2.0023546(6)	[13]
Proton	5.585694674(58)	$1 \cdot 10^{-8}$	[8]	5.58	[14]
Neutron	-3.8260854(10)	$3 \cdot 10^{-7}$	[8]	-3.72	[14]

Table 1.1: Experimental and theoretical values of g for various particles.

Property	e	μ	τ
Charge	-1	-1	-1
Spin	1/2	1/2	1/2
Mass	0.511 MeV/c^2	105.7 MeV/c^2	1776.9 MeV/c^2
Lifetime	$> 2.0 \cdot 10^{36}$ s	$2.2 \cdot 10^{-6}$ s	$290.3 \cdot 10^{-15}$ s
Main decay mode	-	$\mu \to e\bar{\nu}_e\nu_\mu$	$\tau \to \mu\bar{\nu}_\mu\nu_\tau$
Branching ratio	-	$\sim 100\%$	17.39%

Table 1.2: Lepton properties

1.2 The muon

The muon is usually considered as a heavier version of the electron. Both particles are charged leptons: the lepton universality dictates that they are identical except for mass and the fact that muons are intrinsically unstable. Together with the tauon, they complete the charged lepton family. Table 1.2 enumerates lepton properties compiled by the Particle Data Group [8].

1.2.1 Decay chain

The pion decay chain is commonly used to produce muons. The pion is the lightest of all hadronic matter and is produced in copious numbers when an energetic proton beam impacts a high Z target. The pion is a meson, so the two constituent quarks inside the pion are able to annihilate and still conserve color. When the quarks in a charged pion annihilate, the net charge must be conserved, so the W is the only possible propagator. The final state must also have a net charge, and since the mass of the parent pion is 140 MeV, the only possibilities are to have a muon or an electron contained in the final state. While a less massive final state is preferred due to phase space considerations, parity violation of the weak force enhances the decay into a muon and a neutrino [8]:

$$R_\pi = \frac{\Gamma(\pi \to \mu + \nu_\mu)}{\Gamma(\pi \to e + \nu_e)} = 8.1 \cdot 10^3 \tag{1.13}$$

so that the probability of having a muon in the final state is $> 99.9\%$ To understand this phenomenon pictorially Fig. 1.1 shows the π^- decay in the rest frame of the pion. In this frame, the anti-neutrino and the lepton are emitted back-to-back. In the limit of massless neutrinos, the anti-neutrino is always emitted with a right-handed helicity. Since the pion has zero spin, to conserve total angular momentum the lepton must also be right-handed. In the weak decay, both the electron and the muon prefer to be left-

handed. Since this option is essentially vetoed by the nearly massless neutrino, the more massive muon is heavily favored by the weak decay. The decay lends itself to production

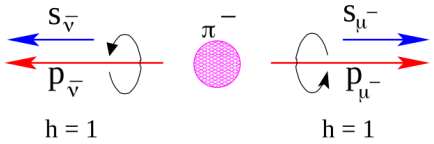

Figure 1.1: Diagram depicting the pion decay in the rest frame, with helicity constraints.

of spin polarized muons. When the isotropic decay is boosted into the lab frame for a pion beam, both the highest energy (forward decay) or lowest energy (backward decay) muons exhibit strong spin polarization. As such momentum selection can be used to achieve a highly polarized muon beam.

After the pion decay, the produced muons decay similarly into an electron and two neutrinos with nearly 100% probability. The decay chains are:

$$\pi^+ \rightarrow \mu^+ \bar{\nu}_\mu \qquad \pi^- \rightarrow \mu^- \nu_\mu \tag{1.14}$$

$$\mu^+ \rightarrow e^+ \bar{\nu}_e \nu_\mu \qquad \mu^- \rightarrow e^- \nu_e \bar{\nu}_\mu \tag{1.15}$$

As in the case of pion decay, parity violation plays an important role also here. In the rest frame of the muon, the highest energy decay electrons come from decays in which the neutrinos are emitted collaterally, as depicted in Fig. 1.2. In this scenario, half of the initial rest mass of the muon is carried away by the decay electron ($E_{max} \approx 53$ MeV), while the other 53 MeV is shared by the two neutrinos. Since the neutrino and anti-neutrino are traveling in the same direction, and the weak decay dictates they must have opposite helicities, their spins must be opposite. With the neutrino's spins canceling, conservation of angular momentum forces the decay electron to carry the spin of the parent muon. The $V - A$ nature of the weak decay prefers to couple to a left-handed electron, so the high energy decay electron depicted in Fig. 1.2 tends to be emitted with its momentum opposite to its spin. Therefore, in the rest frame of the muon, the spin direction of the muon can be monitored by observing the instantaneous direction at which the high energy decay electrons are emitted. A common framing for discussions of muon decay is the differential decay rate, $n(y)$, and asymmetry function, $a(y)$, over the range of possible muon energies, $y = E/E_{max}$ [15]. The differential decay rate, also called the Michel Spectrum, is a proxy for the overall probability of a decay electron with the energy y. The asymmetry function represents the likelihood of the decay electron momentum being in the direction of the muon spin. Both functions are normalized to

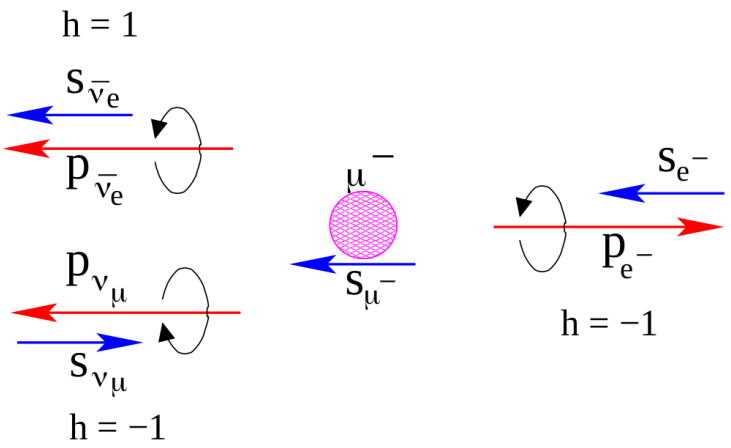

Figure 1.2: Helicity constraints in the muon decay when the neutrinos are emitted in the same direction.

have a maximum value of one. The decay functions for the muon rest frame in Eq. 1.16, and the corresponding plots are shown in Fig. 1.3.

$$n_{rest}(y) = y^2(3-2y) \qquad a_{rest}(y) = \frac{2y-1}{3-2y} \tag{1.16}$$

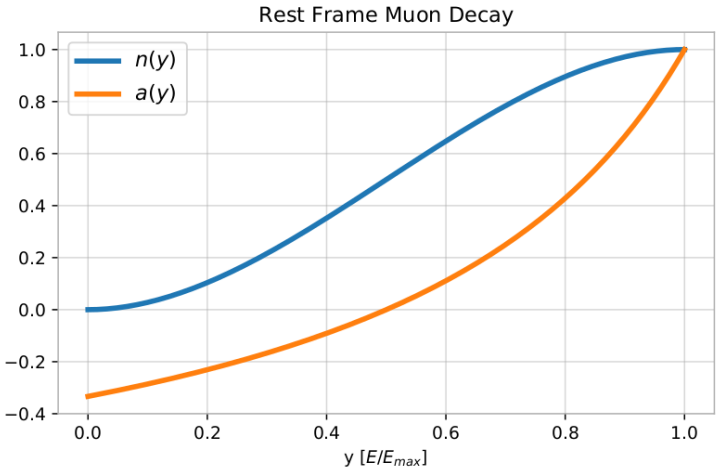

Figure 1.3: Decay rate, $n(y)$, and decay asymmetry, $a(y)$, of the muon decay in the rest frame. Here $y = E/E_{max}$, where $E_{max} = 53$ MeV.

1.3 Why a_μ?

The motivation for a muon $g-2$ experiments comes from various reasons. First of all, a_μ is a relatively simple observable to measure: the experimenters need a spin polarized beam of leptons, an external magnetic field, and a technique to determine the spin direction. Then, as mentioned before, a precise measurement of a_μ probes into all the virtual interactions between the lepton and the vacuum. The whole Standard Model contributes to its value, since the interactions involve Quantum Electrodynamics (QED), Electro-Weak theory (EW), and Quantum Chromodynamics (QCD). It traverses the entirety of Standard Model interactions aside from gravity. Moreover, eventual measurements that differ from the SM theoretical prediction points toward *new physics*, helping theorists to discern between the multitude of Beyond Standard Model (BSM) theories and to set new physics constraints.

Why muons?

To understand why such a measurement using muons is important, there are physical and practical considerations. The physics considerations weigh in with the desire for sensitivity to small effects predicted by the Standard Model. The electron g–2 has already been measured with around 2,000 times more precision [16], so why not just measure a_e even more precisely? Well, simply put the physics contributions for a_e and a_μ are just different. Higher order interactions with particles of larger masses contribute with mass suppression terms, $\propto (\frac{m_l}{M})^2$, or possibly even higher. These interactions mostly manifest in the EW and QCD sector. The relative mass ratio between the electron and the muon enhances the sensitivity to these terms by a factor of $(\frac{105.66}{0.511})^2 \approx 43000$ [17]! Even though a_e can be measured to much higher precision, a_μ is still around 2000 times more sensitive to large mass contributions. To that end, the electron $g-2$ is a deeper probe of QED and the muon $g-2$ is a more rounded probe of the SM. The preceding argument raises a further question though: "Why not use the τ?". The answer is really a practical consideration; the ephemeral tauon has a lifetime of only 0.29 fs compared to 2.2 μs for the μ [8]. The τ also has many decay modes rather than a single dominant one like the muon. While the τ particle would be appealing if a significant enough Lorentz boost could be achieved and a clean method to understand the decay modes was presented, an experiment using tauons is simply not practical with current technology.

1.4 State of the theory

As anticipated in section 1.1.1, the value of a_μ arises from the exchange of virtual particles. The contributions that affect this value come from many sectors of theory, that are Quantum ElectroDynamics (QED), ElectroWeak theory (EW), and Quantum ChromoDynamics (QCD), with the latter further divided into three classes. The lowest-order contribution arises from Hadronic Vacuum Polarization (HVP). Higher-Order contributions (HOHVP) contain an HVP insertion along with an additional loop. The last class is Hadronic Light-By-Light (HLBL) scattering.

$$a_\mu^{SM} = a_\mu^{QED} + a_\mu^{EW} + a_\mu^{HVP} + a_\mu^{HOHVP} + a_\mu^{HLBL} \tag{1.17}$$

As seen in Table 1.3 the dominant contribution comes by far by QED, being nearly two million times the experimental error. Note that the error on the Standard Model comes almost entirely from the hadronic terms.

Term	Value $(\cdot 10^{-11})$
a_μ^{QED}	$116\,584\,718.951 \pm 0.080$
a_μ^{EW}	154 ± 1
a_μ^{HVP}	$6\,949 \pm 43$
a_μ^{HOHVP}	-98.4 ± 0.7
a_μ^{HLBL}	105 ± 26
Total SM	$116\,591\,827 \pm 37$

Table 1.3: Standard model contributions to a_μ [18, 19, 20].

1.4.1 QED term

The QED contribution to a_μ can be evaluated by the perturbative expansion in α/π:

$$a_\mu(QED) = \sum_{n=1}^{\infty} \left(\frac{\alpha}{\pi}\right)^n a_\mu^{(2n)} \tag{1.18}$$

where $a_\mu^{(2n)}$ is finite thanks to the renormalizability of QED. Some examples of fourth and fifth-order QED contributions are shown in Fig. 1.4. The full QED contribution has been fully calculated out to terms of order α^5 (using more than 10'000 diagrams!)

yelding [18]

$$a_\mu^{QED} = 0.5\left(\frac{\alpha}{\pi}\right) + 0.765857425(17)\left(\frac{\alpha}{\pi}\right)^2 + 24.05050996(32)\left(\frac{\alpha}{\pi}\right)^3 + 130.8796(63)\left(\frac{\alpha}{\pi}\right)^4 + 753.29(1.04)\left(\frac{\alpha}{\pi}\right)^5 = 116\,584\,718\,951(19)(7)(77)(9)\cdot 10^{-14} \quad (1.19)$$

where the errors results mainly from the uncertainty in α, which is:

$$\alpha^{-1} = 137.035\,999\,049(90) \rightarrow 0.66 ppb \quad (1.20)$$

obtained from the precise measurement of the recoil velocity of Rubidium h/m_{Rb}, the Rydberg constant and m_{Rb}/m_e [21, 22].

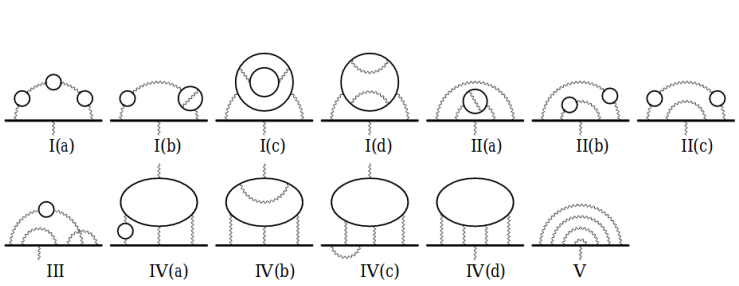

(a)

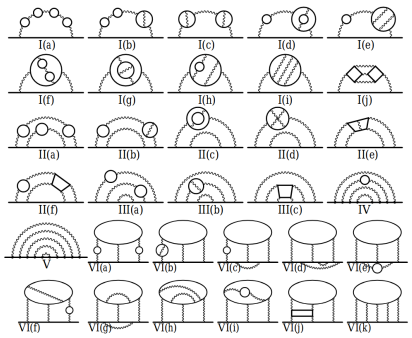

(b)

Figure 1.4: Vertex diagrams representing 13 (a) and 32 (b) gauge-invariant subsets contributing to the lepton $g-2$ for QED at the eighth (a) and tenth (b) order. Solid and wavy lines represent lepton and photon lines, respectively.

1.4.2 EW term

The corrections due to the weak force are mass suppressed compared to the QED contribution. The lowest order and largest contribution to the weak corrections are represented by the two diagrams pictured in Fig. 1.5. The diagram on the left is similar to the Schwinger diagram, but with a Z (or Higgs) boson propagating instead of a photon. The single loop contributions first calculated in 1972 [23] yield

$$a_\mu^{EW}(1-loop) = 194.8\cdot 10^{-11} \quad (1.21)$$

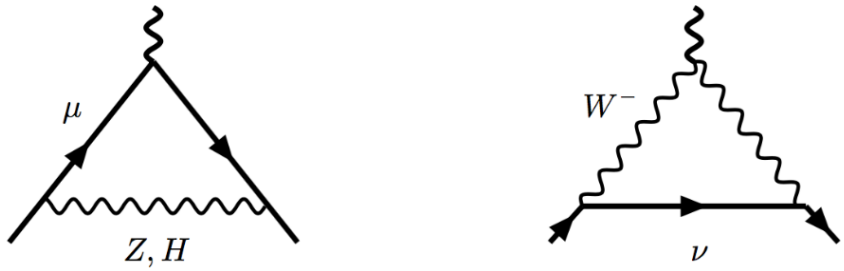

Figure 1.5: The largest contributing diagrams from the weak interaction.

The term containing the W boson contribution is suppressed by a term $(m_\mu/M_W)^2$ with respect to the QED contribution, so that it introduces a perturbation of approximately 3.3 ppm. On the other way, the single loop with an exchange of a Z boson reduces the overall EW contribution with a negative perturbation of -1.6 ppm, while the remaining loop with an Higgs boson ($M_H \sim 125$ GeV) doesn't contribute significantly due to the mass suppression. The total contributions from the second order weak corrections sum up to $-40 \cdot 10^{-11}$ [17], so that the overall EW term is [24]

$$a_\mu^{EW} = 154(1) \cdot 10^{-11} \tag{1.22}$$

where the error comes mostly from hadronic loop uncertainties.

1.4.3 QCD terms

QCD terms are the ones with the higher uncertainty due to the non-perturbative regime of this process. Since it dominates the uncertainty on a_μ with a contribution of about 60 ppm (Table 1.3), improvements in this sector are crucial.

Hadronic Vacuum Polarization

The general form of Hadronic Vacuum Polarization (HVP) is quite similar to the QED one. The muon radiates a photon or another boson, that creates a particle pair that annihilates before recapture with the muon, as seen in Fig. 1.6. The difference with QED is that the particle pair is composed of hadronic matter, such as π^0, $\pi^\pm$, ρ^0, etc. These loop terms can be calculated relating to the cross section of hadron production

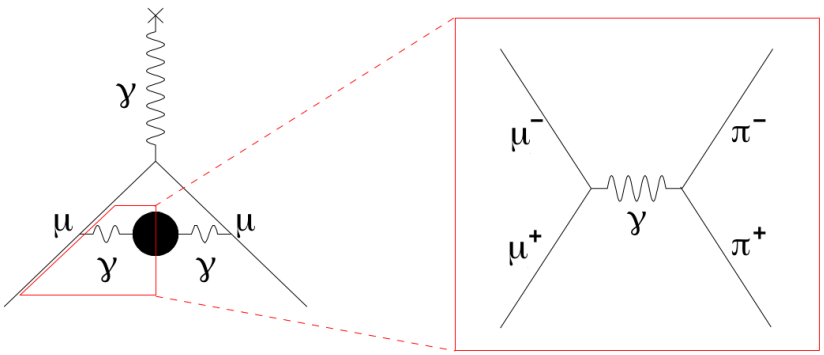

Figure 1.6: The Feynman diagram on the left shows the lowest-order Hadronic Vacuum Polarization (HVP), where the black circle represents any possible combination of quark matter.

from the annihilation of e^+e^-, using the dispersion relation

$$a_\mu^{HVP} = \frac{1}{3}\left(\frac{\alpha}{\pi}\right)^2 \int_{4m_\pi^2}^{\infty} \frac{\mathrm{d}s}{s} \frac{\sigma_{e^+e^-\to hadrons}(s)}{\sigma_{e^+e^-\to\mu^+\mu^-}(s)} K(s) \tag{1.23}$$

In the last years several determination where obtained for the hadronic vacuum polarization which used the same data set with different data treatment, obtaining two leading values:

$$a_\mu^{HVP}[25] = 6923(42)\cdot 10^{-11} \tag{1.24}$$
$$a_\mu^{HVP}[20] = 6949(43)\cdot 10^{-11} \tag{1.25}$$

The total contribution from higher-order hadronic loops is calculated to be [20]

$$a_\mu^{HOHVP} = -98.4 \pm 0.7 \cdot 10^{-11} \tag{1.26}$$

Hadronic Light-by-Light

The general form for hadronic light-by-light (HLbL) contains more interaction vertices than HVP and, therefore a smaller contribution to the total muon anomaly. The propagating muon interacts with three photons and those photons interact with a QCD loop which interacts with the external field. The HLbL scattering differs from other hadronic contributions in that it cannot be related to experiments, so it must be estimated from a model. Several evaluations have taken place, with the "best estimate" value currently

accepted of [20]

$$a_\mu^{HLbL} = 105(26) \cdot 10^{-11} \tag{1.27}$$

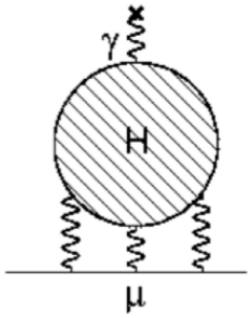

Figure 1.7: Feynman diagram for the general case of hadronic light-by-light scattering.

1.4.4 The standard model prediction for a_μ

Combining all of the various contributions explained in the previous sections and listed in Table 1.3, the current total prediction for the muon's anomalous magnetic moment is

$$a_\mu^{SM} = 116\,591\,827 \pm 37 \cdot 10^{-11} \tag{1.28}$$

The current very precisely known experimental value was measured by the BNL-E821 experiment, as described in the section 2.2 [10]:

$$a_\mu^{exp}(2006) = 116\,592\,080(63) \cdot 10^{-11} \tag{1.29}$$

The total uncertainty includes a 0.46 ppm statistical uncertainty and a 0.28 ppm systematic uncertainty, combined in quadrature. This value was obtained averaging the two results coming from the measurement of the negative and positive muon, which were in agreement, as predicted by the CPT theorem [26]. This experimental value has to be compared with the SM value shown in Eq. 1.28. The difference between the experimental and the theoretical values gives

$$a_\mu^{BNL} - a_\mu^{SM} = 253 \pm 73 \cdot 10^{-11} \tag{1.30}$$

This is a difference of $\sim 3.5\sigma$, and while it does not reach the 5σ threshold usually used to claim a discovery, it tells us that maybe something is hiding there. The next step is

to push the precision even further on both fronts, and turn a statistical tension into a $> 5\sigma$ discovery (assuming constant central values). The new Muon $g-2$ experiment (E989) described in chapter 3 now in operation at Fermilab (FNAL) aims to push the experimental uncertainty from 0.54 ppm of BNL to 0.14 ppm, bringing the discrepancy to $\sim 7\sigma$ if the center value is confirmed.

1.5 Going Beyond Standard Model

Although the SM is a very well established renormalizable Quantum Field Theory (QTF) that can describe essentially all experimental data of laboratory and collider experiments, it is known that the SM is not able to explain a number of fundamental facts. Some of them are:

- the existence of non-baryonic cold dark matter;
- the matter-antimatter asymmetry in the universe;
- the presence of a cosmological constant.

Moreover, a complete theory (*of everything*) should also include the force of gravity in a natural way and explain the difference between the weak and the Planck scale (hierarchy problem). If we confront an accurately predictable observable with a sufficiently precise measurement of it, we should be able to see that our theory is incomplete. New Physics can manifest itself through states or interactions which have not been seen by other experiments, either by a lack of sensitivity or, because the new state was too heavy to be produced at existing experimental facilities or, because the signal was still buried in the background [17].
The anomalous magnetic moment of the muon provides one of the most precise tests of Quantum Field Theory as a basic framework of elementary particle theory and of QED and EW in particular. But not only that, it also constrains Physics beyond the SM severely [17]. The comparison of theoretical and experimental values for a_μ is interesting, regardless of the outcome. If the values differ, then the comparison provides evidence for Physics beyond the Standard Model. If they agree, then the result constrains any proposed speculative extension, assuming that there are no fine-tuned cancellations between different varieties of New Physics.

Considering the simplest extensions of the Standard Model, we can write another

contribution to the anomalous magnetic moment, including a generic BSM contribution:

$$a_\mu = a_\mu^{SM} + a_\mu^{BSM} \tag{1.31}$$

The corrections are proportional to $\left(\frac{m_\mu}{M}\right)^2$, where M is the mass of the new particle, and m_μ the one of the muon. Therefore, the measure is sensitive to new particles in the mass range from 100 MeV to 1 TeV with a precision better than the experiment at LHC due to a much lower background.

Supersimmetry

Supersimmetry (SUSY) is a proposed theory that could account for the deviation in a_μ. It postulates the existence of a symmetry between bosons and fermions: each boson has a fermion partner and viceversa. This new partner particles are labeled using a *s-* as a prefix for fermions having *squarks* and *sleptons*, while the suffix *-ino* is used for bosons: so photon becomes *photino* and so on. Another effects of supersymmetry is that this theory leads to two Higgs doublets [17]: one gives mass to the upper half of each generation (u, c, t quarks) and the other gives mass to the lower half (d, s, b quarks). Of this four states, two are electrically neutral, one is positive and the other is negative. The contributions from this theory arise through diagrams containing loops with smuon-neutralino and sneutrino-chargino conversions, as shown in Fig. 1.8. The $\tilde{\chi}^0$

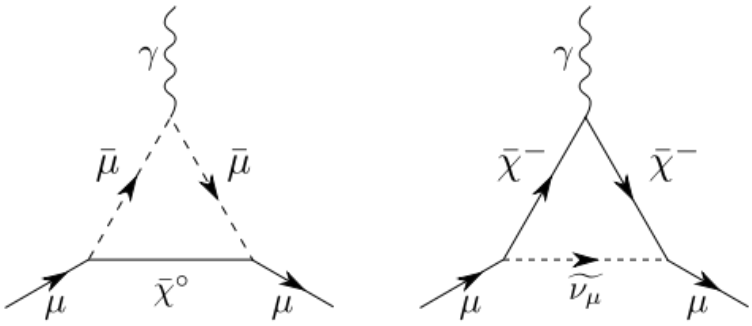

Figure 1.8: Feynman diagrams for the lowest-order supersymmetric interactions contributing to a_μ. $\bar{\mu}$ is a smuon, $\tilde{\nu}$ is a sneutrino and $\bar{\chi}^{0,\pm}$ is the neutralino/chargino.

and $\tilde{\chi}^\pm$ are called *neutralino* and *chargino* respectively: these are the mass eigenstates whose linear combinations give *photino*, *wino*, *zino* and *Higgsino*. A general expression for contributions from SUSY is given in Eq. 1.32 [27].

$$|a_\mu^{SUSY}| \approx 130 \cdot 10^{-11} \left(\frac{100\ \text{GeV}}{\tilde{m}}\right)^2 \tan(\beta) \tag{1.32}$$

The $\tan(\beta)$ enhancement can naturally be around 40 or 50. The difference $a_\mu^{exp} - a_\mu^{SM} \approx 250 \cdot 10^{-11}$ (Eq. 1.30) puts the mass scale at $\tilde{m} \approx 500$ GeV for a SUSY effect the size of the entire muon anomaly discrepance.

Dark photon

A recent BSM scenario involves the so called "dark photon", an hypothetical relatively light vector boson from the dark matter sector that express its interaction with ordinary matter through mixing with the ordinary photon [28, 29]. The strength of the coupling is expressed as ϵe, where ϵ is the kinetic mixing term between ordinary and dark photon. This boson with mass m_V give rise to a contribution to a_μ:

$$a_\mu^{DARK\gamma} = \frac{\alpha}{2\pi}\epsilon^2 F(m_V/m_\mu) \tag{1.33}$$

where the form factor F equals to unity if $m_V \ll m_\mu$, and is equal to $\frac{2m_\mu^2}{3m_V^2}$ if $m_V \gg m_\mu$. A viable solution to the muon $g-2$ discrepancy could be provided by the dark photon if $\epsilon \sim 10^{-3}$ and $m_V \sim 10 - 100$ MeV. Searches for a dark photon in this mass range are currently underway at flavor factories and dedicated experiments at CERN (NA48 and NA62), the Jefferson Lab and MAMI in Mainz, and PADME in Frascati.

More BSM

The two BSM models presented here are by no means the only possible *new physics* scenarios. Many other SM extensions have been proposed throughout the years, including Muon compositeness, Electric Dipole Moment (EDM), leptoquarks, extra dimensions, and so on. Deeper discussions on many possible explanations to the a_μ discrepancy are presented in [15, 17, 27].

Chapter 2

The history of muon g-2 experiments

In the middle of 20^{th} century there was a growing interest on the muon. The results obtained for the neutron and proton g-2 can elicit that also a muon could have an internal structure because of its larger mass with respect to the electron. Muons have a lifetime $\tau_\mu = 2.2\ \mu s$ which makes it difficult to store them and analyze their spin. From the discovery of parity violation in 1957 [30, 31], it was understood that muons produced from pion decay are naturally polarized, providing a natural source of polarization for the experiment with muons. As another consequence of parity violation, the decaying of high energy electrons from a polarized muon source is preferentially in the same direction of the muon spin, providing a way to determine the spin direction of the muons as a function of time with a counting experiment. Counting the number of decay electrons and applying an energy threshold, the fixed detector will measure a distribution in time of the following form

$$N(t) = N_0 e^{-t/\tau}[1 + A\cos(\omega_a t + \phi)] \tag{2.1}$$

where N_0 is the total population at time $t = 0$, τ is the muon lifetime, the value of A represents the asymmetry in the direction of the decaying particle, ω_a represents the anomalous precession frequency and the phase ϕ depends on the initial polarization of the muon beam. Moreover, sensitivity to exchange with heavy particles scales with the square of the leptons mass, giving to the muon an amplification factor of $\left(\frac{m_\mu}{m_e}\right)^2 = 4 \cdot 10^4$ relative to the electron, thus increasing the sensitivity to new physics.

The first muon experiment was performed in 1957 by Garwin and collaborators at the Nevis cyclotron of the Columbia University [32]. Muons formed in flight from pion decays were stopped in a carbon target after passing one at time through an entrance counter. An external magnetic field applied to the target region causes the spin of the muon to precess. The precession could be increased or decreased tuning the magnitude of the external field. This experiment was able to determine a value for $g = 2.00 \pm 0.10$ for the muon, plotting the counts measured from the fixed counter as a function of the magnetic field following Eq. 2.2:

$$\omega_s = g\frac{eB}{2mc} \tag{2.2}$$

as shown in Fig. 2.1 (a).

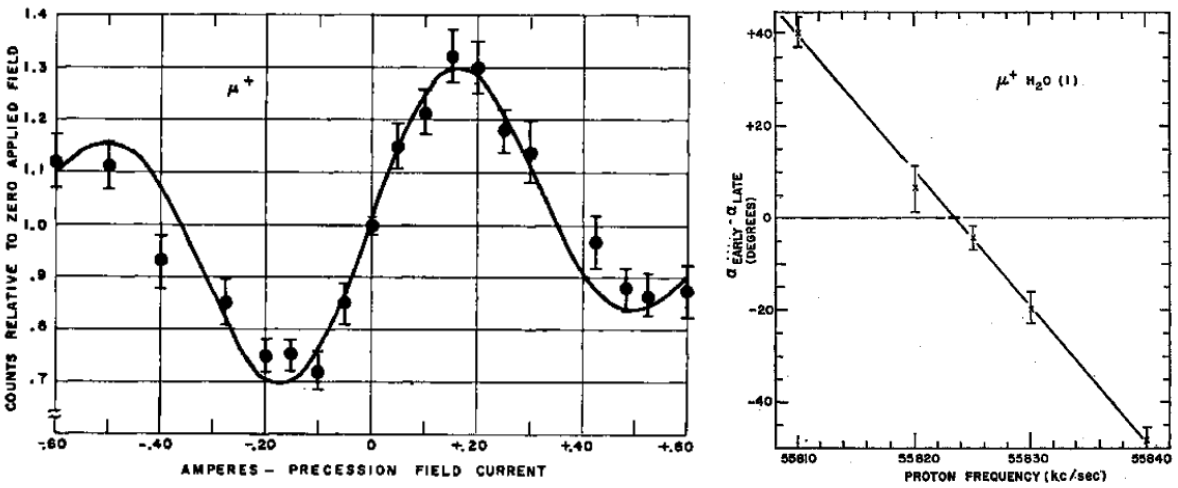

(a) Garwin data (b) Hutchinson data

Figure 2.1: Historical plots showing Larmor precession data from the Garwin (a) and Hitchinson (b) experiments used to determine the muon *g-factor*.

The precision obtained with this experiment was not sufficient to measure anomalous contributions to g. Similar experiments continued during the next years with the aim to improve the precision of this measurement. The highest precision was obtained by Hutchinson and collaborators in 1963 [33] by stopping muons in a magnetic field and measuring the early-to-late phase difference between a standard reference and peaks in the decay electron distribution (Eq. 2.1). In Fig. 2.1 (b) it is shown the final result of the measurement of the Larmor precession frequency plotting the phase difference at a fixed time interval as a function of the reference clock and fitting for the zero crossing. In

this experiment the magnetic field was measured via nuclear magnetic resonance (NMR) in terms of the Larmor precession frequency of protons in a polarized water sample, so it easier to express the results as a ratio λ of the two frequencies or magnetic moments obtaining

$$\lambda = \frac{\omega_\mu}{\omega_p} = \frac{\mu_\mu}{\mu_p} = 3.18338(4). \tag{2.3}$$

Using this result is possible to obtain a direct test with the QED prediction from Eq. 2.2.

2.1 Experiments at CERN

Before Hutchinson published his results on the Larmor precession frequency a new experimental procedure was studied at CERN to increase the precision of the g-2 measurement, following the principles used in the determination of the electron's anomalous magnetic moment [34]. A charged particle moving in a uniform magnetic field B will execute a circular motion with a cyclotron frequency

$$\omega_c = \frac{eB}{mc} \tag{2.4}$$

It appears clear that taking the ratio ω_s/ω_c the spin precession of muons moving into this magnetic field develops $1 + a_\mu$ times faster than the momentum vector. Taking the difference between the two frequencies the result is the *anomalous precession frequency* defined as

$$\begin{aligned} \omega_a = \omega_s - \omega_c &= \frac{eB}{mc}\left(\frac{g}{2} - 1\right) \\ &= \frac{eB}{mc}\frac{g-2}{2} \\ &= a_\mu \frac{eB}{mc} \end{aligned} \tag{2.5}$$

which is proportional to a_μ. Uncertainties on a_μ incorporate uncertainties on the magnetic field determination or in the muon mass determination but because $a_\mu \sim 1/800$ of g, measuring directly the anomaly increases the precision of almost three orders of magnitude. Looking at Fig. 2.2 it is possible to understand the spin precession concept. The figure shows the spin and momentum vectors for an initially forward polarized muon beam, moving along a circular orbit in a magnetic field. If the value of g is exactly 2, the

situation is the one of the left panel, where the spin vector is locked to the momentum direction. Since g is a little larger than 2, the spin vector slightly rotates more than 2π during each cyclotron period, as shown on the right panel. This procedure developed at CERN permits to improve the experimental precision and from this concept a series of experiments with increasing precision came out; three were performed at CERN, which will be referred to as CERN I, CERN II and CERN III, one at the Brookhaven National Laboratory (BNL) and a new one is now in operation at Fermilab (FNAL).

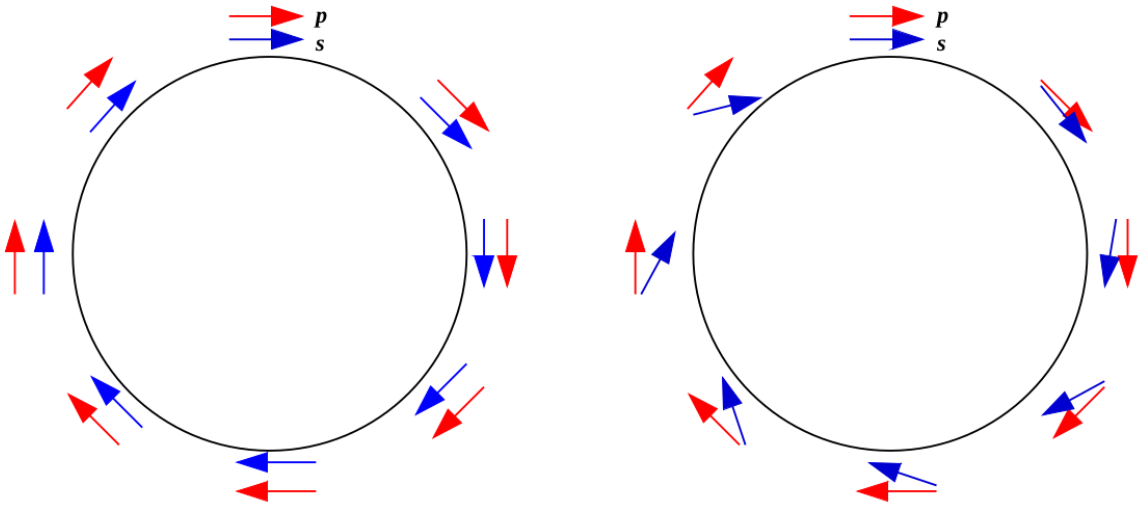

(a) $g = 2$ (b) $g > 2$

Figure 2.2: Illustration of the muon spin and momentum vectors for a muon orbiting in a magnetic field when $g = 2$ (a) and $g > 2$ (b).

2.1.1 CERN I

In the first experiment at CERN a forward polarized muon beam is injected into a 6 m long magnet, with a magnetic field of 1.5 T. The magnetic field causes the muon beam to move in a spiraling orbit. To create this kind of motion is important to shim carefully the magnetic field in order to be parabolic in the vertical direction

$$B(y) = B_0(1 + ay + by^2) \tag{2.6}$$

where the radius of the orbit is determined by the value of B_0, the linear term a causes each orbit to advance along the magnet and the term b produces a quadratic field pro-

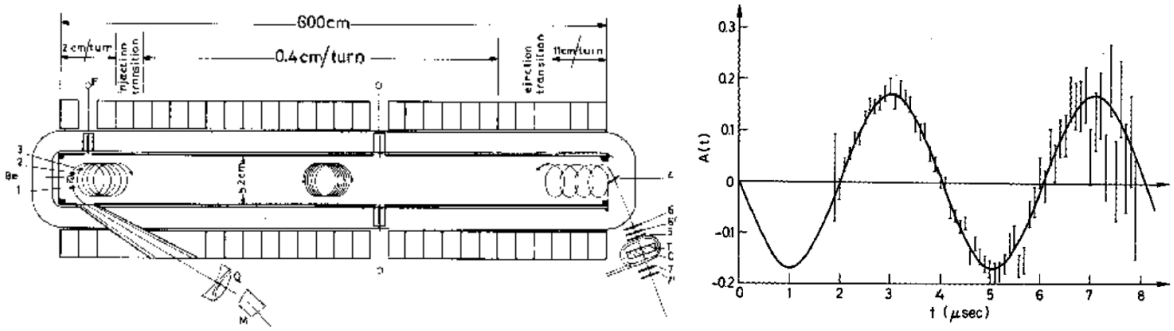

(a) CERN I setup (b) CERN I data

Figure 2.3: (a) An overview of the CERN I experimental setup and (b) the published data [35].

viding vertical focusing. Increasing gradually the value of a increases the step size of orbital 'walking'. At the end of the magnet this gradient is large enough to allow the muons to escape from the field. A methylene-iodide target stops the beam and from the asymmetry of the decay electrons the polarization is extracted. To determine the spin precession relative to the momentum is necessary to determine the amount of time spent by the muon beam in the magnetic field. To avoid the use of a forward and backward detector, with different efficiencies for each, the magnetic field is pulsed to alternately rotate the muon spin by $\pm 90°$ before injection. Data from CERN I don't appear to be more precise than Garwin data, as shown in Fig. 2.3, but they represent a direct measurement of the anomaly. Therefore, the precision of $5 \cdot 10^{-3}$ on a_μ

$$a_\mu^{exp}(1965) = 0.001162(5) \rightarrow 4300 ppm \tag{2.7}$$

implies a precision of 5 ppm on the determination of g. The muon mass and the constants in Eq. 2.2 were known at the time of the CERN I experiment with an adequate precision to extract a_μ. But using different techniques for extracting a_μ like Hutchinson's, provide a measurement independent on the muon mass. This technique gains importance as the precision of the anomalous precession experiments improves, since Eqs. 2.2 and 2.5 can be written as

$$\frac{\omega_a}{\omega_s} = \frac{a_\mu}{a_\mu + 1} \tag{2.8}$$

Multiplying and dividing the left side of the equation for the Larmor precession frequency of proton ω_p in the same magnetic field, the ratio can also be written as

$$\frac{\omega_a}{\omega_s} = \frac{\omega_a}{\omega_p}\frac{\omega_p}{\omega_s} \tag{2.9}$$

The factor ω_p/ω_s in Eq. 2.9 is the inverse of the ratio λ (Eq. 2.3) measured by Hutchinson independently. Frequencies in numerator and denominator of Eq. 2.9 are individually B dependent, but the ratio is not. This permits to take the value of λ and the ratio $R = \omega_a/\omega_p$ from different experiments to extract the value of a_μ. In fact solving Eq. 2.9 for a_μ considering λ and R one obtains

$$a_\mu = \frac{R}{\lambda - R} \tag{2.10}$$

With an accurate knowledge of λ, the value of a_μ can be extracted from experiments which measure the anomalous precession frequency ω_a and the proton Larmor frequency ω_p in the same apparatus. CERN I results were surprising due to the agreement with the prediction for the electron (see Eq. 2.7). It was expected a noticeable deviation because of the muon mass, as in the proton and neutron case, but the result was the proof that in terms of QED the muon behaves just as an heavier electron. This result, together with the idea of a CERN II experiment, led theorists to improve the QED calculation to second order in α (Fig. 2.4), with the new result [18]

$$a_\mu^{th}(1965) = 0.00116552(5) \rightarrow \pm 42 ppm \tag{2.11}$$

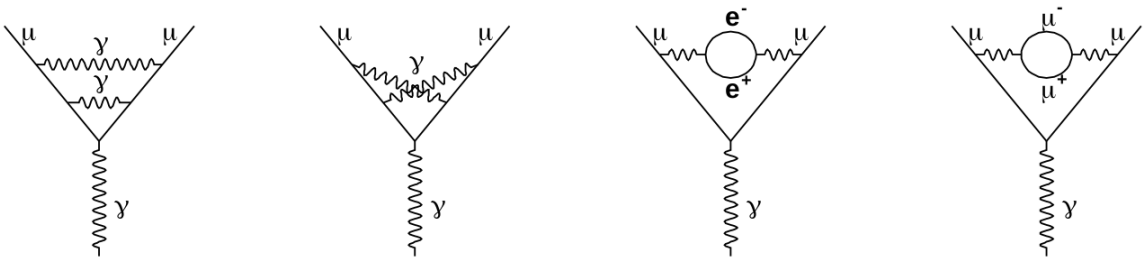

Figure 2.4: Some of the Feynman diagrams required in calculating the second-order QED contributions probed by CERN I.

where the error of $5 \cdot 10^{-8}$ is due to the uncertainty in the virtual loops containing hadronic processes. This value can be improved to $1 \cdot 10^{-8}$ with a first estimation of a third order QED calculation and by the knowledge of α. Uncertainties in the result of the CERN I experiment are mainly statistical. Examining the five parameter function

Eq. 2.1 used to fit data, the fractional error on ω_a is [19]

$$\frac{\delta\omega_a}{\omega_a} = \frac{\sqrt{2}}{\omega_a A \tau \sqrt{N}} \tag{2.12}$$

To improve the accuracy the first option is to increase N; a second option is related to ω_a, which being proportional to the magnetic field, contributes increasing the number of cycles to be fit increasing the field strength; a third option is to use a more energetic muon beam with a bigger lifetime; the fourth option is to improve the asymmetry A of the signal with better detectors and a more accurate choice of the energy threshold to maximize the level of the parity violating decay electrons. The advent of the PS at CERN provided a more energetic muon source with a luminosity higher than the Synchro-cyclotron giving the idea to the same group of physicist of CERN I to exploit the possibility to perform a measurement of a_μ.

2.1.2 CERN II

To setup the CERN II experiment a 5 m diameter storage ring with a C-shaped cross section was built. The polarized muon source was obtained by injecting a 10.5 GeV proton beam against a target placed inside the storage ring. The 1.7 T field in the storage ring selects forward-going pions of momentum p = 1.27 GeV/c. As the pion decays, a beam of longitudinally polarized muons with a relativistic factor $\gamma = 12$ were captured in the storage ring. This injection process was inefficient creating a large background due to protons and the large amount of pion momenta produced a less than optimal initial muon polarization. However, the luminosity of PS and the factor 12 in the dilated lifetime more than CERN I made up for the inadequacies associated with the injection. The decay electrons from the stored muons bend radially inward with respect to the muon orbit because of their lower momentum. Therefore, detectors had to be placed around the inner radius of the ring to detect the decayed electrons. Fig. 2.5a shows the experimental setup.

The CERN II experiment was able to measure for a_μ (Fig. 2.5b)

$$a_\mu^{exp}(1968) = 0.00116616(31) \rightarrow \pm 270 ppm \tag{2.13}$$

which is almost 2σ from the theoretical prediction. This level of discrepancy between the two values was resolved by Aldins and collaborators [37] examining QED contributions arising from light-by-light scattering (Fig. 2.6). This contribution was assumed to be

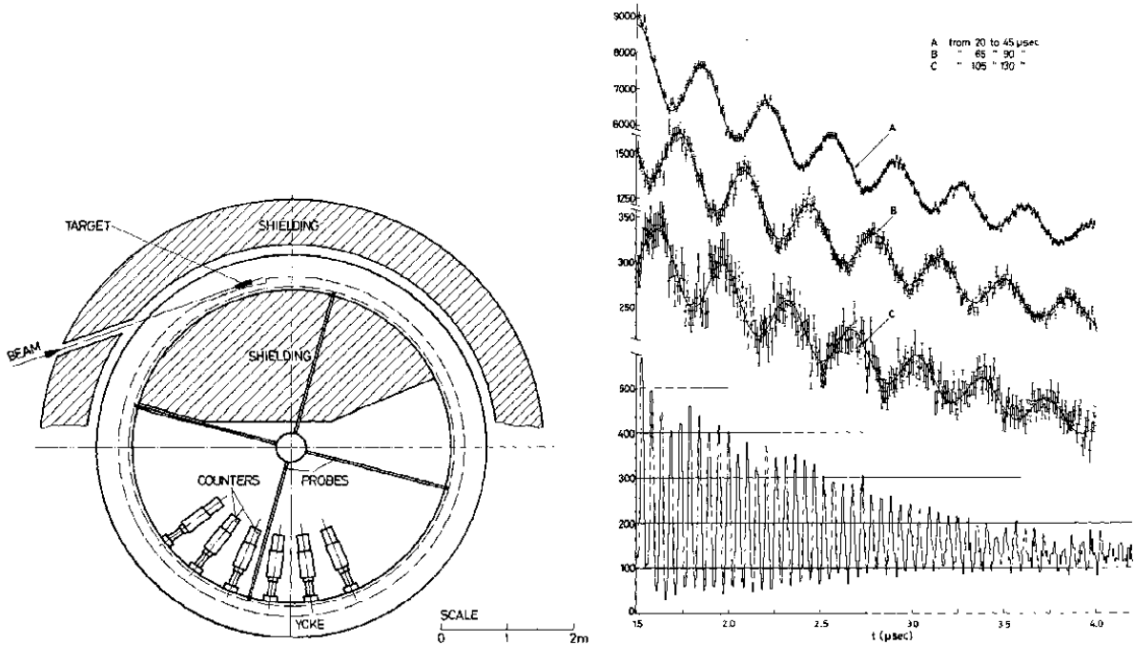

(a) CERN II Setup (b) CERN II Data

Figure 2.5: (a) An overview of the CERN II experimental setup and (b) the published data [36].

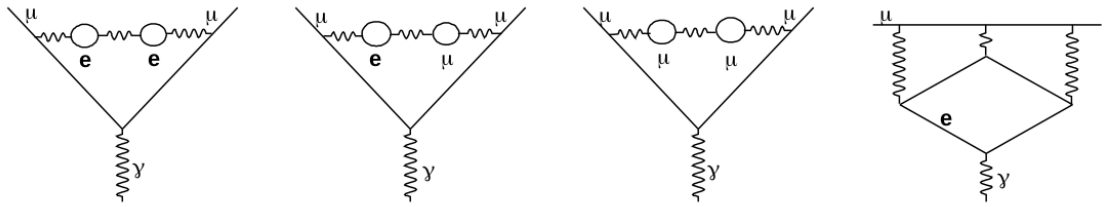

Figure 2.6: Feynman diagrams used to calculate the third-order QED correction to a_μ. The light-by-light diagram on the far right was the original source of the discrepancy between theory and experiment.

negligible but in 1969 was confirmed a 200 ppm contribution to the theoretical value of a_μ leading to a new determination:

$$a_\mu^{th}(1969) = 0.00116587(3) \rightarrow \pm 25 ppm \tag{2.14}$$

confirming the agreement between the experimental and theoretical values. The increasing precision of the experimental procedure required to start considering the hadronic contributions to vacuum polarization in the theoretical calculation of a_μ. Quantum chromodynamics does not provide a method to calculate hadronic loops at low energies associated with the muon's vacuum polarization. A way out is to take the electromagnetic coupling of hadrons from experimental data using the dispersion relation [38]

$$a_\mu^{HVP} = \frac{1}{3}\left(\frac{\alpha}{\pi}\right)^2 \int_{4m_\pi^2}^{\infty} \frac{R(s)}{s} K(s)\mathrm{d}s \tag{2.15}$$

where $R(s)$ is given by:

$$R(s) = \frac{\sigma(e^+e^- \to hadrons)}{\sigma(e^+e^- \to \mu^+\mu^-)} \tag{2.16}$$

and the function $K(s)$ is the QED kernel function. A more precise determination of the cross section data obtained at Novosibirsk and Orsay experiments [39, 40], were included as first in the paper of Gourdin and de Rafael [38], where they present a contribution of a_μ of $6.5(0.5) \cdot 10^{-8}$ to a_μ, with the error calculated solely from the uncertainty in the cross section measurements.

With the CERN I precision at 270 ppm, the 60 ppm calculated hadronic contribution to a_μ was not far from experimental reach. Therefore the CERN physicists once again started searching for ways to improve the experimental precision. The CERN II experiment had ended with a statistical error of $2.3 \cdot 10^{-7}$ and a systematic error of $1.9 \cdot 10^{-7}$, so a new experiment would have to improve on both fronts.

2.1.3 CERN III

The systematic uncertainty coming from the CERN II experiment is entirely due to the radial variation in the magnetic field required to provide vertical confinement. A possible solution could be to use a quadrupole electric field to prevent the stored muons from oscillating up and down into the magnet yoke. A relativistic muon will see this quadrupole electric field in the lab frame as a magnetic field in its rest frame; so the anomalous precession frequency will be derived as

$$\vec{\omega}_a = \frac{e}{m}\left[a_\mu \vec{B} - \left(a_\mu - \frac{1}{\gamma^2 - 1}\right)(\vec{\beta} \times \vec{E})\right] \tag{2.17}$$

The last term of Eq. 2.17 introduces a dependence of the spin frequency on the electric field. This causes a problem: while NMR probes provide an extremely accurate method of

measuring magnetic fields, there exists no equally precise method for measuring electric fields. Even if the option of electrostatic quadrupoles seems not to be a viable one, looking more closely at the coefficient in front of the electric field term it is apparent that a trick exists. If the coefficient $\left(a_\mu - \frac{1}{\gamma^2-1}\right)$ can be made zero, then a measurement of the electric field is no longer required. It turns out that for the correct relativistic gamma

$$\gamma = \sqrt{\frac{1}{a_\mu} + 1} = 29.3 \tag{2.18}$$

this coefficient is precisely zero. Nature was even kind enough to place this *magic* momentum for the muon at $p_\mu = 3.09$ GeV/c, which corresponds to a momentum that was easily attainable at the PS.

One other obstacle to be overcome before pushing the precision of a_μ was a new measurement of λ. The Hutchinson result had an error of about 13 ppm, which would not be sufficient for a measure of a_μ to a few parts per million. Several collaborations undertook the endeavor to better the λ measurement [41, 42], with the most precise performed by Ken Crowe and collaborators [43]

$$\lambda = \frac{\omega_\mu}{\omega_p} = \frac{\mu_\mu}{\mu_p} = 3.1833467(82) \rightarrow 2.6ppm \tag{2.19}$$

Once these major problems were solved, the design of the CERN III experiment began.

The experience obtained with CERN II was used to revisit the whole scheme and improve the experimental setup. Rather than injecting protons into the ring, the background could be greatly reduced by locating the target outside of the storage ring. Pions could then be transported to the interior side of the ring by using an inflector to cancel the strong fields in the backleg of the magnet. This allowed also to place detectors all around the circumference, increasing statistics, because the shielding blocks were not necessary as in CERN II. By transporting pions to the ring through a beamline, a very narrow range of pion momenta could be selected and the subsequent polarization of the stored muons was much higher. Finally, the magic momentum meant that the relativistic lifetime of the muons was precisely 64.4 μs, more than a factor of two more dilated than in CERN II. Essentially, every factor in the denominator of Eq. 2.12 was improved with the CERN III design. An overhead diagram of the storage ring and cross sectional views of the magnet and storage region are shown in Figure 1.9, as well as the data. The final result obtained after combining data for both the positive and negative muon was [44]

$$a_\mu^{exp}(1979) = 0.001165924(8.5) \rightarrow \pm 7ppm \tag{2.20}$$

where the fact that the 7 ppm error is dominated by statistical uncertainty proved the robustness of the new magic momentum technique. With a theoretical prediction of

$$a_\mu^{th}(1977) = 0.001165921(13) \rightarrow \pm 11 ppm \tag{2.21}$$

the CERN III results did not discover the origin of the muon mass but proved the importance of hadronic vacuum polarization contribution to the 5σ level.

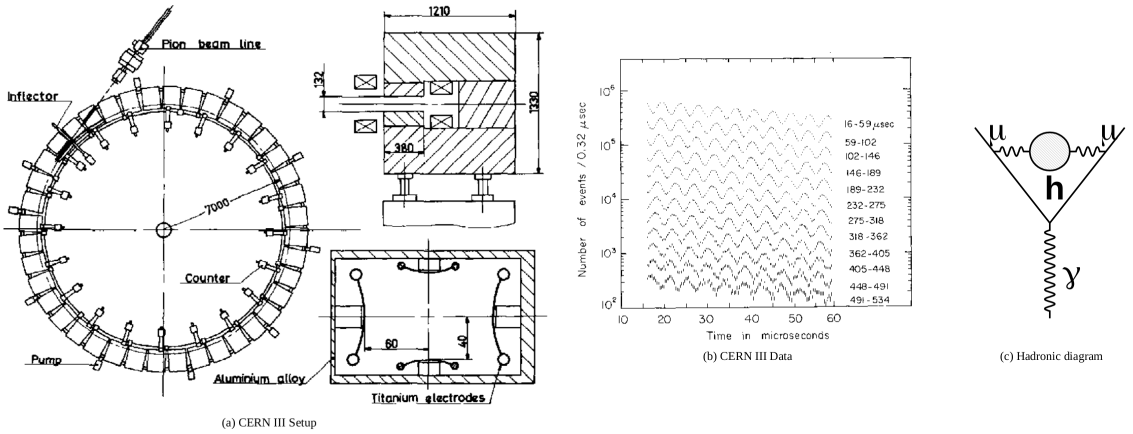

Figure 2.7: (a) An overview of the CERN III apparatus and (b) the published data [44]. (c) Feynman diagram depicting the contribution to a_μ from hadronic vacuum polarization that was first probed by CERN III.

2.2 The E821 experiment at BNL

Shortly after the CERN experiments came to a close, theoretical advances slowed to the point that pushing the experimental precision could no longer be justified. In 1984, Kinoshita and collaborators presented the results of a calculation complete to fourth order in α [45]. Furthermore, they pointed out that the error in the hadronic sector had been greatly reduced by improved measurements of the $R(s)$ cross sections and that a new experimental effort was in order. A group of physicist that included Vernon Hughes and many of the original CERN collaborators started to think about a possible experiment to be performed at the Alternate Gradient Synchrotron (AGS) at Brookhaven National Laboratory (BNL). From the first workshop meeting in 1984 and in the future ones, a design goal of measuring a_μ to 0.35 ppm was established.

At about this time, the 4 ppb precision of the electron g-2 experiments far outweighed any prospects for a next generation muon experiment. However, the contribution to a

lepton's vacuum polarization from heavy exchange particles scales as the square of the lepton mass, which gives the muon an amplification factor of $(m_\mu/m_e)^2 = 4 \cdot 10^4$ relative to the electron. This is the reason why the hadronic contributions to a_μ were tested at 5σ by the CERN III result, but at only 2 ppb for the electron are below the resolution of the a_e measurements. The enhancement factor of the muon mass more than compensates for the factor of 100 in the precision of a_μ versus a_e, thus measuring the magnetic moment of the muon provides a unique probe into the world of heavy virtual particles.

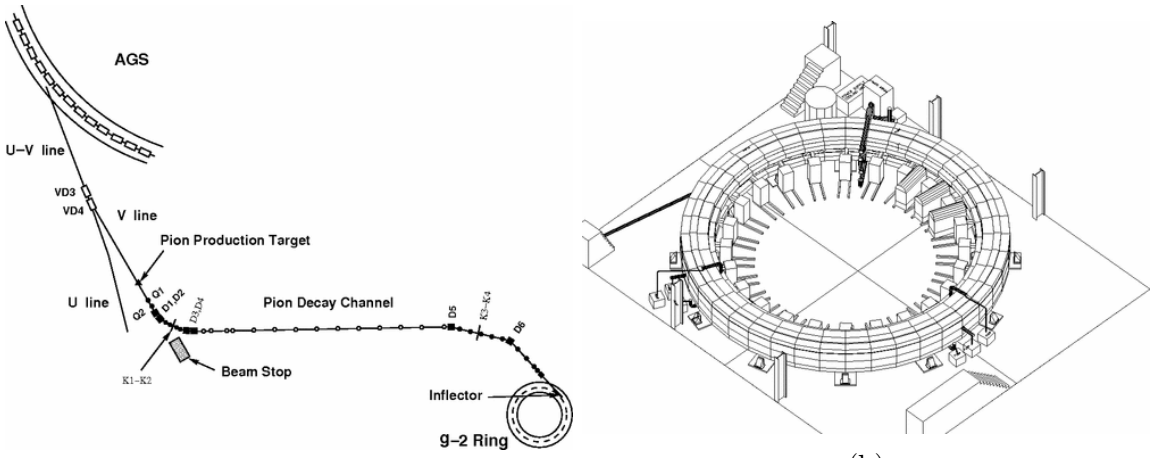

(a) (b)

Figure 2.8: (a) Plan view of the pion/muon beamline from AGS to the storage ring. The pion decay channel is 80 m and the ring diameter is 14.1 m. (b) Schematic of the BNL storage ring.

With the proposed precision, the BNL experiment would for the first time be sensitive to virtual exchanges from the weak sector. As in the past experiments, it also probes the limits of "new physics" contributions. The 7 ppm error in the CERN III experiment was dominated by statistics, which indicated that the method of operating a storage ring at a field corresponding to the *magic* momentum had not yet been systematically exhausted. Thus, the first step towards reaching a factor of 20 improvement over CERN required increasing the muon flux by approximately a factor of 400. A first factor comes from the AGS itself which is capable of delivering a beam which is almost a factor 20 more intense than the PS at CERN [46]; the second step comes from a better method of injection. In the final CERN experiment pions were injected into the storage ring through an inflector that cancelled the field in the yoke. Because of the uniform circular motion of particles in the storage ring, the pions could only complete one orbit before impacting the exterior wall of the inflector. Therefore, muons could only be obtained from pions that decayed in the first orbit. Rather than rely on pion injection for the

BNL experiment, it was realized that the number of muons stored per AGS cycle could be dramatically increased by allowing the pions to decay in a channel upstream of the storage ring and then directly injecting the resulting muon beam (Fig. 2.8a). To avoid interference of this muon beam with the inflector magnet after the first orbit, a series of kickers that shifted the muon orbit after injection with an electromagnetic impulse was implemented. Together with this, some more important improvements of the BNL experiment to keep systematic errors at a controlled level are listed below:

- The storage ring is constructed with three continuously wound superconductors, as opposed to the series of 40 independent conventional bending magnets used in CERN III.
- The inflector incorporates a superconducting shield to minimize the disruption of the field in the storage region, and unlike the CERN inflector, allows it to operate in a static DC mode.
- An NMR system capable of making an in-situ measurement of the field in the storage ring was designed, which unlike CERN III, does not require cycling the magnet power.
- In the BNL experiments, the decay electron signals from the calorimeters are recorded by waveform digitizers and stored for later analysis instead of relying on a hardware trigger.

It took almost 15 year of developments before starting to take data in 1997, and the first years of runs were just some test of the new improvements and subsystems. Nevertheless they were useful and gave also interesting results as shown in Fig. 2.9.

The experiment continued to take data on the positive muon until year 2000, where an eventual precision of 0.7 ppm was obtained for a_{μ^+} (Fig. 2.10) and then was decided to switch to the negative muon. Technically, this required switching the polarities of all of the beamline magnets, the inflector, and the storage ring itself. In practice, the optics behaved exactly as expected under the reversal, with very little optimization required to maximize the flux of stored muons. The switching procedure was a success and combining the data from both measurement the BNL experiment obtained a final result of [47]

$$a_\mu^{exp}(2006) = 11659208.0(5.4)(3.3) \cdot 10^{-10} \rightarrow 0.54 ppm \tag{2.22}$$

resulting in a difference with the theoretical value of the time of 2.7σ.

The improvement in the statistical power relative to CERN can be observed by comparing Figure 2.10 to Figure 2.7. The signal in the CERN data has virtually disappeared by 500 μs, while the BNL signal is still clearly visible at 700 μs.

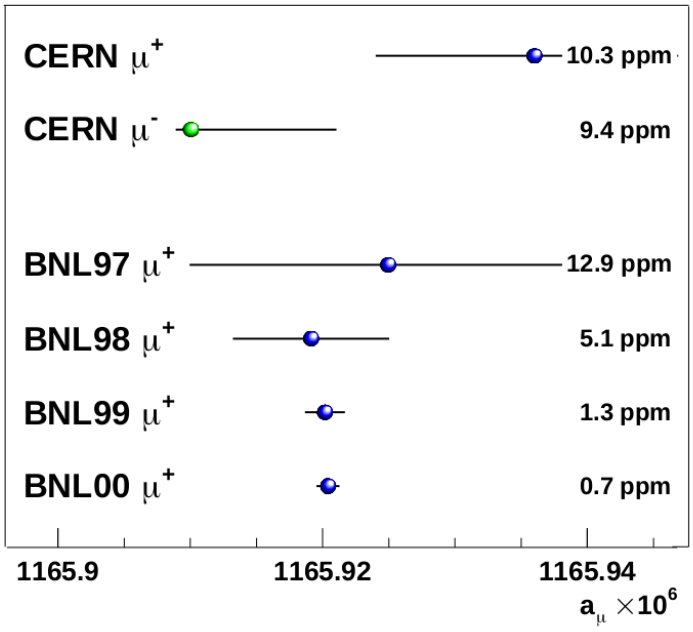

Figure 2.9: Progression of experimental precision from CERN through the 2000 BNL data set.

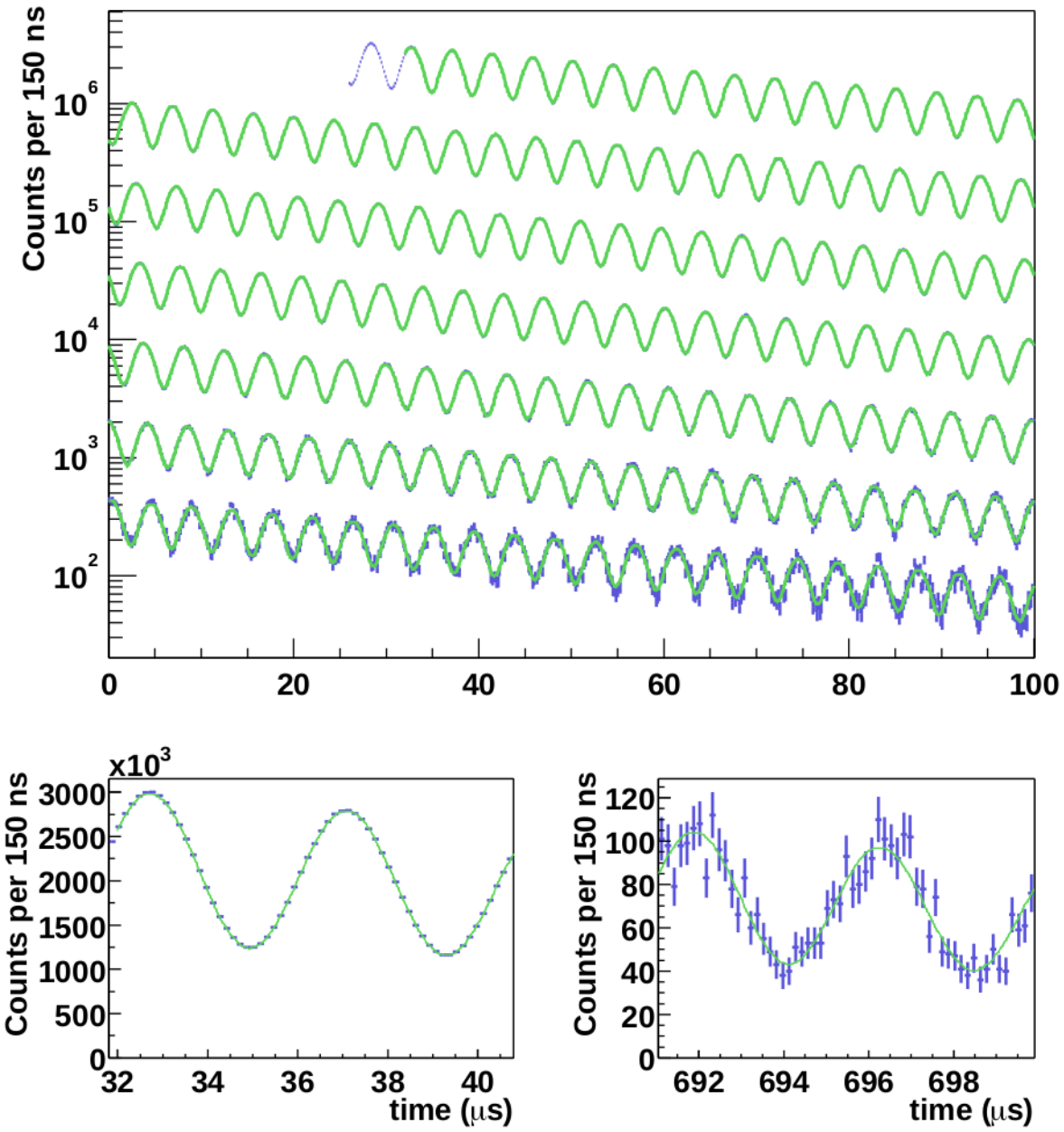

Figure 2.10: Data from 2000 $\mu+$ data set with a five parameter fit of the form in Eq. 2.1 overlayed.

Chapter 3

The E989 experiment at Fermilab

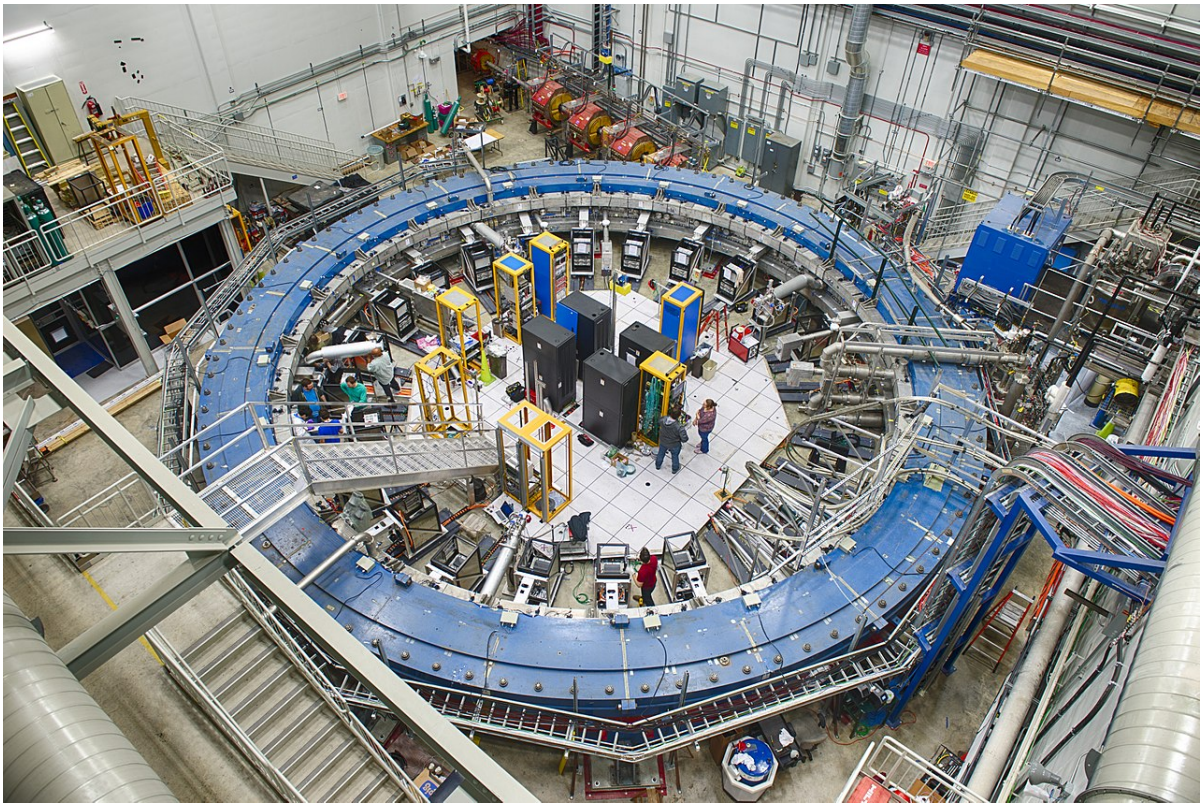

Figure 3.1: The Muon g-2 experiment at Fermilab.

The new Muon g-2 experiment in operation at Fermi National Accelerator Laboratory aims to measure the muon's anomalous magnetic moment with a precision of 0.14 ppm, a factor 4 better than the previous BNL E821 experiment.

To achieve this precision, several aspects of the experiment have to be improved, both to increase the number of muons observed, and to reduce the systematic uncertainties. The experimental technique is the same as the one used for the CERN III and BNL experiments, as it has proven successful and it presents room for improvements.

The BNL storage ring was moved from Brookhaven to Fermilab and installed in the muon campus, at the end of the FNAL accelerator chain. Fermilab accelerators can provide a much more intense beam allowing the experiment to collect 21 times the statistics of the BNL experiment in two or three years. While BNL E821 improved on the CERN III experiment in a revolutionary manner, primarily by the invention of direct muon injection into the storage ring, the FNAL E989 experiment will introduce a broad suite of refinements focused on optimizing the beam purity and rate, the muon storage efficiency, and modernizing the instrumentation used to measure both ω_a and ω_p [48].

The E989 experiment will measure a_{μ^+} during the first run, due to the enhanced cross section for producing μ^+ using protons at the target, but a_{μ^-} may be measured in a second run. Theoretically $a_{\mu^+} \equiv a_{\mu^-}$, but measuring both provides a way to perform a CPT theorem test. Since the values measured for a_{μ^+} and a_{μ^-} in the E821 experiment were statistically consistent, the E821 Collaboration averaged the two values to produce their final experimental value.

The total uncertainty of 0.14 ppm expected for the E989 experiment is subdivided into 100_{stat} ppb and 100_{sist} ppb. Some of the various improvements needed to reach this goal uncertainty are [49]:

- higher proton rate with less protons per bunch. Since the detected positron number is directly proportional to the protons on target, the Fermilab experiment will have to deliver $4 \cdot 10^{20}$ total protons. These high numbers are within reach thanks to the Fermilab beam complex which is expected to annually deliver $\sim 2 \cdot 10^{20}$ protons with an energy of 8 GeV on an Inconel core target [50];

- a very long pion decay line. A limiting factor at BNL was the 120 m beamline between the pion production target and the storage ring; since the decay length of a 3.11 GeV/c pion is ≈ 173 m, the beam injected into the storage ring contained both muons and a significant number of undecayed pions. Those pions create an enormous burst of neutrons when they intercept materials [48]. The new decay line will be more than 2000 m long, also thanks to the four orbits around a 500 m long Delivery Ring: virtually no pion will reach the muon storage ring without

decaying;

- 6-12 times larger muon yield per proton and 3 times the muon beam rate: the muon storage ring will be filled at a repetition rate of 12 Hz, which is the average rate of muon spills that consists of sequences of successive 700 μs spills with 11 ms spill-separations, compared to 4.4 Hz at BNL [50];

- improved detectors and new electronics: the detectors and electronics will all be newly constructed to meet the demands of measuring the anomalous spin precession frequency to the 70 ppb level. This is a substantial improvement over the E821 experiment where the total systematic error on ω_a was 180 ppb. Better gain stability and corrections for overlapping events in the calorimeters are crucial improvements addressed in the new design. A new tracking system will allow for better monitoring of the stored muon population, and to establish corrections to ω_a that arise from electric field and vertical oscillations; [52];

- better monitoring of B-field variations: the storage ring magnetic field, and thus ω_p, will be measured with an uncertainty that is approximately 2.5 times smaller. This is done by placing critical Nuclear Magnetic Resonance (NMR) probes at strategic locations around the ring and shimming the magnetic field by placing wedges and small steel foils to achieve a high uniformity [53];

- a continuous monitoring and re-calibration of the detectors, whose response may vary on several timescales from nanoseconds to days, will be required: a high-precision laser calibration system that will monitor the gain fluctuations of the calorimeter photodetectors at 0.04 % accuracy will be used [49].

3.1 Production and injection of the muon beam

In this section we review the production of the muon beams that are used for this experiment. The overall structure of the accelerator complex is schematized in Fig. 3.2.

The FNAL muon campus beamline is constructed to deliver pure pulses of highly polarized muons to the E989 storage ring. The muons originate from decaying pions, which are in turn produced by focusing a proton beam on a target. The protons begin their journey in the linear accelerator **Linac** and accelerate through the **Booster**. From there, the protons continue into the **Recycler Ring** where they are grouped into high

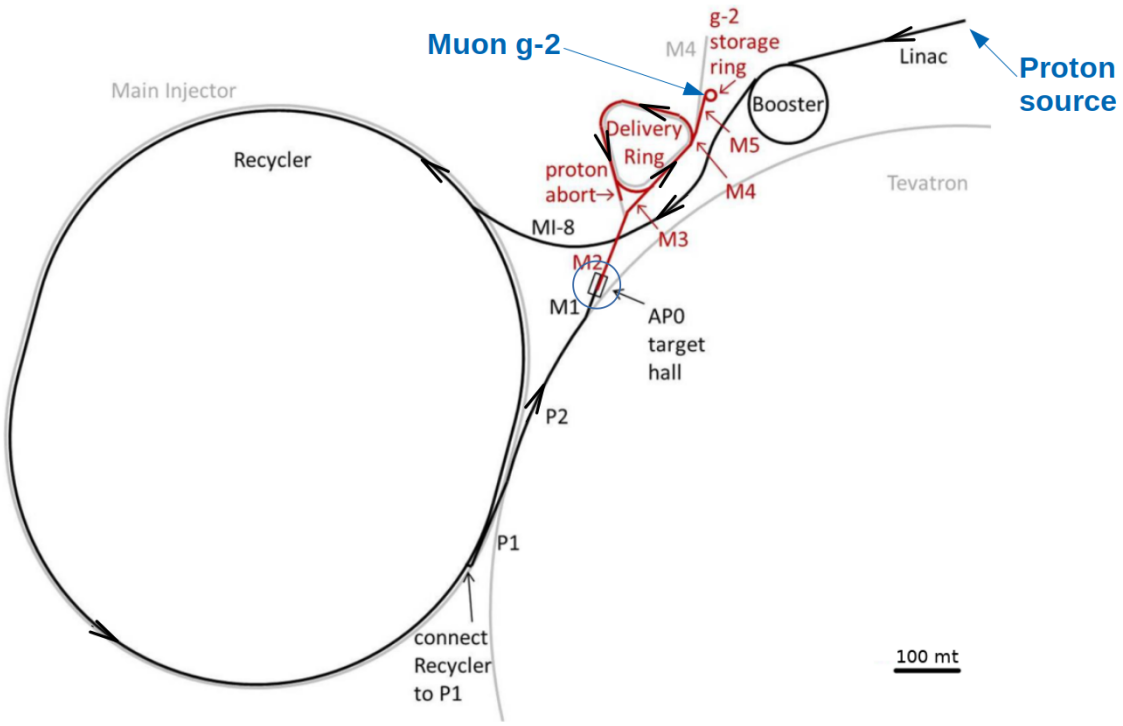

Figure 3.2: The diagram depicts all relevant FNAL beamlines that are used to produce muons for *g-2* [15]. Protons (black lines) begin accelerating in the Linac, and end up colliding with a target (AP0). Positive secondaries (including pions which later decay into muons) with a momentum of 3.1 GeV/c are focused and transported to the Delivery Ring. In the Delivery Ring, the bunch propagates long enough to have most of the pions decayed, and to develop a time separation between protons and the muons that compose the beam. With this time separation, the proton can be dumped and the muons can be extracted to continue to the *g-2* storage ring.

intensity bunches with a short temporal width of ∼120 ns. Each proton bunch contains $\mathcal{O}(10^{12})$ protons with 8 GeV kinetic energy. The protons then propagate from the Recycler to the **AP0** target hall through (the antiproton production hall used by the Tevatron) where they collide with an *Inconel* target. The collision produces $\mathcal{O}(10^{9})$ positive secondary particles of which many are pions. The secondary particles are focused via an electrostatic lithium lens into a secondary beam which goes through a momentum filter shortly after focusing. Momentum selection yields a beam of 3.1 GeV/c with a momentum spread of $\pm 0.10 \frac{\Delta p}{p}$. The secondary beam then proceeds through M2 and M3 beamlines into the **Delivery Ring**.

The goals in the Delivery Ring are twofold. First, the beam cycles around the Deliv-

ery Ring to create a spatial separation between the pions/muons and the more massive protons (slightly lower velocity for the same momentum), so that the protons can be removed. Protons with momentum 3.094 GeV/c have a relativistic γ of 3.3 and travel at about 95% the speed of light. Muons with a γ of 29.3 travel within 0.1% of the speed of light. Therefore, after each trip around the Delivery Ring the protons fall 25 m behind the muons. Secondly, essentially all pions decay in flight into muons, so that the outgoing beam is a very pure muon beam. The pion decay line is ∼2 km long while the one of Brookhaven was only 120 m. Four orbits around the Delivery Ring are enough to achieve both goals.
After the Delivery Ring, the now muon beam is extracted onto the path toward the **Storage Ring**. Through the pion decay process the high and low energy muons have a net spin polarization (as discussed in section 1.2.1), and the beamline design acceptance is narrow around the filtered secondary energy of 3.1 GeV/c. The muons produced at 3.094 GeV/c by the pion beam are forward decays and thereby achieve a net spin polarization of around 95%. The distribution of delivered muons has a momentum RMS of approximately 2% centered around 3.094 GeV/c and a temporal length of 120 ns. Of these injected muons, only 1% to 2% can be stored. A bunch of muons produced in the beamline is referred to as a "fill". These fills deliver $\mathcal{O}(10^4)$ muons to the storage ring at an average rate of 11.4 Hz [15]. With a 4.5 cm radius storage region and a 7.112 m orbit radius, the E989 ring can at best store muons within approximately 0.5% of the design momentum.

3.2 The Storage Ring

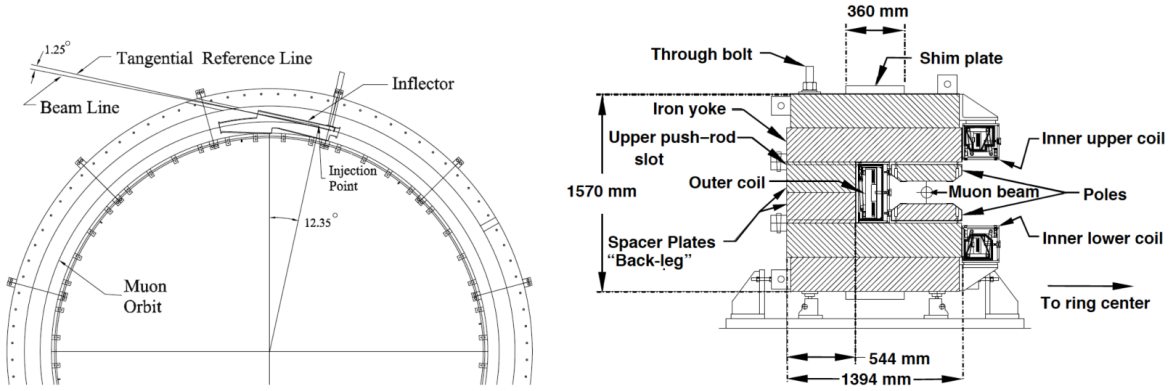

Figure 3.3: Top down and cross sectional view of the Storage Ring [15].

After a final focusing, the beam enters through a hole in the "back-leg" of the magnet and then crosses into the superconducting inflector magnet [54], which provides an almost field free region, delivering the beam to the edge of the storage region. Without it, muon injection into the storage ring would not be possible because passage through the fringe field would deflect the beam into the magnet iron. Once that the beam is injected it requires to be *kicked* otherwise it will impact against the inflector after one turn. The exit of the inflector is displaced 77 mm radially outward from the center of the storage region, so that the beam is injected in an orbit slightly shifted from the designed one. To store the particles that enter the storage ring vacuum, a pulsed kicker magnet fires as the muon beam crosses the ideal orbit 90° around the ring from the injection site. The kicker pulse length is ideally less than the muon orbital period, 149 ns, so that each particle is only kicked once. The ideal kick is exactly strong enough to deflect design-momentum muons onto the ideal orbit. Copper collimators placed around the ring define a 9 cm diameter transverse area of the beam.

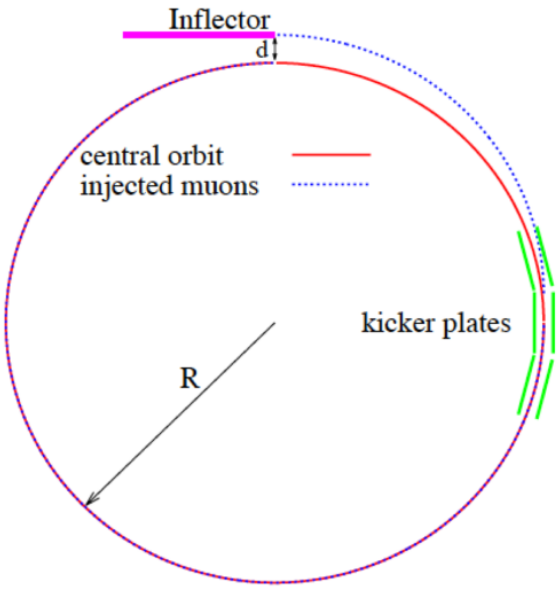

Figure 3.4: Diagrammatic illustration of injection into the storage ring [15]. During the first turn after injection, the kickers provide the deflection necessary to place muons onto the central storage orbit.

3.2.1 The magnetic field

The E989 magnetic Storage Ring, shown in Fig. 3.1 and 3.3 is the same one previously used in the E821 Muon g-2 Experiment at Brookhaven National Lab. The magnetic field in the vacuum chamber is generated by three superconducting NbTi/Cu coils around a C-shaped yoke as shown in figure 3.3. They operate with a current of 5176 A, providing an uniform vertical magnetic field [15]. The C-shape faces the interior of the ring so that positrons from the muon decay, which spiral inward, can travel unobstructed by the magnet yoke to detectors placed around the interior of the storage ring. During the assembly of the ring a shimming process was applied to be sure that the magnetic field is as uniform as possible inside the beam storage volume.

The magnetic field is of critical importance to the *muon g-2* experiment. A magnetic field of 1.4513 T puts muons with "magic" momentum, 3.094 GeV/c, into uniform circular motion at the "magic" radius of 7.112 m. In this magnetic field the muons circulate many times around the ring ($\sim$4500 orbits in 700 μs), until they all decay. A very precise measurement of the magnetic field is crucial for the success of the experiment, for two main reasons. To first order, the value of $\vec{B}$ directly affects the rate of muon spin precession and cyclotron frequency, as seen in section 1.1.1. To second order, the magnetic field influences the beam dynamics of the stored muons. These deviations in beam dynamics make the analysis which matches muon trajectories with the magnetic fields along them more difficult, and therefore add uncertainty to the determination of the expectation value for ω_p.

3.3 The detectors

When a muon decays, the produced decay positron has less energy than its parent muon and correspondingly a smaller orbit radius in the storage ring's magnetic field; decay positrons curl toward the center of the ring. There are 24 electromagnetic calorimeters stationed around the inner radius of the storage ring to intercept these decay positrons and measure their energies and hit times. This process is illustrated in Figure 3.5. With 24 calorimeters equally spaced azimuthally, the probability that a decay positron will hit a calorimeter (called the acceptance) becomes very high, about 80%, for the decay positrons nearest the endpoint of the energy spectrum [15].

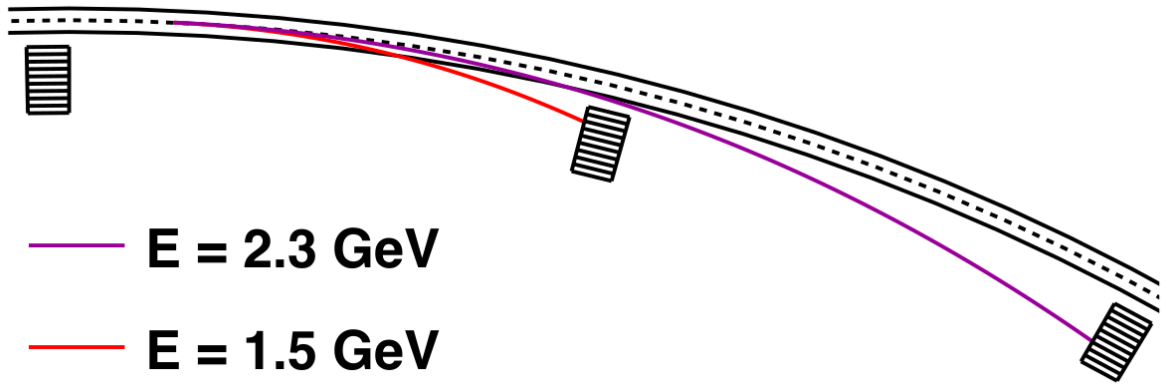

Figure 3.5: Illustration of muon decay in the storage ring [56]. The black curves delineate the storage region, and the dashed line is its center. The rectangular objects represent the electromagnetic calorimeters. When a muon decays in the storage region, its decay positron will curl inward and may strike a calorimeter. The red and magenta curves show the paths that decay positrons of two different energies would take if they were born at the same location with momenta tangent to the ideal orbit.

3.3.1 Calorimeters

The calorimeters are the primary instruments for the ω_a measurement. The main purpose of the calorimeters is to establish a time and energy for each detected positron. Each one consists of a 6 high by 9 wide array of lead fluoride (PbF_2) crystals, each one is a 14 cm long block with a square cross section of side 2.5 cm (Fig. 3.6). Every crystal is coupled with a Silicon PhotoMultiplier (SiPM) detector (Fig. 3.7), with a sensitive area smaller than the crystal it's attached to. While this kind of calorimeter has not been extensively used in the past, its properties are particularly well suited to the needs of the Muon g-2 experiment: PbF_2 has very high density (7.77 g/cm^3), a 9.3 mm radiation length and a Molière radius of $R_M = 22$ mm for energy deposition. High density allows for decay positrons to deposit virtually all of their energy in a relatively compact calorimeter. The crystals are 14 cm long, that is approximately 15 radiation lengths. The width of 2.5 cm is higher than the Molière radius, thus the energy depositions of a typical decay positron is contained almost entirely within one or two crystals. The segmentation of the detector decreases the likelihood of two decay events occurring simultaneously in the same SiPM. These double events are referred to as *pileup* and were a major source of uncertainty in E821 [15].

Incoming positrons deposit energy in each crystal by producing an electromagnetic

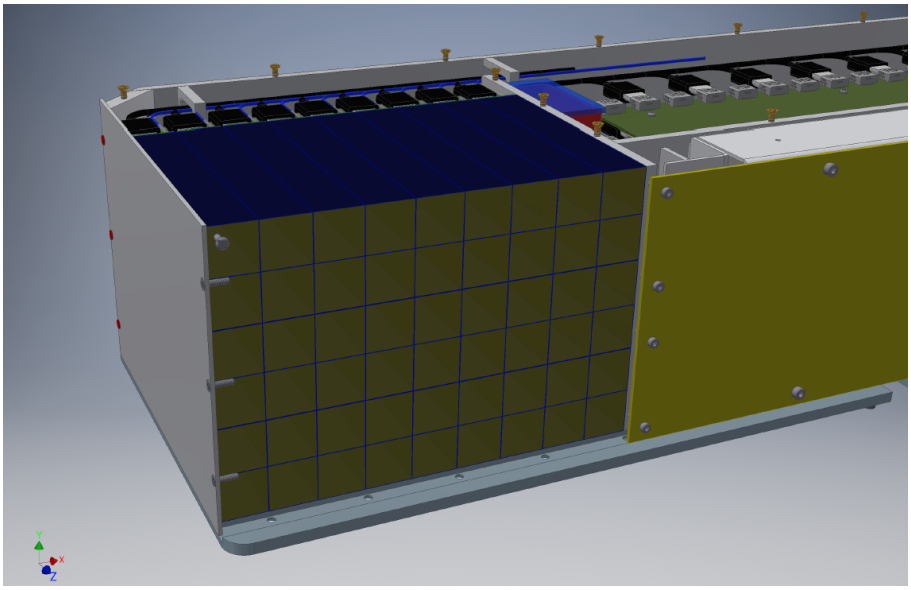

Figure 3.6: Model of the E989 calorimeter [56]. The active volume comprises a 6 by 9 array of PbF_2 crystals. There are 24 calorimeters equally spaced around the E989 storage ring.

shower, and emitting Čerenkov radiation in few nanoseconds. The refraction index of PbF_2 is 1.8: Čerenkov radiation is produced only by positrons that travel faster than $c/1.8$, that is with a kinetic energy of ∼100 keV. All the positrons emitted by the decaying muons have an energy significantly higher than 100 keV. The choice of a pure Čerenkov material is driven by the almost instantaneous signal produced when an electron strikes a crystal. There is no delay as one would expect from a scintillator. Considering the 14 cm crystal lengths, the relevant time scale for Čerenkov light production is on the order of 1 ns. In addition, the PbF_2 crystals have a very low magnetic susceptibility, perfect for working in a magnetic environment without perturbing the magnetic field itself. Each crystal is wrapped in a black-tedlar absorptive material which, even if it has a light yield lower than a reflective one, ensures a faster response of the crystal.

The SiPMs work as a Geiger-mode counter, with 57344 pixels each one 50 μm wide on a 1.2×1.2 cm^2 device. Each pixel contains a resistor in series with the avalanche photodiode (APD), called the quenching resistor. They serve to arrest the avalanche and allow the device to recover with a recovery time constant typically of ∼10 ns. This recovery time will be one of the important aspect of the study described in chapter 6. Finally, the produced electrical current passes through a custom electronic readout board where it is converted into a voltage signal. These voltage signals are recorded by 12-bit,

800 MS/s waveform digitizers [55].

The SiPMs are intrinsically non-linear. The term "Geiger-mode" refers to the fact that a given pixel either fires (produces signal) or it does not. The consequence of this is that a SiPM can never count more photons than the number of its pixels, 57344 in this case. The number of pixels that produce signal can be expressed as:

$$N_{fired} = N_{tot}\left(1 - e^{-\frac{\epsilon N_\gamma}{N_{tot}}}\right) \xrightarrow{N_\gamma \to 0} \epsilon N_\gamma \tag{3.1}$$

where ϵ is the probability that an incident photon will induce a signal in a pixel, N_{tot} is the number of pixels (57344) and N_γ is the number of incident photons. The response is linear only in the approximation of low energy (low N_γ). The typical number of Čerenkov photons emitted by a high-energy decay positron is about 2000, resulting in a number of pixels that fire ∼2% less than the linear case.

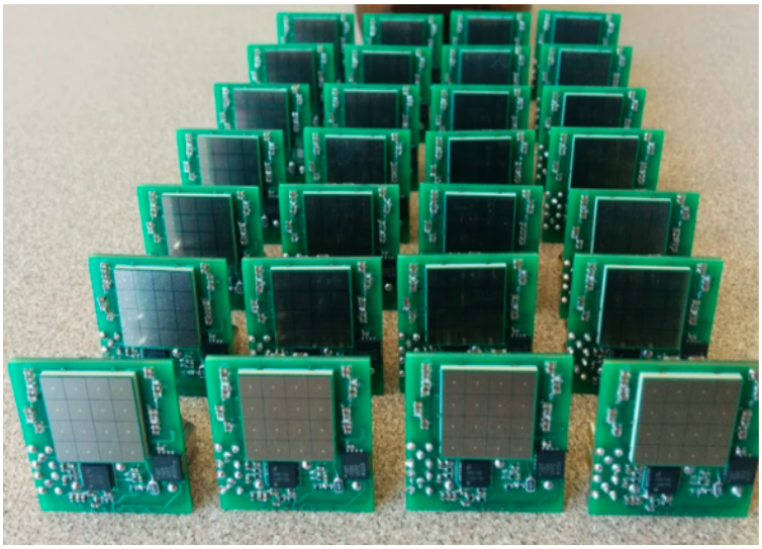

Figure 3.7: The silicon photomultiplier (SiPM) detectors and their readout board [57].

Choosing SiPMs over PMTs is advantageous, as they can be placed inside the storage ring field without perturbation, avoiding the long light guides that would be needed for remote PMTs as in E821. On the other hand, SiPMs are very sensitive to temperature and bias voltage, thus making their gain calibration a challenging and important task. All the 1296 channels are calibrated during data taking using the Laser Calibration System, described in chapter 4.

3.4 Measuring a_μ

The experimental technique was briefly presented in Chapter 2 following the historical development of the experiment, and will be described here with more detail.

A charged particle with mass m, and placed in an uniform external magnetic field will follow a circular path because of the the Lorentz force, and this motion is called cyclotron motion. If the particle has spin, its direction will also rotate (precess) in the same plane of the circular orbit.
In the absence of electrical fields, and with the particle velocity perpendicular to the magnetic field, the equations governing this motion are:

$$\vec{\omega}_s = -\frac{ge\vec{B}}{2m} - (1-\gamma)\frac{e\vec{B}}{m\gamma} \tag{3.2}$$

$$\vec{\omega}_c = -\frac{e\vec{B}}{m\gamma} \tag{3.3}$$

ω_s is the spin precession angular frequency and ω_c is the cyclotron frequency. γ is the relativistic Lorentz factor, and g is the particle's g-factor. The second term of Eq. 3.2 is a relativistic correction to the Lorentz force, called Thomas precession. It accounts for the rotation of the particle's frame of reference. The rotation of the particle spin with respect to its momentum is called anomalous precession frequency, ω_a, and is:

$$\vec{\omega}_a = \vec{\omega}_s - \vec{\omega}_c = -\left(\frac{g-2}{2}\right)\frac{e\vec{B}}{m} \equiv -a_\mu \frac{e\vec{B}}{m} \tag{3.4}$$

The E989 experiment houses several electrostatic quadrupoles, in the magnetic region, that serve to focus the beam. The anomalous precession frequency is sensible to such electric fields:

$$\vec{\omega}_a = -\frac{e}{m}\left[a_\mu \vec{B} - \left(a_\mu - \frac{1}{\gamma^2-1}\right)(\vec{\beta}\times\vec{E})\right] \tag{3.5}$$

However, for a muon beam with *magic* momentum $p_\mu = 3.094$ GeV/c, corrisponding to a value of $\gamma = 29.3$, the second term of Eq. 3.5 cancels out, so that Eq. 3.4 holds.
From Eq. 3.4 we see that we can evaluate the anomalous magnetic moment a_μ from the measurement of ω_a and $\vec{B}$:

$$\vec{\omega}_a = -a_\mu \frac{e\vec{B}}{m} \qquad \rightarrow \qquad a_\mu = -\frac{m}{e}\frac{\vec{\omega}_a}{\vec{B}} \tag{3.6}$$

This means that two values have to be measured with high accuracy in order to achieve the final 0.14 ppm precision. The value of ω_a is measured by the observation of the decay positrons as a function of time, and this is done by the calorimeter system. The value of the magnetic field can be measured by the observation of the Larmor precession frequency of the proton (ω_p) in the same magnetic region where the muons are stored. We can rewrite the Equation 3.6 using the following relations:

$$B = \frac{\hbar\omega_p}{2\mu_p} \qquad\qquad e = \frac{4m_e\mu_e}{\hbar g_e} \tag{3.7}$$

where μ_p is the proton's magnetic dipole moment; g_e, μ_e, and m_e are the g-factor, the magnetic dipole moment, and the mass of the electron. The three latter terms are given by past experiments. We get:

$$a_\mu = \frac{\omega_a}{\tilde{\omega}_p}\frac{g_e}{2}\frac{m_\mu}{m_e}\frac{\mu_p}{\mu_e} \tag{3.8}$$

where $\tilde{\omega}_p$ is the particle distribution weighted spatial average of ω_p. The first fraction $\omega_a/\tilde{\omega}_p$ is what this experiment will measure. The other three fractions are known from prior experiments with high enough precision, as reported by CODATA [58].

3.4.1 The proton precession frequency ω_p

The magnet field measurement consists of various components and techniques used to determine the value of ω_p, the free proton Larmor precession frequency in the storage ring. To achieve this, 378 Nuclear Magnetic Resonance (NMR) fixed probes are placed along the ring under and over the vacuum chamber. The probes keep monitoring the field during the whole data taking. Once in a while, especially after changes in the magnetic field or ring shutdowns, *trolley* runs are performed: a cylinder equipped with 17 NMR probes, is moved on rails inside the vacuum chamber along all the ring (Fig. 3.8). The trolley measurements produce a three dimensional map of the magnetic field inside the storage region. All these expedients are used to bring the field uncertainty at about 70 ppb.

3.4.2 The anomalous precession frequency ω_a

The measurement of the anomalous precession frequency is performed using the calorimeters. The standard analysis procedure is to identify individual decay positrons and plot the rate of their arrival versus time. The number of detected positrons above a single

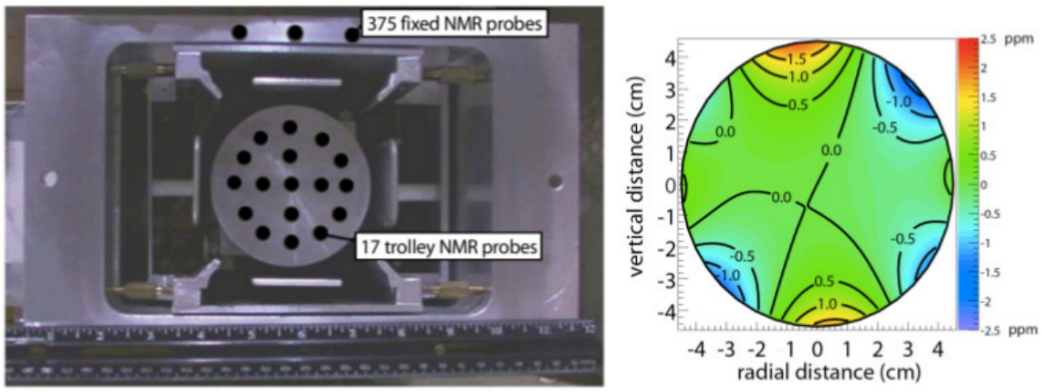

(a) (b)

Figure 3.8: (a) The electrostatic quadrupole assembly inside a vacuum chamber showing the NMR trolley sitting on the rails of the cage assembly. Seventeen NMR probes are located just behind the front face in the places indicated by the black circles. The storage region has a diameter of 9 cm. (Copyright 2006 by the American Physical Society.) (b) A contour plot of the magnetic field averaged over azimuth, 0.5 ppm intervals.

energy threshold E_{th} is

$$N(t) = N_0 e^{-\frac{t}{\tau}}[1 + A\cos(\omega_a t + \phi)] \tag{3.9}$$

where the normalization N_0, the asymmetry A and the initial phase ϕ are all dependent on the energy threshold. τ represents the lifetime of the muon in the laboratory system, that is $\gamma\tau_\mu$. There is a number of ways to extract ω_a using such function, differing on how to weight the events depending on energy. The T-Method (Threshold) uses a weight of 1 for positrons above a certain energy (usually 1.7 GeV) and 0 for positrons below that threshold. The E-Weighted and A-Weighted methods instead weight the events linearly on energy and on the asymmetry respectively. The A-Weighted technique yields the maximum possible statistical power for a given threshold using the event identification technique. The histogram used to plot the positron counts as a function of time is called *wiggle plot* and is shown in Fig. 3.9.

Equation 3.9 contains five parameters (N_0, $\gamma\tau_\mu$, A, ω_a, ϕ) and it represents the number of counts we expect for muons that orbit exactly with the magic radius without any side effect. A real-world experiment has these effects that affect the measurement to some degree. For example, the beam has its own dynamics due to the magnetic and electric field applied in the storage ring by the dipoles, the kickers and the electrostatic

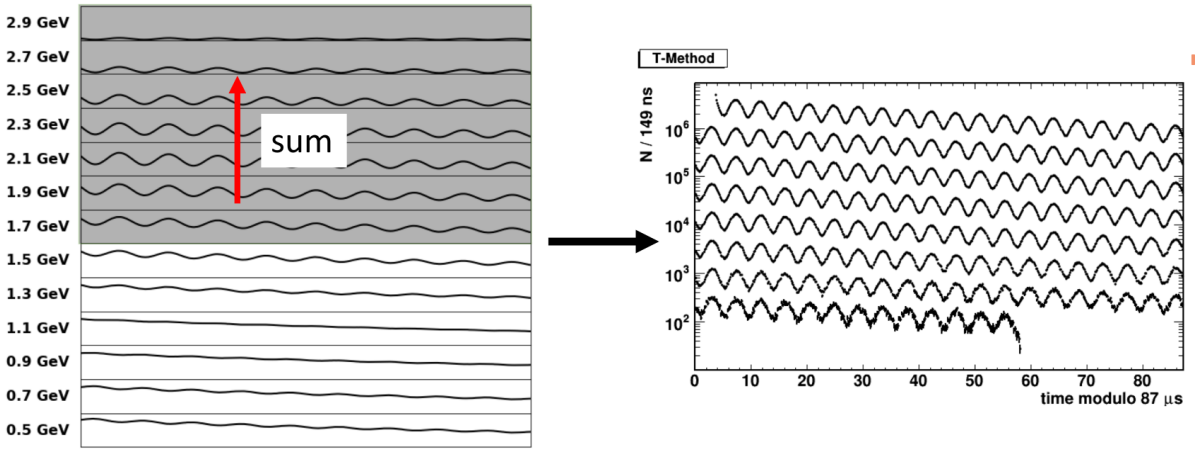

Figure 3.9: Illustration of the T-Method for ω_a analysis [56]. On the left are the calorimeter signals in a number of different energy windows. Summing the signals from all energies above a certain threshold yields the one dimensional T-Method histogram shown on the right. This histogram is also called the *wiggle plot*. The T-Method signal is wrapped on itself every 87 μs to show the entire 700 μs measurement period. The period of the oscillations visible in the T-Method histogram is $2\pi/\omega_a$.

quadrupoles for focusing. In particular it oscillates both in the radial and in the vertical directions with a frequency dependent on the quadrupoles strength. This phenomenon is called Betatron Oscillation. The functions used to fit the T-Method histogram contains a number of parameters that depends on how many corrections are being addressed. Listing here some of them, we have:

- **Coherent Betatron Oscillation (CBO)**: is the correction for the oscillation of the beam in the radial direction. The direction of the positrons emitted by the decay is influenced by this effect, resulting in an oscillation in the number of events. The correction is parameterized using 4 parameters (A_{CBO}, τ_{CBO}, ω_{CBO}, ϕ_{CBO}) and applied to Eq. 3.9 as a multiplicative term:

$$N_{9par}(t) = N_{5par}(t) \cdot \left[1 - A_{CBO} e^{-\frac{t}{\tau_{CBO}}} (\cos(\omega_{CBO} t) + \phi_{CBO})\right] \tag{3.10}$$

  where τ_{CBO} is the CBO lifetime and the other parameters have similar meanings to the 5-parameters equation 3.9.

- **Lost Muons**: is a correction that accounts for the muons that are lost by the storage ring. This loss lowers the number of positron counts, with the effect of altering the exponential shape of the muon decay. This correction is parameterized

by one parameter L defined as

$$N_{10par}(t) = N_{9par}(t) \cdot \left[1 - K_{loss} \int_0^t L(t') e^{-\frac{t'}{\tau}} dt'\right] \tag{3.11}$$

where $L(t)$ is the number of lost muons as a function of time in the *fill* window of 700 μs, $\tau = \gamma\tau_\mu$ is the lifetime of the muons and K_{loss} is the parameter, an acceptance factor. The function $L(t)$ is found using a dedicated analysis and extracted prior the ω_a fit.

- **Vertical Oscillation (vBO)**: similar to the radial oscillation of the beam, this correction accounts for the oscillation in the vertical direction. It is parameterized using four parameters in the same way as the CBO correction:

$$N_{14par}(t) = N_{10par}(t) \cdot \left[1 - A_v e^{-\frac{t}{\tau_v}} \left(\cos(\omega_v t) + \phi_v\right)\right] \tag{3.12}$$

In conclusion, the positron count versus time plot contains many frequencies embedded in the distribution. They can be studied using a Fast Fourier Transform (FFT) technique, as shown in Fig. 3.10, and their typical values are listed in table 3.1.

Frequency name	Symbol	Typical value
Cyclotron	ω_c	6.71 MHz
Anomalous precession	ω_a	0.23 MHz
Coherent Betatron Oscillation	ω_{CBO}	0.37 MHz
Vertical Betatron Oscillation	ω_v	2.19 MHz

Table 3.1: Frequencies expected in the positron hit time histogram. Values are taken from E989 Run 1 [56].

3.4.3 Detector corrections

In addition to the corrections considered in the fitting function of the positron count versus time distribution, other corrections have to be applied prior to the construction of the distribution itself. In fact, while the functions $N(t, E)$ and $A(t, E)$ can be calculated theoretically, the quantities E and t are measured by the detectors, and they contain systematic biases that must be accounted for. Such effects depend on detector hardware and software.
The primary known detector effects of concern are *pileup*, which happens when two or

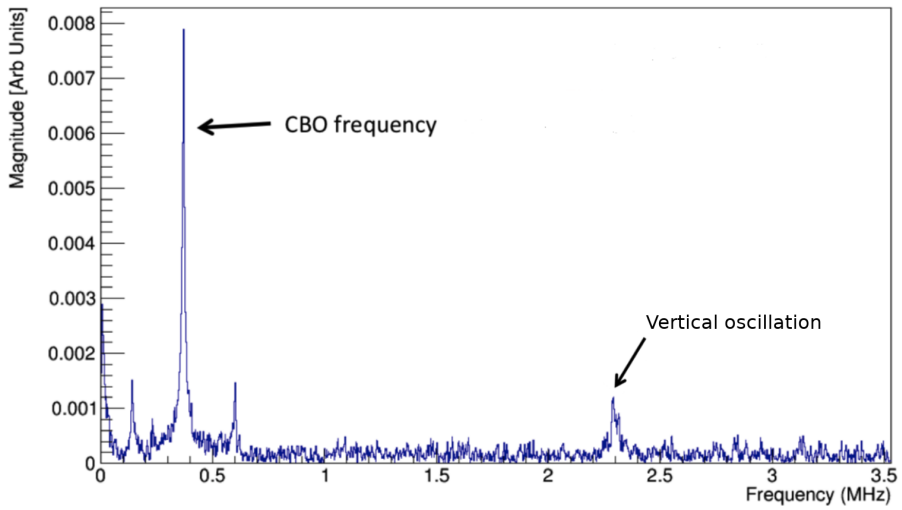

Figure 3.10: Fast Fourier Trasform of the 5-Parameters fit residuals. The two peaks indicated by the arrows correspond to the CBO and vBO oscillation frequencies.

more particles are reconstructed as one, and *gain instability*, which is a time-dependent shift of the conversion factor from positron energy to detected energy. In addition to that, all the 1296 detectors must be precisely synchronized to measure the time arrival of the particles with high accuracy.

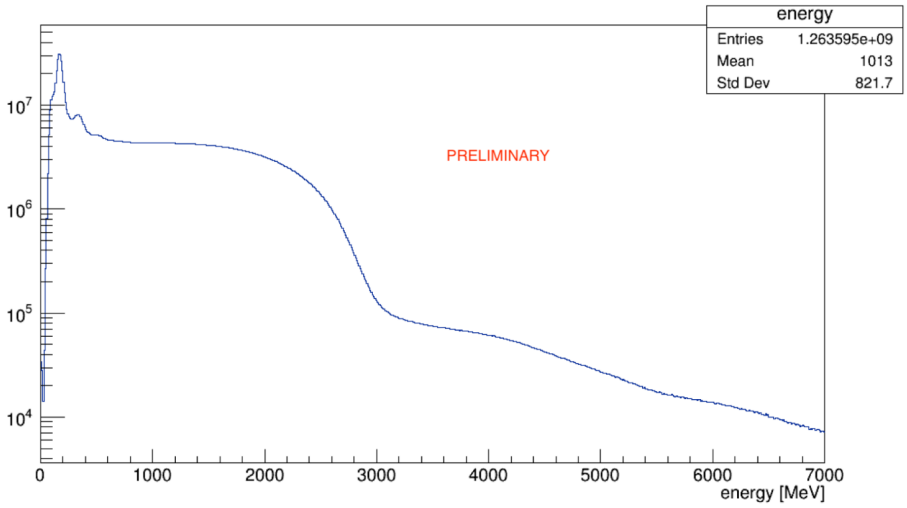

Figure 3.11: Energy spectrum of the positrons as measured by the calorimeters. The end-point should be at ∼3.1 GeV, but the plot shows a long tail due to the pileup events [59].

The pileup is a rate-dependent effect, and distorts the energy spectrum in a different manner between early and late times in a fill. The pileup correction can be evaluated by studying the energy spectrum of the observed positrons. Since the muons have an energy of ∼3.1 GeV, any detected signal with an energy higher of that comes probably from a pileup event, that is two or more positrons producing signal in the same SiPM simultaneously. Figure 3.11 shows the tail of the energy distributions corresponding to these pileup events. The study of this tail is used to obtain a statistical correction to events with all energies. This correction is applied to the wiggle plot before the fit procedure.

Gain is the conversion factor between the physical energy deposition in a calorimeter and the quantifiable detected signal, such as an ADC value. Typically, through a calibration procedure, the gain is measured so the detected signal can be converted back into physical energy units, such as MeV. The gain can vary with external factors such as temperature and hit rate. Gain fluctuation can affect the measured precession frequency if not properly corrected for. In fact, since the T-Method relies on an energy threshold, gain shifts over the course of a fill result in a change in the effective energy threshold, thus affecting the parameters N, A, and ϕ, and indirectly biasing the precession frequency. For example, a decreased gain of the detectors is equivalent to a higher energy threshold. Gain fluctuations were the main source of systematic errors in the E821 BNL experiment. One of the improvements of this new E989 experiment is the installation of an accurate calibration system that uses laser pulses to monitor the gain response of the calorimeters during data taking. These gain fluctuations have effects on various time scales:

- long term (hours, days), due to temperature variations of the environment where the experiment is placed;
- short term (~ 50 μs), due to the muon decay rate that is maximal at the beginning of the muon fills;
- very short term (~ 10 ns), due to the overlap of the positron signals.

The Italian team, sponsored by the Istituto Nazionale di Fisica Nucleare (INFN), is responsible of the construction, the installation, and the maintenance of this Laser Calibration System, that is described in Chapter 4. This thesis work was performed using such system, and conducted in collaboration with the Italian team.

Chapter 4

The Laser Calibration System

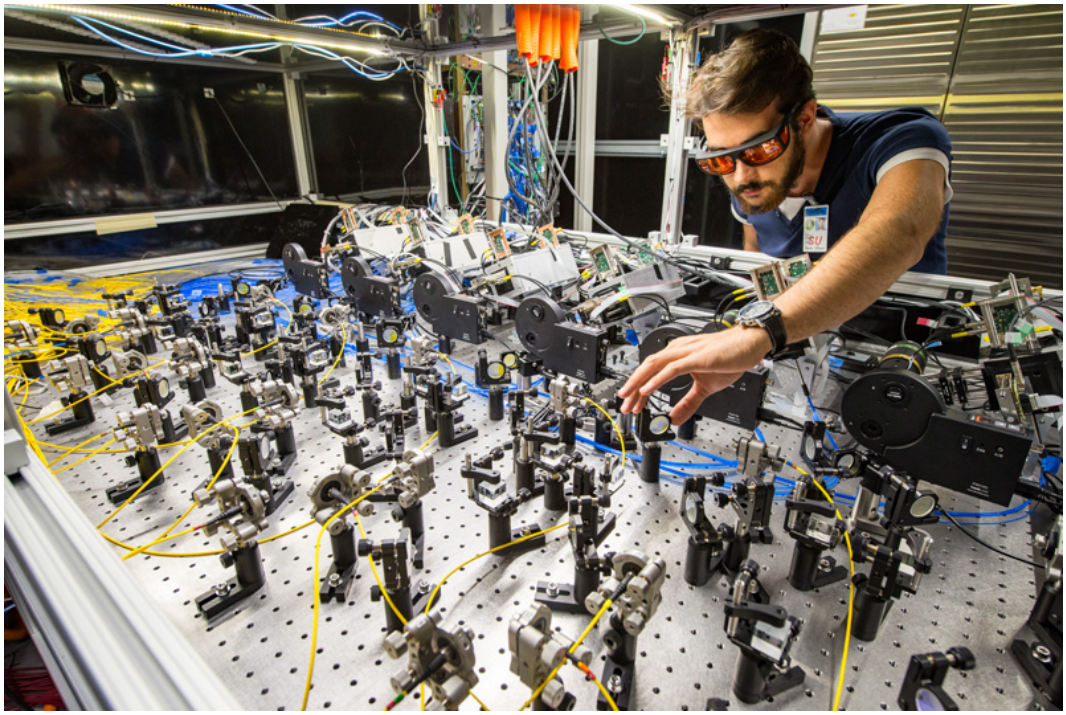

Figure 4.1: The optical table of the Laser Calibration System. On the right: me.

The Muon g-2 experiment at Fermilab (E989) plans to measure the muon anomaly a_μ to an uncertainty of $16 \cdot 10^{-11}$ (0.14 ppm), consisting of a 0.1 ppm statistical error and two systematic uncertainties of about 70 ppm on the spin precession angular velocities of both muons (ω_a) and protons(ω_p) in the same magnetic field. This improves the precision of the BNL E821 experiment by a factor 4. To reach this level of accuracy, systematic

uncertainties have to be lowered with respect to the E821 (BNL) experiment: Table 4.1 lists these errors and the planned goal for the new E989 experiment.
The laser calibration system (Fig. 4.1) is one of the improvements: its main task is to monitor the gain fluctuations of the detectors (SiPM) allowing for a total systematic uncertainty of **20 ppb**.

Error	E821 [ppb]	E989 goal [ppb]
Gain changes	120	20
Lost muons	90	20
Pileup	80	40
CBO	70	40
E and pitch	50	30
Total	180	70

Table 4.1: List of the E821 systematic errors and the planned goal for the E989 experiment [61].

The detector response may vary on both a short timescale of a single beam fill, and a long one of accumulated data over a period of more than one year. To achieve this, the calorimeter gain must be measured and corrected at the level of 0.1% over the time scale of a 700 μs muon fill and at the sub-per cent scale over the longer term of the entire data collection. This is a challenge for the design of the calibration system because the desired accuracy is at least one order of magnitude higher than that of all other existing or past calibration systems for calorimetry in particle physics [62]. In addition, the SiPM response to consecutive positron hits in the time scale of 100 ns must be addressed: this effect is important in particular for the firsts 50 μs of the muon fill, where the decay rate is higher.

The implemented solution is based on the method of sending simultaneous light calibration pulses onto each of the 1296 crystals of the electromagnetic calorimeter. Light pulses should be stable in intensity and timing in order to correct drifts in the response of the crystal readout devices (SiPM). The stability of the laser intensity is monitored with a suitable photo-detector system. The guidelines given by the experiment to define the architecture of the entire system are detailed in [63]. The crucial point for the realization of this system are the light sources and the distribution system.

4.1 The Laser Heads

First of all, since the laser system is used to calibrate the detectors, the light wavelength must be in the range of the calorimeter SiPM sensitivity and the light source must have an adequate power to deliver an appropriate amount of light to all crystals. Then, the light pulses produced by the laser heads must be stable in intensity and timing to correct for systematic effects due to drifts in the response of the SiPMs. For the choice of the light source, the following criteria were used as reported in [15]:

- light wavelength must be in the spectral range accepted by the detector and determined by the convolution of the spectral density of the Čerenkov signal produced by electrons in PbF_2 crystals with the spectral transmission of the crystals, and with the spectral quantum efficiency of the photodetector;
- the energy of the calibration pulses must be in the range of the electron deposit in the crystal, typically 1-2 GeV; this corresponds to a luminous energy of about 0.01 pJ at 2 GeV;
- the pulse shape and time width must be suitable to infer on the readout capability in pile-up event discrimination; pulse rise/trailing time must be of the order of some hundreds of picoseconds, the total pulse width should not exceed 1 ns;
- the pulse repetition rate must be of the order of 10 kHz; this value is obtained searching the best compromise between the need of having enough calibration statistics and the need to avoid saturation of the DAQ bandwidth and perturbation of data due to the laser pulses.

The laser heads used to accomplish these requirements are *LDH-P-C-405M* from Picoquant (Fig. 4.2), with a wavelength of 405 ± 10 nm and a pulse FWHM of < 600 ps. Some of the properties of the laser are listed in Table 4.2.

Property	Value
Wavelength	405 ± 10 nm
Pulse FWHM	700 ps
Average Power (@40 MHz)	28 mW
Power stability	1% RMS, 3% peak to peak (12 h)
Measured light output	1 nJ/pulse at 10 kHz

Table 4.2: Properties of the Picoquant *LDH-P-C-405M* laser sources. [64]

Figure 4.2: The LDH-P-C-405M laser head by Picoquant.

4.2 Distribution system

The task of the distribution chain is to divide and carry the light from the laser source to the different calorimeter stations placed around the ring, preserving as much as possible uniformity and intensity of the laser light source.

4.2.1 The Laser Hut

Right next to the storage ring, a black room called *Laser Hut* houses the electronics and the optical table of the laser calibration system. The reason why this room is located outside the ring is to avoid electromagnetic perturbations of the local field induced by the current flow used to excite the lasers.
A scheme of the optical table is shown in Fig. 4.3. The six laser heads are controlled by the *PDL 828 Sepia II* 8 channel multi-laser driver. First of all, the laser light is split in two by a splitter cube, as described in section 4.3.1, where the reflected beam goes into the Source Monitor. Then, the beam that continues straight passes trough a motorized Filter Wheel, that houses several (12) different transmittance filters. This filter wheel is used to regulate the amount of light reaching the SiPMs. After that, the beam is split in four beams and coupled to quartz fibers. These fibers, called *launching fibers* are 25 m long and bring the light to all the 24 calorimeters inside the storage ring. A new piece of equipment has been installed on the optical table, as described in chapter 6, not shown in the figure 4.3.

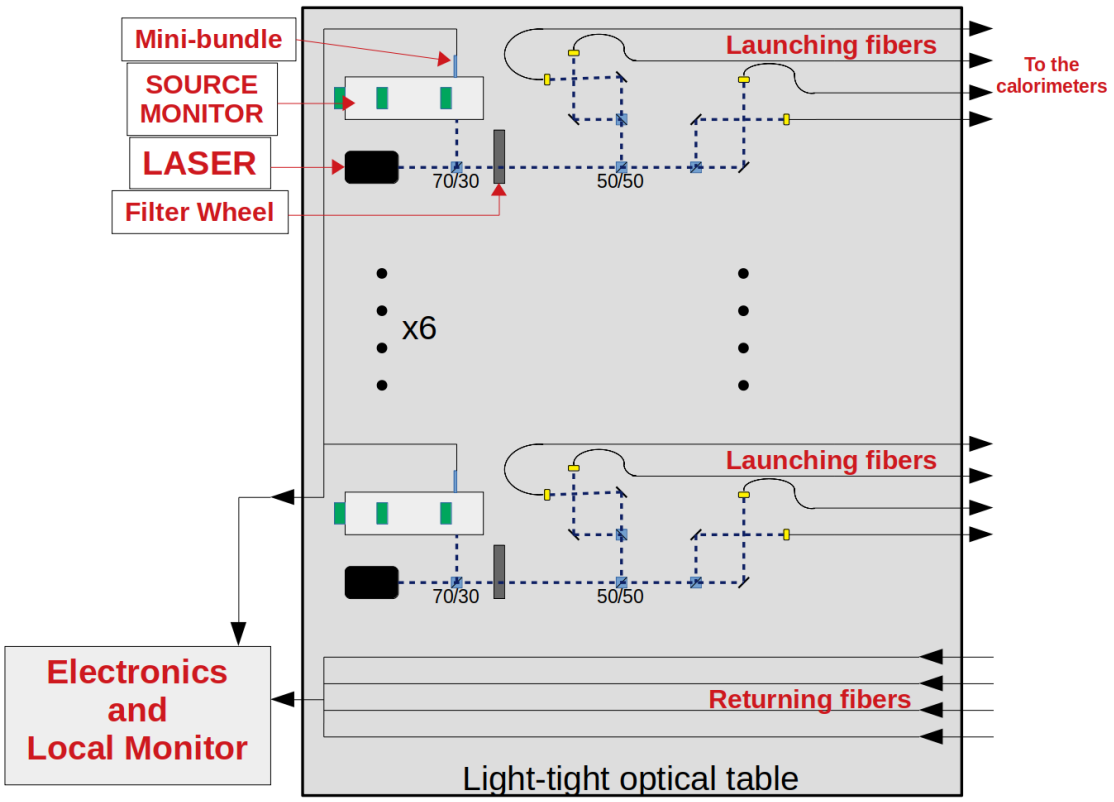

Figure 4.3: Schematic of the optical table inside the Laser Hut. Most of the major components are shown and labeled.

4.2.2 Connection to calorimeters

At the calorimeter end of the launching fibers, the light enters in a light distribution box (Fig. 4.4 where the light exits the fiber and then goes through a collimation lens and an engineered diffuser (*Thorlabs ED-20*) which tailors the light intensity from the fiber to a flat top profile. After the diffuser, the light illuminates a fiber bundle containing 54 one meter long fibers, that bring the light to each crystal of the calorimeter via a light distribution plate. This plate is made of 1 cm thick plastic material (*Delrin*) and is placed in front of the calorimeter crystals. Other than providing the calibration signal, this plate also holds the crystals in place from the front side. There are, in each plate, 54 total channels where fibers are inserted. At the end of each channel (and fiber) an optical prism steers the light at 90 degrees into the crystal it is facing. The light illuminates then each of the 54 PbF_2 crystals in every of the 24 calorimeter stations. In addition to the fiber bundle just mentioned, the diffused light illuminates two more 25 m long fibers,

one made of quartz and the other made of PMMA. These two fibers are sent back to the laser hut where their light is measured by the *Local Monitor*.

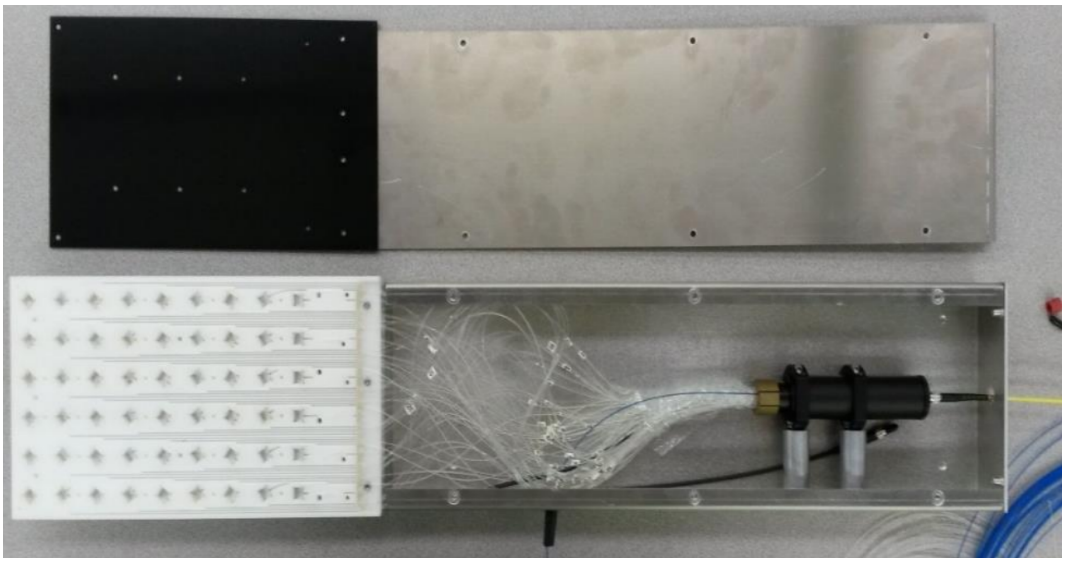

Figure 4.4: Light distribution box of one calorimeter. The launching fiber (yellow) on the right brings the light from the Laser Hut. The white panel on the left distributes the light to the 54 crystals.

4.3 Monitors

The intensity variations of the light source used for calibration are monitored by a monitor called Source Monitor (SM), while the intensity variations in the light distribution are monitored by the Local Monitor (LM).

4.3.1 Source Monitor

The light from each laser is divided just after the source with an unbalanced beam splitter in two (70%-30%) where the lower intensity beam goes to the SM. The other beam continues straight trough the Filter Wheel and then toward the remaining splitting optics.

The SM consists of a commercial integrating sphere (*Thorlabs IS200*) equipped with two large area (1 cm^2) photodiodes (*Hamamatsu S3590-18*) and one PhotoMultiplier Tube (PMT) (*Hamamatsu H5783*). In addition, a low activity (6 Hz) Am source coupled to a NaI crystal illuminates the PMT, thus providing an absolute calibration reference.

A *mini-bundle* of fibers is attached to one of the integrating sphere's ports; it consists of ten 3 m long fibers that brings some of the light to the Local Monitor PMTs. This direct signal is compared in the LM with the delayed signal that has made a round trip to the calorimeters. For the SM a custom made electronics has been made which is integrated with the optics and detectors. Everything is placed in an aluminum housing that provides a large thermal inertia. A schematic of the source monitor is shown in figure 4.5.

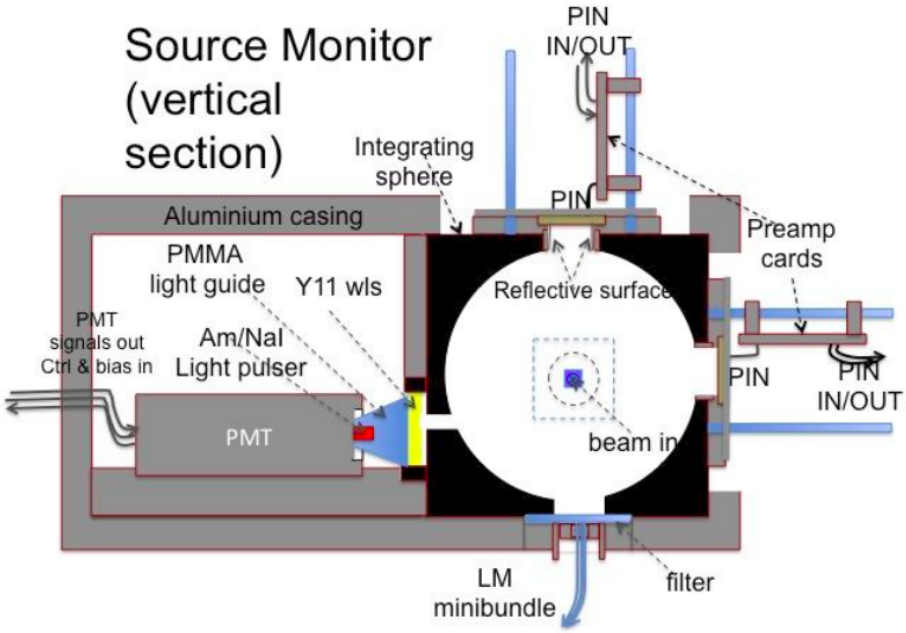

Figure 4.5: Schematic of the vertical section of one source monitor.

4.3.2 Local Monitor

As mentioned earlier, two fibers return to the Laser Hut from each calorimeter. The light coming from those is measured by the Local Monitor. The principal component is a *Photonics XP2982* PMT that receives two laser pulses. The first one is a reference signal that comes from the SM thanks to the mini-bundle, while the other is the one coming from the calorimeters and is representative of the calibration signal sent to the calorimeters. The PMTs are contained in custom made cases which hold 10 tubes each and signal conditioning electronics.
Before reaching the PMTs, the light passes through an interferential band-pass filter centered at 405 nm, with 10 nm half width, which filters out possible background light

coming from other sources than the lasers themselves. The two signals, which are produced by the same laser pulse, are separated by about 250 ns (Fig. 4.6) since the first only travels from the SM to the PMTs with 2 m long fibers and the second goes to the calorimeter and back, traveling trough a 50 m fiber. Two pulses can be directly com-

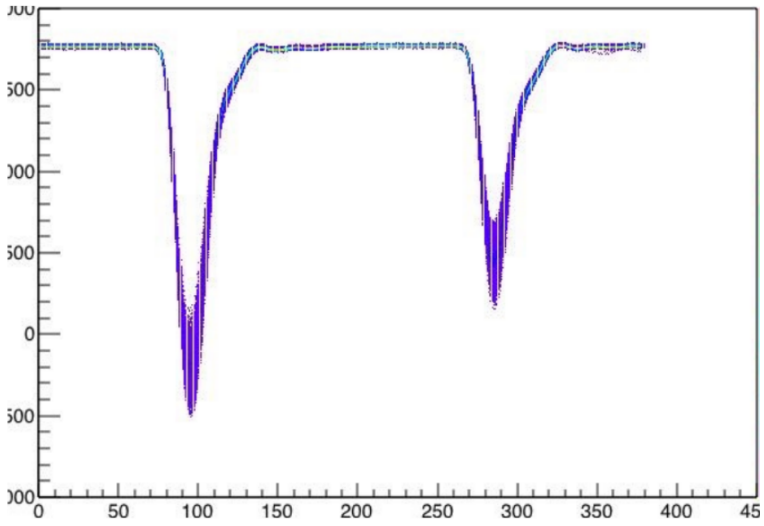

Figure 4.6: Typical plot of a Local Monitor PMT signal [65]. The first pulse comes from the SM mini-bundle, while the second has traveled to and from the calorimeters.

pared since the expected gain fluctuations of a PMT at this timescale are negligible. In order to study and compensate for any fluctuations due to temperature of the transmission coefficient of the local monitor optical fibers, two types of fiber materials are used: quartz and PMMA. The system is redundant, and allows to monitor any aging effect of the PMMA fibers [65].

4.4 Operating modes

The laser is operated in two distinct modes. The first is enabled during physics runs with the muon beam, and used to correct for systematic gain variation of the SiPMs caused by the varying muon decay rate and the flash of particles at the beginning of the muon fill. The second is devoted to the test runs, without beam, in order to exercise the detector and DAQ with specific laser pulse time sequences and to study the SiPM response to double pulses. This latter operating mode is new and developed and tested as discussed in chapter 6. Also, the laser data taken during beam is used for time alignment of the SiPMs in a calorimeter and between calorimeters. This type of study has performed as

described in chapter 5.
A dedicated and custom electronic board, the Laser Control Board (LCB) allows the following operating modes:

- Calibration mode, or generation of *in-fill* pulse trains, at programmable frequencies, superimposed on the physics data provided in a 700 μs muon fill. To sample homogeneously the gain of SiPMs at different points in the muon fill, the pattern is shifted at each fill by a fraction of the pulse period (Fig. 4.7. The measured early-to-late gain perturbation is used to correct reconstructed pulse energies during analysis. The number of samples at each point is determined by the calibration goal of a 10^{-4} relative error, that allows an ultimate gain systematic uncertainty of less than 20 ppb.

- Physics event simulation, or operation in "flight simulator" mode, entails triggering the laser according to the exponential decay time function $e^{-t/\tau}$ expected in the experiment due to muon decay. In fact, an essential feature of the LCB is the capability of generating pulses, or triggering the laser, according to any time distribution. This mode provides flexible testing of the SiPMs to determine, for example, their response linearity and gain stability. Moreover it allows fully realistic tests of the readout electronics, DAQ and data processing.

- Synchronization of detectors and electronics by providing a reference pulse on request, or in connection to an accelerator machine signal produced as the muon beam approaches the storage ring.

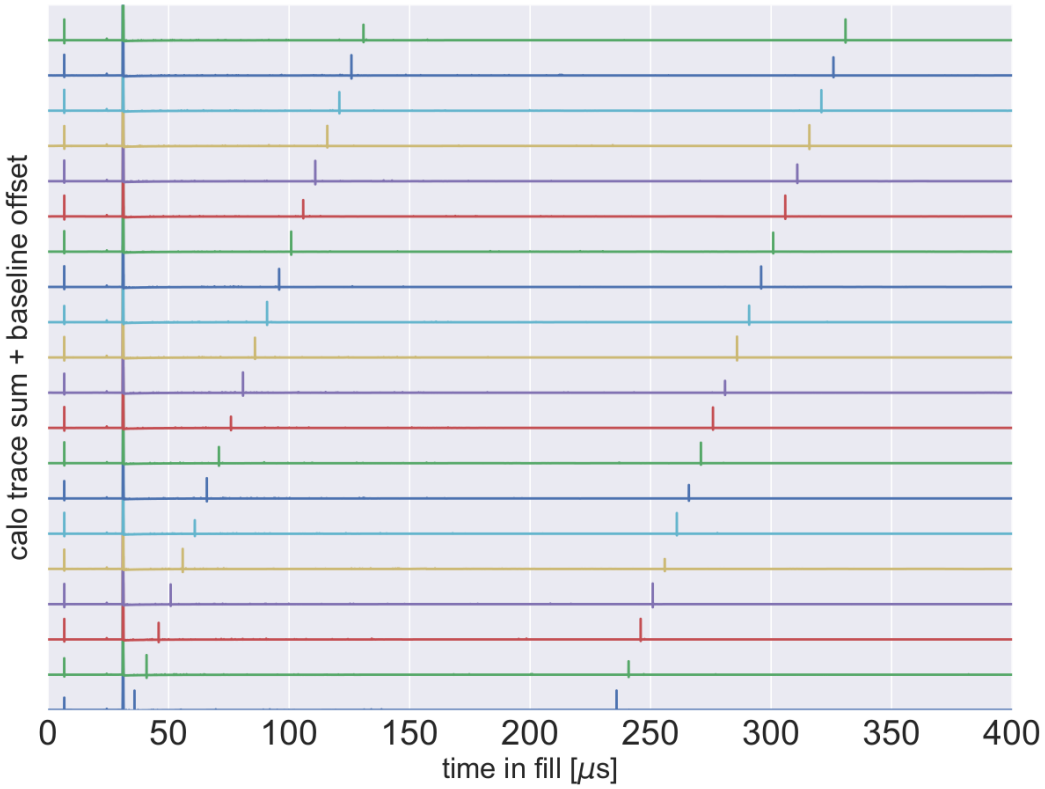

Figure 4.7: Pattern of laser pulses for various muon fills [56]. Each curve is the sum of all SiPM voltage signals, or traces, within a given calorimeter across the first 400 μs of a muon fill. Within each trace, there are four clear pulses: the first is the *sync pulse* used for timing synchronization on all fills, the second and largest pulse is the beam injection, and the last two pulses are the in-fill laser pulses. Each subsequent vertically offset curve is the next fill in which in-fill laser pulses appear.

Chapter 5

The time synchronization of the detectors

The precise measurement of the precession frequency relative to momentum, ω_a, requires an extremely precise determination of the response of each detector, in particular what regards the energy calibration and the time synchronization.

This chapter discusses how well the relative time synchronization among the SiPMs can be determined by using the laser *sync* pulse, a flash of light issued by the laser calibration system a few microseconds before muon injection, together with positron signals and *lost muons*, i.e. muons which are scraped out of the beam path and spiralize inward, hitting the calorimeters.

This work is an independent check on the synchronization constants used within the reconstruction software, described in [66] and [67].

At the end we will see that the relative synchronization can be determined at the level of ~ 100 ps, being limited by the time spread of electromagnetic showers within a calorimeter. This value is much smaller than the sampling frequency, which is $\Delta t = 625$ ps, and it is highly reproducible at the level of ~ 10 ps among different runs throughout the data taking period.

5.1 Hardware induced delays

Whenever the laser calibration system is prompted to fire a light pulse, the Laser Control Board (LCB) sends two signals to a NIM crate that, after some logic gates, sends six outputs to the Sepia-II driver, which triggers the six laser heads on the optical table. As shown schematically in Fig. 5.1, the laser light of each head is then split into four beams and sent to four calorimeters via a 25 m long *launching fiber*. Each one of those fibers encounters a diffuser that spreads the light (almost) evenly to a bundle of 54 fibers, which finally convey the light to each crystal through a set of reflecting prisms mounted on a panel. Due to the mechanical structure of the system, the 54 fibers are cut into three groups of different lengths: 45-55-65 cm. The light gets then detected by the SiPMs and the signals are sent to the waveform digitizer via HDMI cables.

This complex structure makes it obvious that when a trigger is provided, the light does not reach each crystal (and the digitizers) at the same time. We can divide this long journey into three main sections: the launching fibers (that also contains the trigger-to-laser path), the fiber bundles, and the SiPM signal paths. To correctly synchronize the output pulses, it is necessary to accurately measure the relative delays between the SiPMs and the waveform digitizers, so that it would be possible to correct the time measurement of the positron signals.

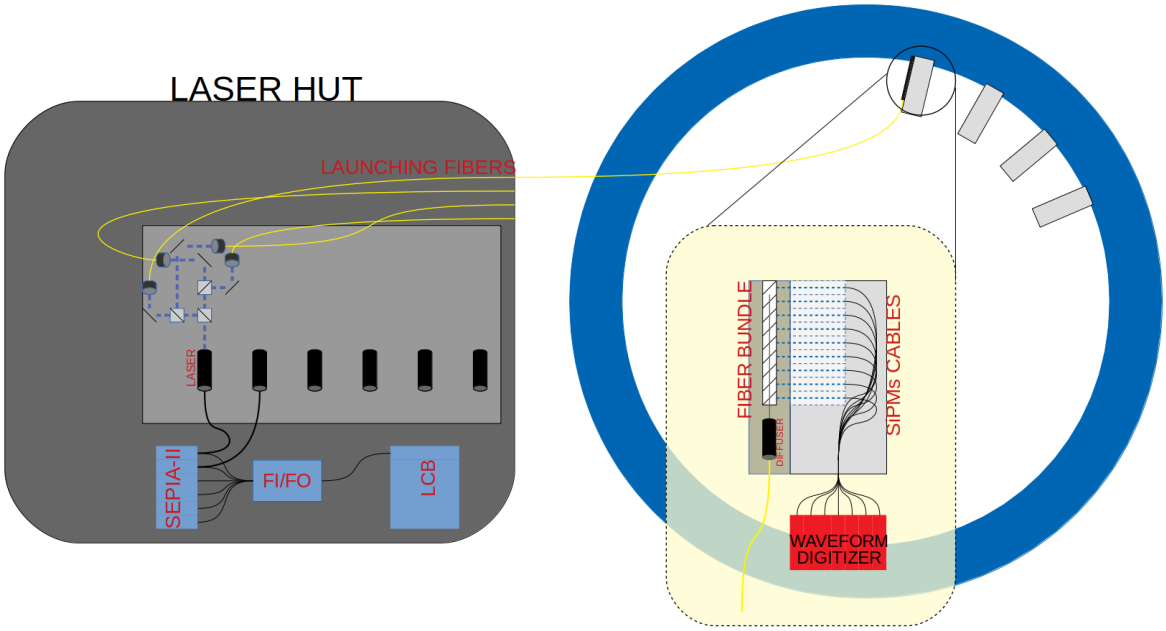

Figure 5.1: Schematic sketch of the overall structure of the laser system.

5.2 The Fiber Bundles

To derive the delays due to the fiber bundles, we assume that signals from positron showers reach all involved SiPMs at the same time. Monte Carlo simulations show that this statement is correct at the level of ~ 100 ps (see [68]).

The measured arrival time of a laser pulse for each crystal (t_i, where i runs from 0 to 53 for each calo) can be written as

$$t_i^L = t^{trigger} + T_i^{fiber} + T_i^{bundle} + T_i^{signal} \tag{5.1}$$

where $t^{trigger}$ is the time the trigger fires, which is the same for every crystal and can be defined as 0. T_i^{fiber} is the travel time inside the launching fiber and it is the same for every crystal belonging to the same calorimeter. Since positron events are calorimeter-confined, also this can be set equal to 0. T_i^{bundle} is the time needed from the light to go from the diffuser to each SiPMs, and T_i^{signal} is the one from the SiPMs to the Waveform Digitizer. t_i^L is the value measured by the digitizer and expressed in clock ticks.
In a similar way, the measured time of a positron hit is

$$t_i^+ = t^+ + T_i^{signal} \tag{5.2}$$

where t^+ is the true time of the positron hit. For two crystals (i & j) belonging to the same positron shower, we have

$$t_j^+ - t_i^+ = T_j^s - T_i^s \equiv \delta_{ij}^{signal} \tag{5.3}$$

since the positron arrival time t^+ is the same. Normally the time difference δ_{ij}^{signal} is constant, but, due to the digitizer jitter, a difference as large as ± 2 c.t. can be observed. This eventual difference is however constant within a muon fill.
By subtracting 5.1 from the equation 5.2:

$$t_i^+ - t_i^L = t^+ - T_i^{bundle} \tag{5.4}$$

that actually means to subtract the sync pulse time from all the positron events of the same fill, we then get

$$-\delta_{ij}^{bundle} = t_j^+ - t_j^L - t_i^+ + t_i^L \equiv t_j^{+,L} - t_i^{+,L} \tag{5.5}$$

where $t^{+,L}$ is the positron arrival time with respect to the laser synchronization pulse.

The delays δ_{ij} can then be evaluated with respect to a reference crystal. We choose crystal 22 because it is one of the central ones and this is convenient from a statistical point of view. We therefore define δ_i as

$$\delta_i = \delta_{22i} = t_i - t_{22} \tag{5.6}$$

so that $\delta_{22} = 0$.

We used two different methods to calculate the δ_i^{bundle}, as described in the next two subsections.

5.2.1 The adjacent method

We first look at every positron event and collect the time difference between two adjacent crystals (horizontally and vertically), when they are hit by the same shower. The distributions obtained (Fig. 5.2) for each crystal pair are Gaussian, with the variance reflecting the pulse fitting uncertainty (∼50 ps) and the mean representing δ_{ij}.
To evaluate the δ_i with respect to the reference crystal we can propagate (sum) the δ_{ij} and their errors starting from the reference one to crystal i. Many paths allow to reach crystal i from the reference one, leading to different values of δ_i. The spread of these values is smaller than 100 ps. As an example, in Fig. 5.3 the δ_i obtained by following two sample paths are shown.

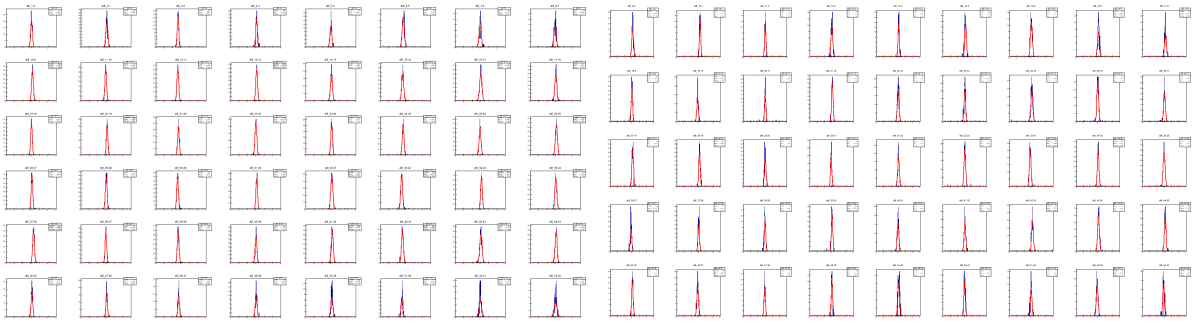

(a) Horizontal time difference between adjacent crystals of calorimeter 10.

(b) Vertical time difference between adjacent crystals of calorimeter 10.

Figure 5.2: Example of the time difference distributions.

The result of this technique is shown in Fig. 5.3, for calorimeter 10. The δ_i calculated using the two different paths are similar, with a maximum difference of ∼50 ps which

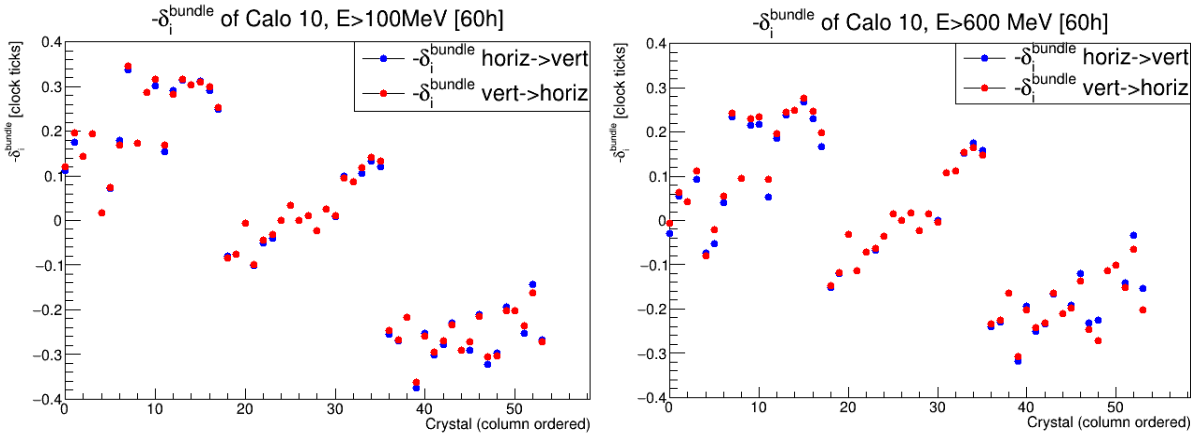

Figure 5.3: δ_i^{bundle} for calorimeter 10 calculated with the adjacents method. For the blue dots δ_i is evaluated by propagating horizontally first and then vertically (see text). The opposite happens for the red dots. A cut on the energy of each crystal is applied: E>100 MeV in the left figure and E>600 MeV in the right one.

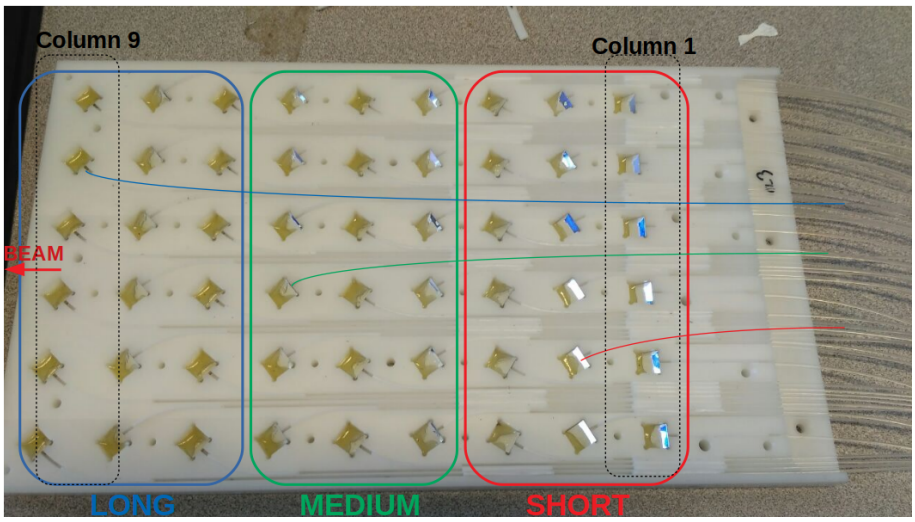

Figure 5.4: Photo of the fiber bundle panel. The different fiber lengths are highlighted.

can be considered an upper limit of the precision of this method. The crystals in this plot are ordered by column, from column 1 to 9, as in Fig. 5.4. The three visible groups of δ_i reflect the fact that the fibers in the bundle are of three different lengths. The points within the same group show a dependency on the column number, probably due to different light paths in the crystals caused by different reflection angles.

Some cuts on the dataset are applied, in particular:

1. cluster time > 50 μs, to avoid pileup events;
2. cluster energy > 1.2 GeV;
3. crystal energy $> E_{thr}$.

Figure 5.3 shows the distribution of the time correction terms for two different values of E_{thr}, corresponding to different topologies: when $E_{thr} = 100$ MeV the energy is normally concentrated in the central crystal, while in the case of $E_{thr} = 600$ MeV it is more evenly distributed. The relative delays change between the two topologies at the $50 - 100$ ps level, which reflects the fact that the assumption of a perfectly synchronized response of the SiPMs to an EM shower is only correct at this level. We can assume an induced systematic error of 100 ps.

5.2.2 The χ^2 method

A more sophisticated method has also been used: its concept is to calculate all the δ_i at the same time. This is done building a function similar to a χ^2 test (hence the name) as seen in [67]:

$$f_{\chi^2} = \sum_{+} \sum_{i} \frac{(t^+ - t_i^+ + \delta_i)^2}{\sigma_i^2} \tag{5.7}$$

where t^+ (without subscript) is now a variable that represent the true arrival time of the cluster, with the condition that

$$\delta_{22} = t_{22}^+ - t^+ = 0 \tag{5.8}$$

We have to find the δ_i and t_i^+ values which minimize f_{χ^2}. Setting the partial derivatives to zero we obtain

$$\frac{\partial f_{\chi^2}}{\partial \delta_i} = 0 \;\rightarrow\; \sum_{+} t^+ + N_i \delta_i = \sum_{+} t_i^+ \quad \text{(53 equations)} \tag{5.9a}$$

$$\frac{\partial f_{\chi^2}}{\partial t^+} = 0 \;\rightarrow\; \sum_{i} \delta_i + N_+ t^+ = \sum_{i} t_i^+ \quad (n_{e^+} \text{ equations}) \tag{5.9b}$$

where N_i is the number of times that the crystal i is hit by all the positron events, and N_+ is the number of crystals hit by a single positron event. We then have a set of 53 (that is 54 minus the equation with $i = 22$) plus n_{e^+} linear equations, where n_{e^+} is the number of positron showers used in the analysis. Due to statistical and computational limitations, we filter the run so that each crystal appears in at least 500 clusters and the overall number of equations is around 15000. This enormous linear system can be considered as a square symmetrical matrix, mostly diagonal and very sparse. To solve this system, a matrix inversion is computationally prohibitive, since it scales roughly as $\mathcal{O}(n^3)$. The ROOT class `TMatrixDSparse`, built specifically to handle this kind of matrices, helps to solve this very efficiently.
This method finds all the δ_i at once, without having to propagate them inside the calorimeter, but it is limited by the dimensions of the matrix.

In Fig. 5.5 the χ^2 solution for calorimeter 10 is shown, with the adjacent method results for comparison.

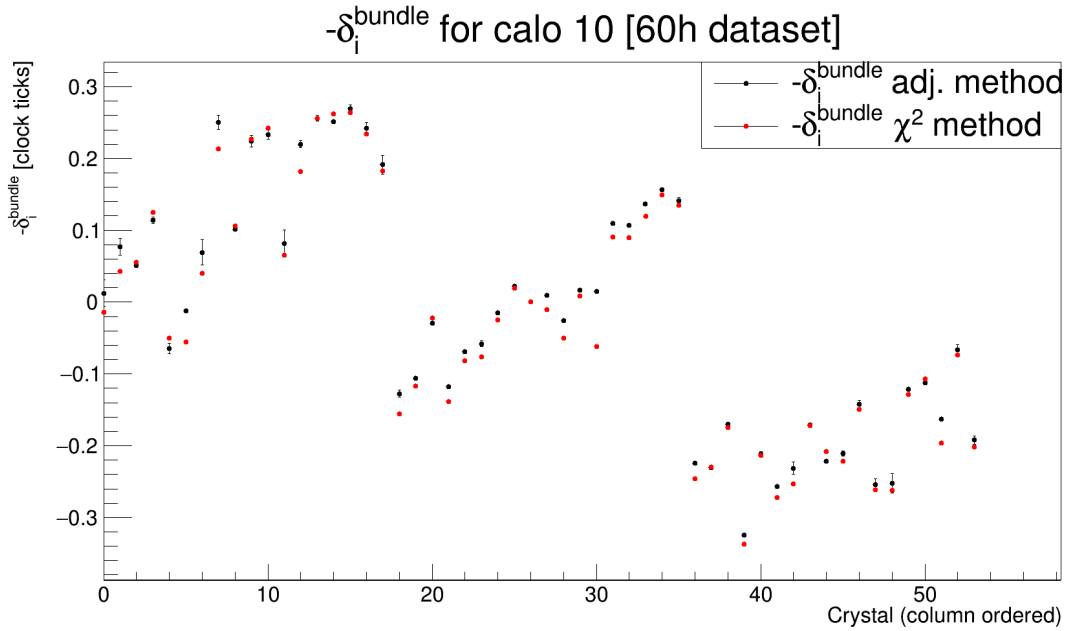

Figure 5.5: δ_i^{bundle} for calorimeter 10 calculated with the χ^2 method. The δ_i calculated with the adjacent method are superimposed for comparison.

5.2.3 Comparisons

Calculating the δ_i^{bundle} for different runs and methods we can compare the results. Calorimeter 10 is shown as example.
The adjacent method is very stable as shown in Fig. 5.6. The values agree very well for each run, even for the crystals that showed some difference in the propagation path of the δ_{ij}. However, the χ^2 method is less stable, as visible in Fig. 5.7, probably due to systematic correlations that arise at the calorimeter level. The spread of the values is of the order of 200 ps, in particular for the crystals near the beam (crystal number > 35).

We now average the values found in different beam runs for each method, and compare them with the ones found in [66] (*ref*), as shown in Fig. 5.8. Plotting the difference with respect to the ref values, we see a good agreement (< 50 ps) for the adjacent method, with a slight deviation in the columns 1-3 (short fibers). The values of the χ^2 method do not have the same level of agreement, showing some deviation in the long fibers and a row correlation in the short fibers.

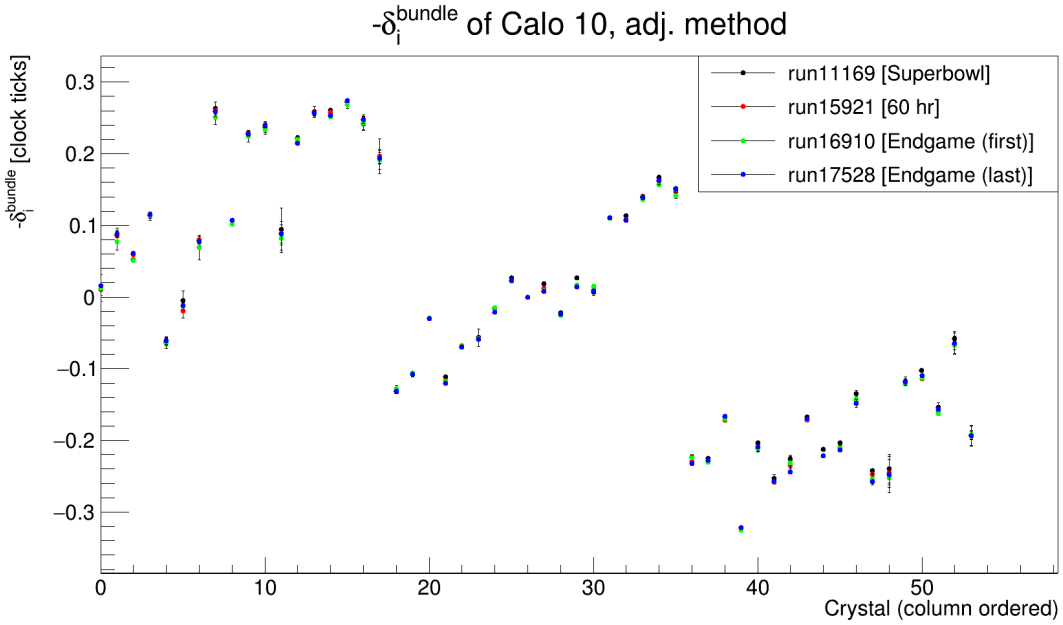

Figure 5.6: Comparison of the δ_i of Calorimeter 10 calculated with the adjacent method for 4 different runs.

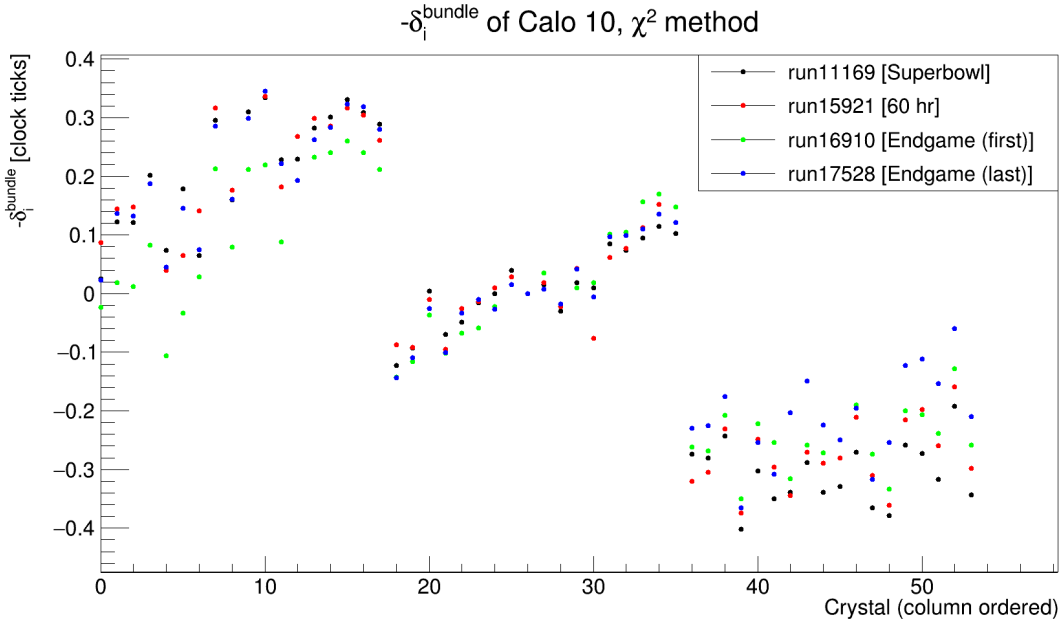

Figure 5.7: Comparison of the δ_i of Calorimeter 10 calculated with the χ^2 method for 4 different runs.

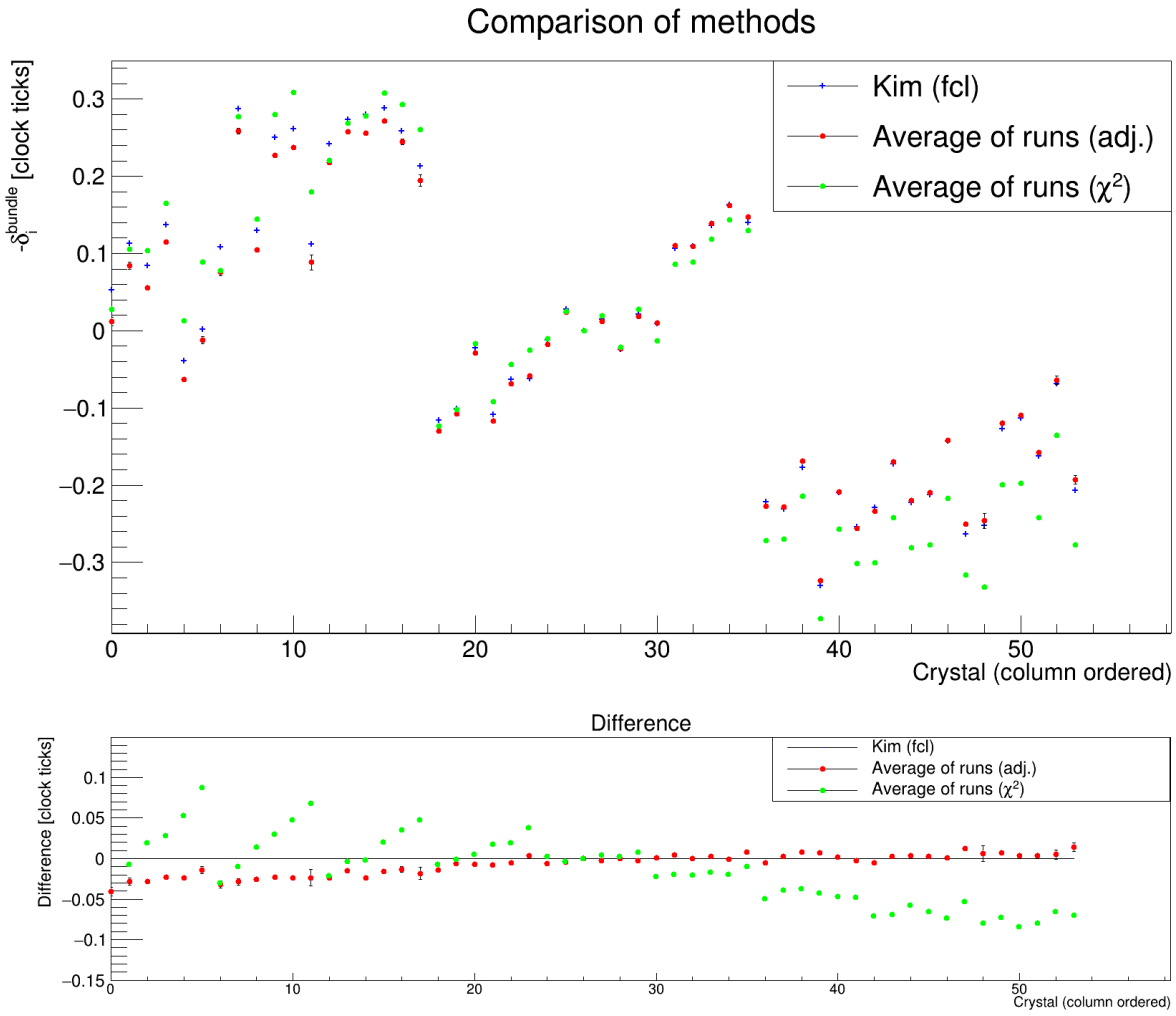

Figure 5.8: Comparison of the δ_i of Calorimeter 10 calculated between the two methods and the reference (here named `Kim (fcl)`). The plot below shows the difference with respect to ref values.

5.3 The Launching Fibers

Now that the time correction of the crystals within a calorimeter is found, we can synchronize different calorimeters using lost muons events. Some muons, specially in the firsts microseconds of each fill, are scraped from the beam. They start to curl inward, hitting some calorimeters before decaying. These events have a particular signature: the muons mostly hit only one crystal per calorimeter depositing an energy typical of a MIP. The muons travel at 0.9994c ($\gamma = 29.3$), making one full turn of the ring in 149.1 ns. So the average Time of Flight (TOF) between two consecutive calorimeters is 6.21 ns.

To solve this new problem we can use two methods in a complete analogy to the previous section. As before, we can build the time equations for laser and muon events:

$$t_i^L = t^{trigger} + T_i^{fiber} + T_i^{bundle} + T_i^{signal} \tag{5.10}$$

$$t_i^\mu = t^\mu + T_i^{signal} \tag{5.11}$$

As before we can now subtract eq. 5.10 from eq. 5.11 obtaining

$$t_i^\mu - t_i^L = t^\mu - T_i^{fiber} - T_i^{bundle} \tag{5.12}$$

that is, for two different crystals i & j

$$t_j^\mu - t_j^L - t_i^\mu + t_i^L = t_{TOF} - \delta_{ij}^{fiber} - \delta_{ij}^{bundle} \tag{5.13}$$

We finally have the 23 equations for the launching fibers:

$$-\delta_i^{fiber} = t_i^{\mu,L} + \delta_i^{bundle} - nt_{TOF} - t_{22|22}^{\mu,L} \tag{5.14}$$

where the subscript i of the last term is written as $XX|YY$, where XX is the calorimeter (1-24) and YY is the crystal (0-53), e.g. crystal 7 of calo 14 is 14|07. nt_{TOF} is the time of flight (theoretic or real) of the muon between crystals i and 22|22, and n is their distance in calorimeter units, i.e. $XX - 22$.

Relativistic muons hit two consecutive calorimeters at a time difference $\Delta t \sim$6.25 ns. In this analysis, a muon track is required to cross a single crystal and to deposit the typical MIP energy. An energy cut of $120 < E_{hit} < 220$ MeV is applied, as show in Fig. 5.9.

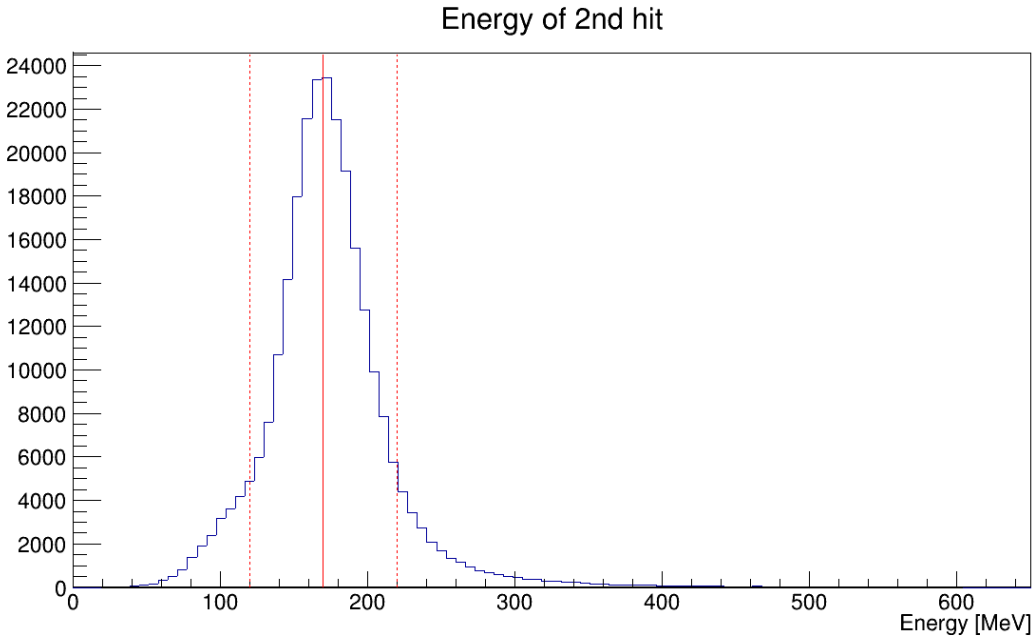

Figure 5.9: Uncut energy spectrum of the double coincidence of adjacent calorimeters. The red lines represent the applied 170 ± 50 MeV cut.

As the calorimeter response is not yet synchronized, a strict time cut cannot be applied and events are accepted if $|\Delta t| < 30$ ns. Residual background due to low-energy positrons misidentified as muons, or independent muons falling in the coincidence window, has a flat distribution in time and it is eliminated during the analysis by imposing the constrain $\Delta t = 6.21$ nsec, as described in the next section.

5.3.1 The TOF method

The TOF method is very similar to the one shown in section 5.2.1: the δ_{ij}^{fiber} are calculated collecting the measured TOF times of each pair of adjacent calorimeters and removing the average TOF of all the pairs (Eq. 5.15). In fact, the sum of all the δ_{ij} going around the ring must be zero, therefore the average of the measured TOF should approach the true value of 6.21 ns.

$$-\delta_{i,i+1}^{fiber} = t_{i+1}^{\mu,L} + \delta_{i+1}^{bundle} - t_i^{\mu,L} - \delta_i^{bundle} - \langle t_{TOF} \rangle \tag{5.15}$$

In Fig. 5.10 the distribution of the time difference between calorimeters 7 and 8 is plotted, after correcting each crystal time according to Eq. 5.15. The mean of the peak

is shifted with respect to the average t_{TOF}: the difference is the δ_{ij} of the corresponding launching fibers. In Fig. 5.11 it is possible to see the effect of these corrections on the TOF times of all calorimeters. In particular, Fig. 5.11a shows the distribution of the difference $t^{\mu}_{i+1} - t^{\mu}_{i}$ for each calorimeter. In Fig. 5.11b the laser sync pulse is subtracted and in Fig. 5.11c the fiber bundle correction is applied, narrowing the distributions at each step.

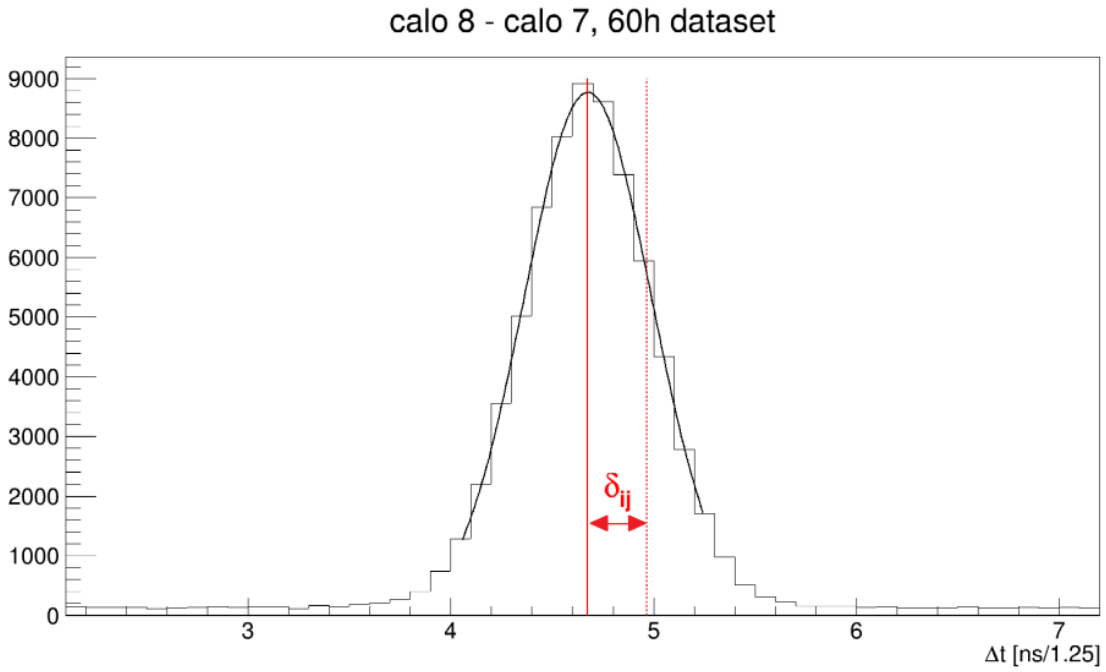

Figure 5.10: Spectrum of the TOF between two adjacent calorimeters. The red dashed line is the muon flight time (6.21 ns). A flat and small background is visible.

Taking as a reference calorimeter 22, Fig. 5.12 shows the correction terms to be added in order to synchronize the response among all the calorimeters. This method is very stable and similar values are found for different runs. The measured correction terms are grouped in four, each group corresponding to a laser head. The pulse from laser 1 (first four calorimeters) is delayed by ∼3 ns with respect to the others. This value is within specifications, but it must be corrected for in order to synchronize the global response.

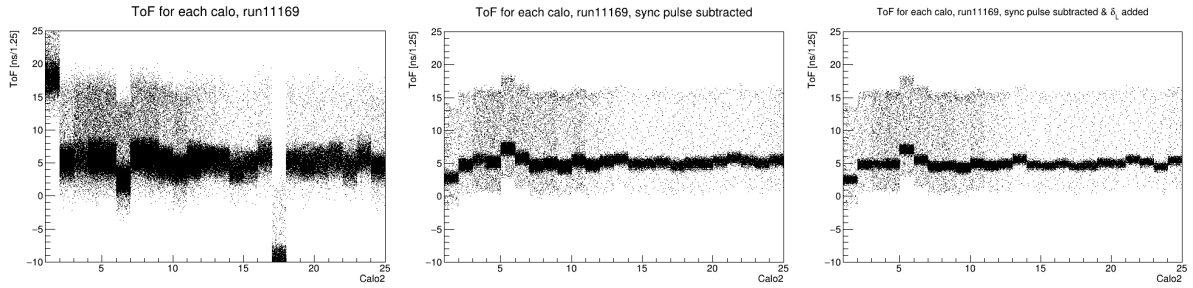

(a) Raw TOF times (b) TOF - t^L (c) TOF - $t^L + \delta_i^{bundle}$

Figure 5.11: Sequence of corrections to the raw TOF times, according to eq.5.15, for each calorimeter.

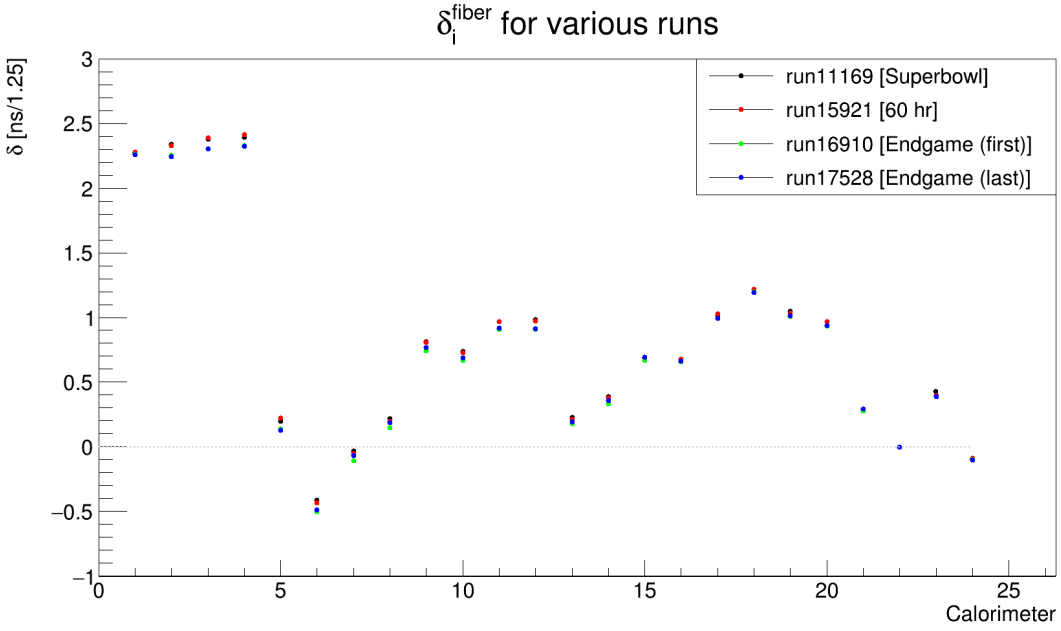

Figure 5.12: δ_i^{fiber} for each calorimeter, calculated with the TOF method for four different runs.

5.3.2 The χ^2 method

Since the problem is very similar to the positron one, we can also use the χ^2 method, with the function slightly modified in order to accommodate for the muon travel time t_{TOF}:

$$f_{\chi^2} = \sum_{\mu} \sum_{i} \frac{(t^{\mu} - t_i^{\mu} - \delta_i^{bundle} + nt_{TOF} + \delta_i)^2}{\sigma_i^2} \tag{5.16}$$

Setting the partial derivatives to 0 we now have 24 (that is 23 for the δ_i plus one for the t_{TOF}) + n_μ equations.
Solving this system of equations the same way as in section 5.2.2 we obtain the 24 values shown in Fig. 5.13. This method is quite stable, with the exception of few points that are different for calorimeters 6 and 17.

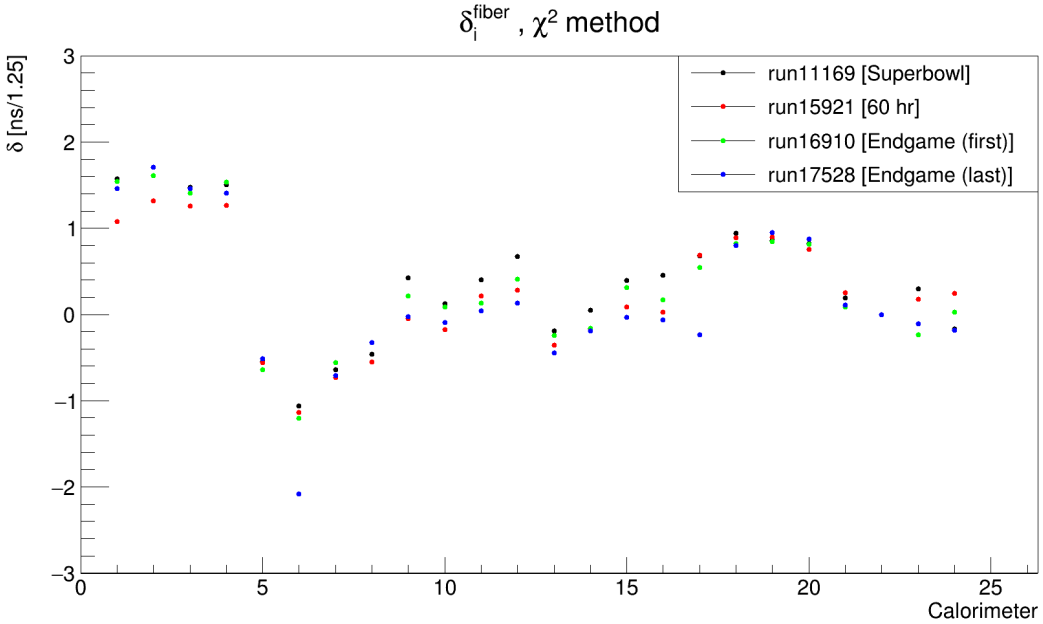

Figure 5.13: δ_i^{fiber} for each calorimeter, calculated with the χ^2 method for four different runs.

5.3.3 Comparisons

We now average the values found in different runs for each method as done in section 5.2.3, and compare them with [66], as shown in Fig. 5.14. Plotting the difference with respect to the ref values, we see a better agreement (< 200 ps) for the TOF method with respect to the χ^2 one, that shows a big deviation of the order of 1 ns in the firsts calorimeters.

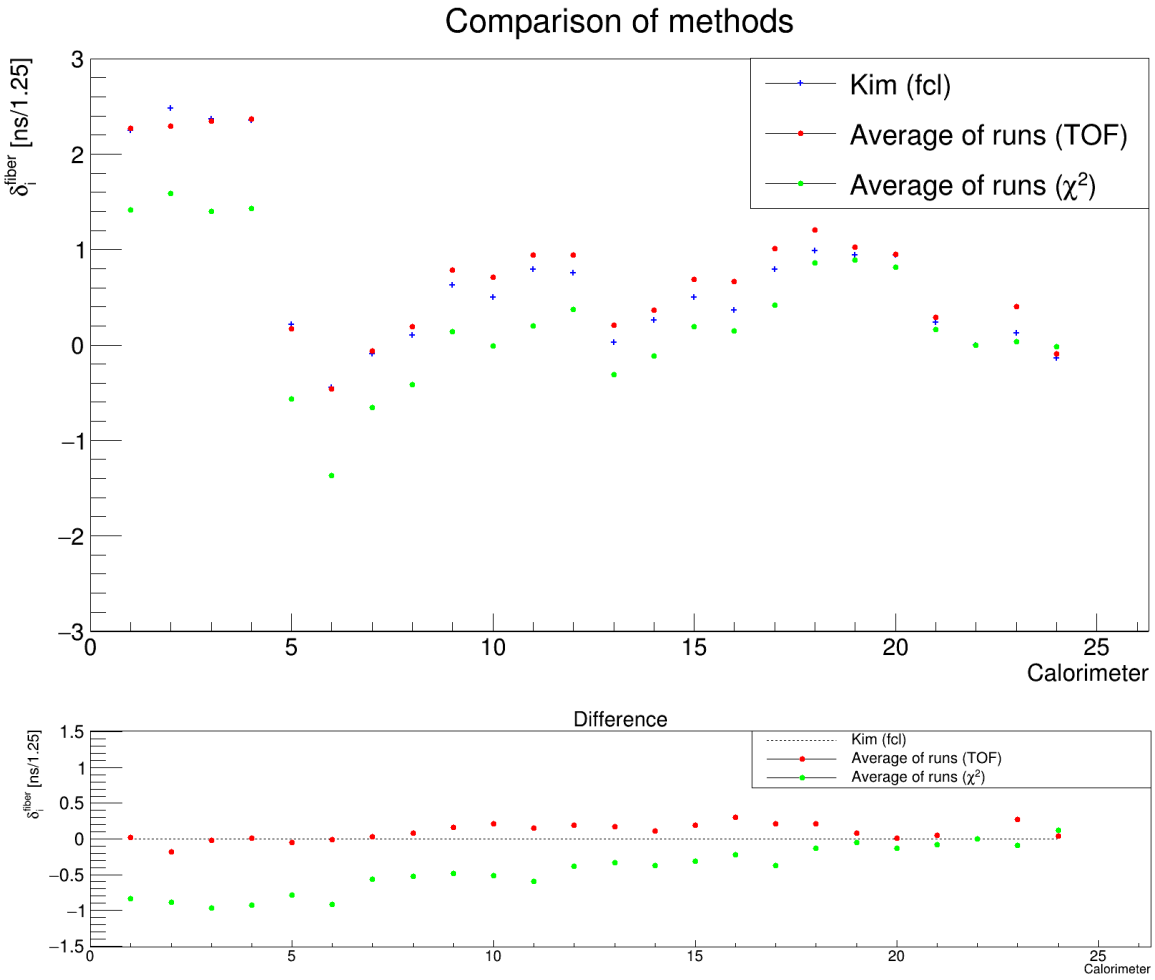

Figure 5.14: Comparison of the δ_i^{fiber} between the two methods and the reference. The plot below shows the difference with respect to the reference values.

5.4 Hardware measurement

At the end of July 2018, one month after the data taking, we have tried to measure the δ_i^{fiber} directly in the ring with an oscilloscope. Each calorimeter is equipped with a probe fiber connected to the diffuser that has an open end. By connecting the probes of two different calorimeters to a PMT, we can monitor the arrival times of the same laser pulse with an oscilloscope and actually measure the δ_i^{fiber}. In our setup the PMT is connected directly to the probe of the calorimeter 24. The other calorimeters' probe is reached using a 20 m long fiber, as shown in fig 5.15. The time difference between the two peaks observed in the oscilloscope represent the time the light needs to travel the 20 meters (that is always the same) plus the δ_{i24}^{fiber}.

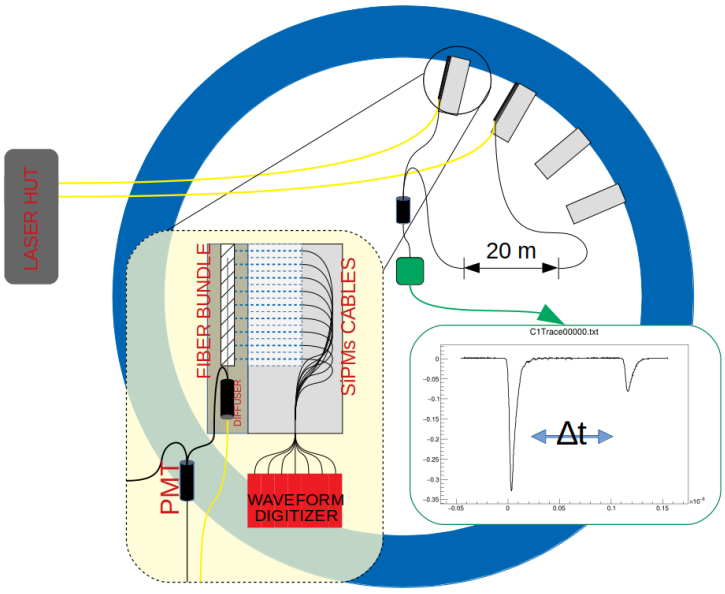

Figure 5.15: Schematic of the hardware measurement setup.

For each calorimeter we recorded 500 waveforms, and after fitting every peak with a parabola (Fig. 5.16), we obtain a distribution of the time difference between the peaks:

$$\Delta t_i = t_i^{peak2} - t_i^{peak1} = t_{20m} + \delta_{i24}^{fiber} \tag{5.17}$$

The distributions are then Gaussian fitted and shown in fig. 5.17. The peak number 24 represents the delay of the calorimeter 24 with itself, that is t_{20m}. To obtain the final δ_{i24}^{fiber} we must subtract this value from all the other peaks. Two additional peaks (number 25 and 26) are visible in the same spot as peak 24: they are repeated measurements of the same calorimeter 24 at different conditions. One is performed 2 hours after the first

measurement and the other with the 20 m fiber fully stretched. No systematic effects are observed.

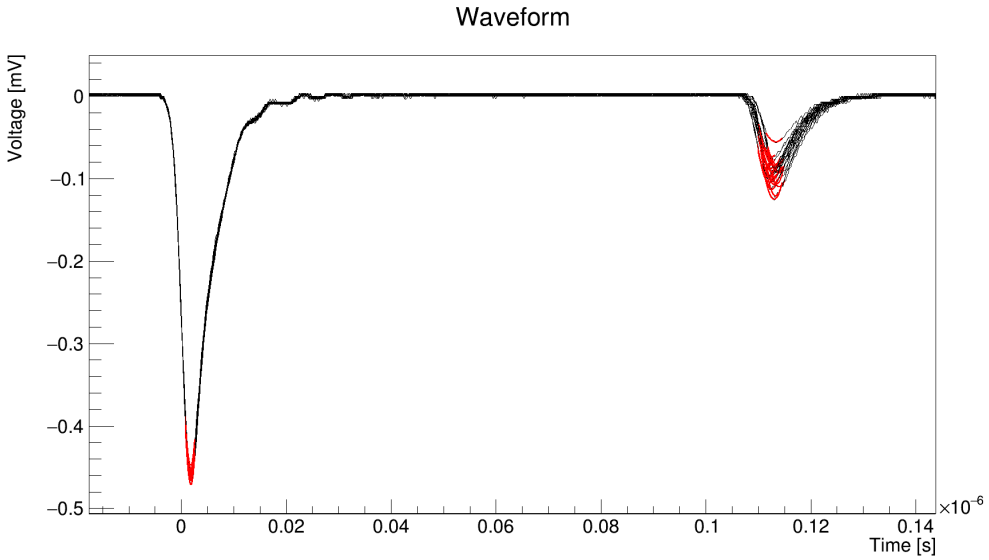

Figure 5.16: One waveform per calorimeter, as recorded by the oscilloscope. Parabolic fits are performed for both peaks, here shown in red.

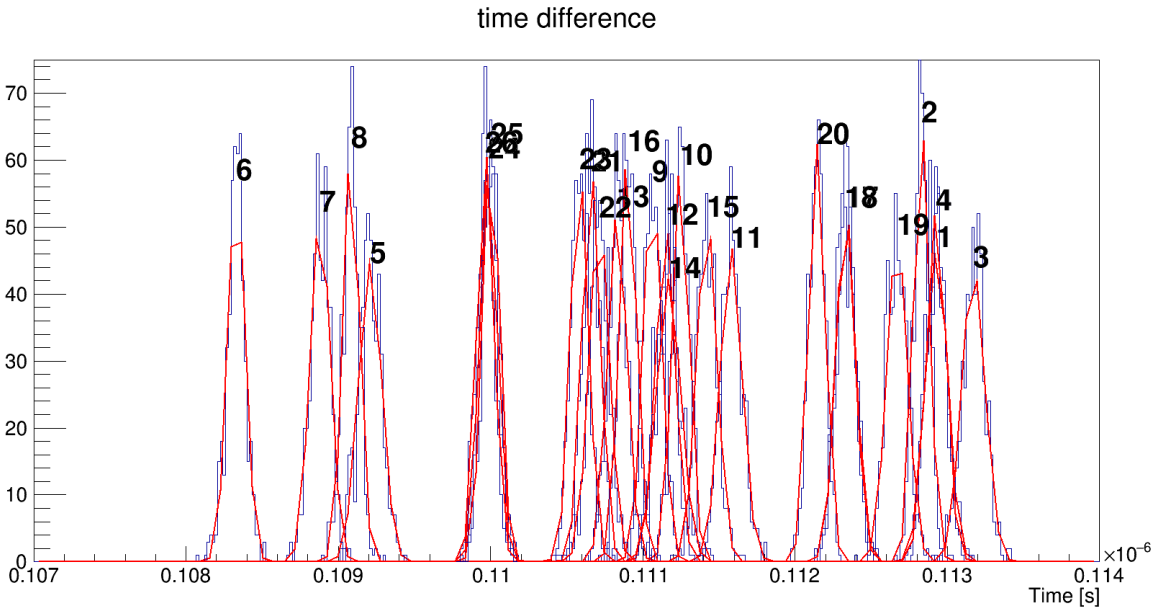

Figure 5.17: Time difference for each calorimeter. The distributions are gaussian fitted.

5.4.1 Amplitude dependence

One possible systematic error of this analysis comes from the amplitude of the PMT signal. A larger pulse could systematically shift the fitted time. To test whether this is relevant or not, we repeated the measurement of calorimeter 1 five times, changing the corresponding laser filter wheel value from 3 to 7. In figure 5.18 are shown all the different amplitudes as seen from the oscilloscope waveforms.

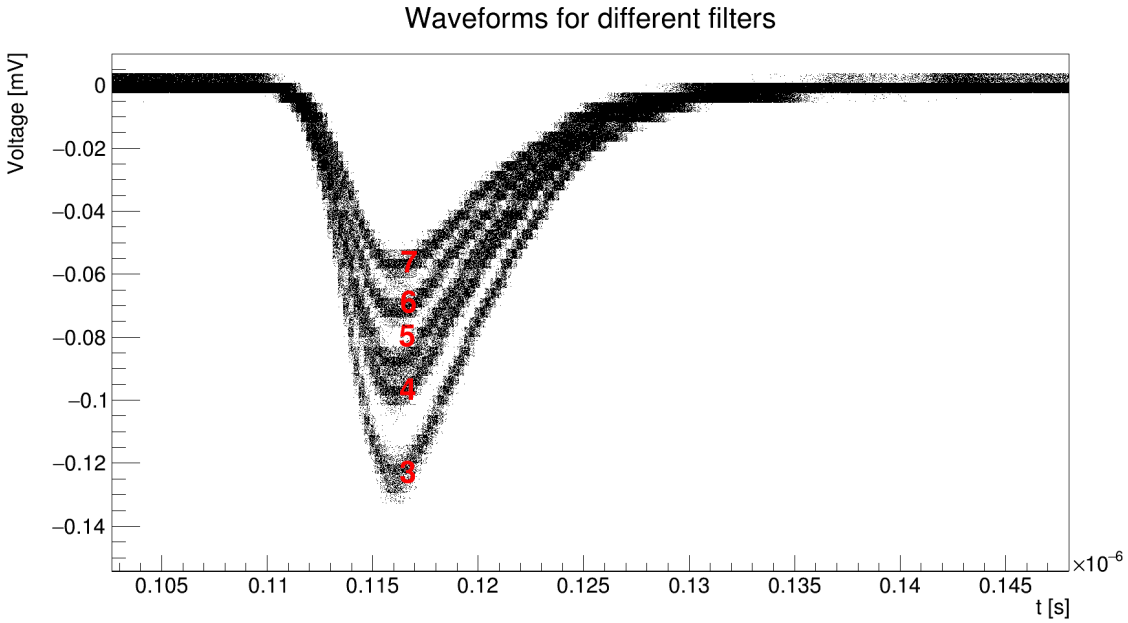

Figure 5.18: Waveforms for calorimeter 1 with different filter wheels.

Fitting with a Gaussian all the distributions as shown before, we find that there is no significant difference between the filters (Fig. 5.19). The only exception is the filter 7 (the shortest amplitude), that anyway shows a shift less than 100 ps with respect to filters 3-5.
Despite the fact that an amplitude correction is not needed for the precision we aim for, we decided to correct the amplitude of the pulse of each calorimeter acting on the filter wheels.

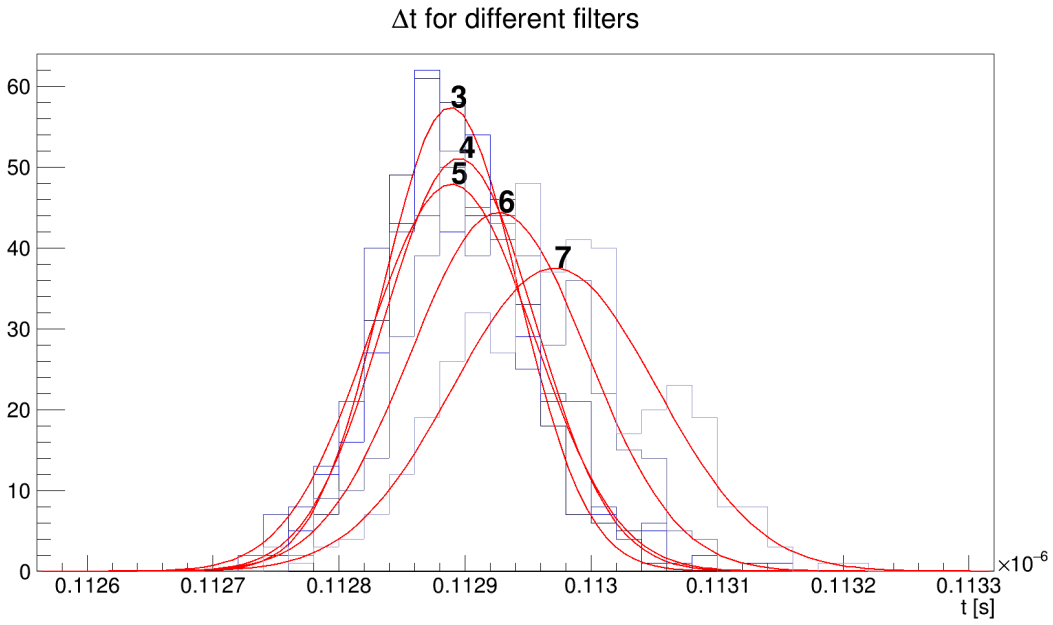

Figure 5.19: Results of the time difference between the second peak and the first peak, for different filter wheels.

5.4.2 Comparison with the analysis

The result of the hardware measurement is shown in Fig. 5.20. Comparing the measured δ_i with the lost muons analysis we see that the values are more or less comparable, except for lasers 1 and 2. We suspect that this discrepancy is due to some hardware modifications in the crate happened between the last physics run and this measurement (1 Aug 2018) which modified the trigger delay for the first two laser heads. However the trend within each subgroup is well represented, showing the consistency of the methods.

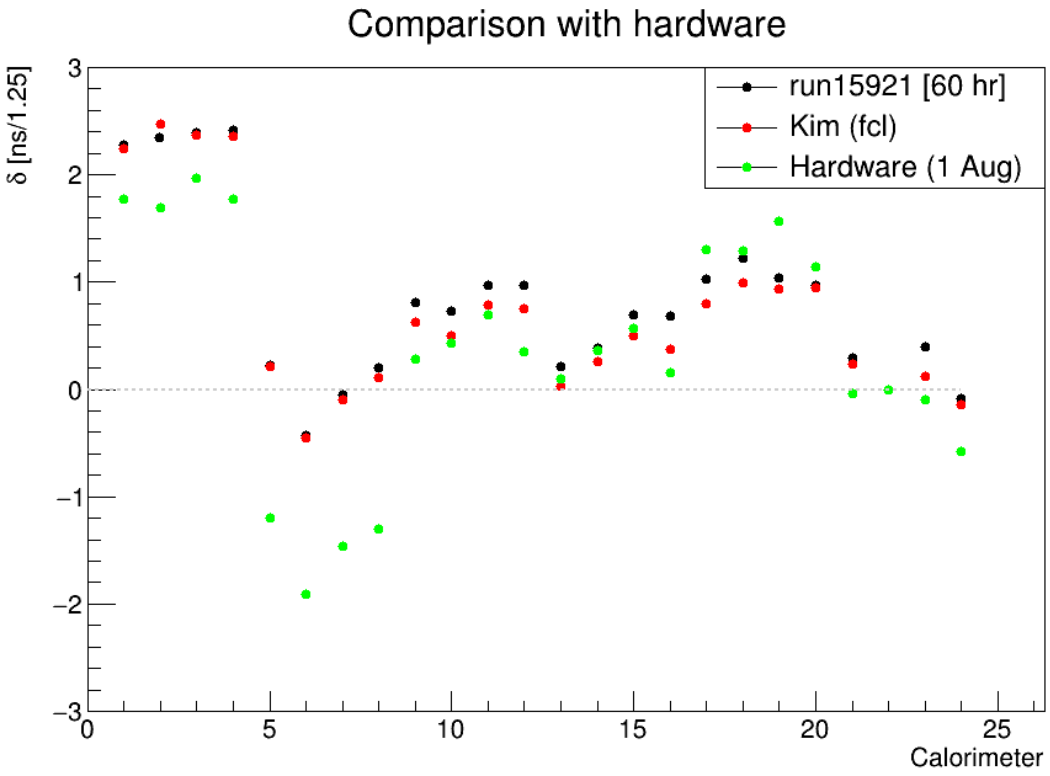

Figure 5.20: Results of the hardware measurement. Also plotted the lost muons analysis result (TOF method) in black and the reference in red.

Chapter 6

The Double Pulse System

The gain stability of the calorimeters is one of the requirements of the Muon g-2 experiment. The systematic uncertainty of the measurement of ω_a associated with the gain stability has to be lowered from 120 ppb to 20 ppb, as shown in Table 4.1 (Chapter 4). As discussed before, measuring the correct energy of the decay positrons is crucial because of the energy dependence of the decay asymmetry of the muon. Therefore, one of the requirements it the knowledge of the response of the SiPMs in every regime. In particular, when two positrons hit the same calorimeter in a time scale of few nanoseconds, the expectation is that the first pulse causes a systematic reduction in the measured energy of the second signal due to charge depletion in the capacitive components of the system's electronics [69]. With the Laser Calibration System we also want to study this phenomenon, by artificially sending two laser pulses with ns-level delay in dedicated runs and analyzing the SiPM response as a function of time separation and energy.

This chapter summarizes the work I did to make this correction possible, starting from the addition to the Laser System of a new operating mode, called *Double Pulse*, the data analysis of the dedicated laser runs, and its application to the positron data.

6.1 Construction

The six laser heads placed on the optical table of the Laser Calibration System are driven by an electronic module called Sepia-II. For the Double Pulse mode it is desirable to have the two pulses provided by two different laser heads instead of firing the same laser repeatedly, some of the reasons are:

- the laser maximum repetition rate of 10 MHz does not allow to test the nanosecond

time scale;

- in case of two consecutive pulses, the laser output light for the second one can be systematically lower than the first one, while light fluctuations for different lasers is uncorrelated;

- the laser light output fluctuates at the percent level from pulse to pulse; this fluctuation is monitored by two PIN diodes, which have a response time of the order of tens of microseconds. Therefore they cannot be used to correct close-by pulses.

For all these reasons, the laser optics has been modified to include the possibility of sending 2 different laser pulses to the same calorimeter. The solution comes by having an external electronic module that can trigger two different laser heads with high enough precision, and one of the two laser being deviated to follow the path of the other one. In standard data taking, each laser sends pulses to four calorimeters. The laser light is split by three *splitter cubes*, as shown in Fig. 6.2, and then directed by a mirror to 4 quartz fibers, also known as *launching fibers*. The light of one laser can be deflected from its normal path using motorized mirrors, so that they can be inserted only when necessary, and injected to the path of another laser light using its first splitting cube. The movable mirrors are mounted on motorized *flipflop stands Thorlab MFF101/M* (Fig. 6.1). The stand has 2 positions, at 90 degrees rotation one from the other, allowing for a beam stability better than 0.1 μrad.

A set of 12 fixed and 6 movable mirrors has been placed and aligned on the optical table. Thanks to these mirrors it is possible to deflect the laser light of all the 6 laser heads, pair by pair. This design allows the odd lasers (1^{st}, 3^{rd}, 5^{th}) to illuminate the same fibers that are usually lighted up by the even ones (2^{nd}, 4^{th}, 6^{th}) and vice-versa. A consequence of this setup is that only half of the calorimeters can be studied during each Double Pulse acquisition run.

6.1.1 Remote operation of the system

One motorized mirror is placed in front of each laser, just after its filter wheel. They are simple flip-flops: the mirror position is in either up-state or down-state. This movement allows the mirrors to be removed from the laser path when a Double Pulse is not desired, i.e. in normal acquisition mode. Each mirror is controlled by a switch pad with a button, but they can also be controlled with external TTL signals. Six USB-to-TTL (*TTL-232RG*) cables have been soldered as shown in Fig. 6.3. Each cable uses a serial

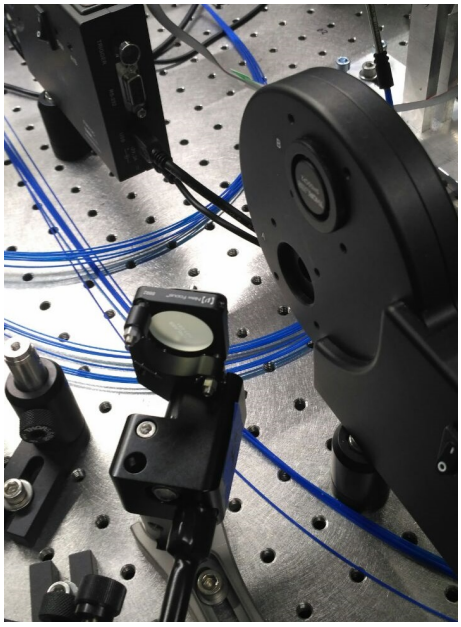

Figure 6.1: Motorized mount used to move the mirrors in and out from the light path. On the right, the motorized filter wheel.

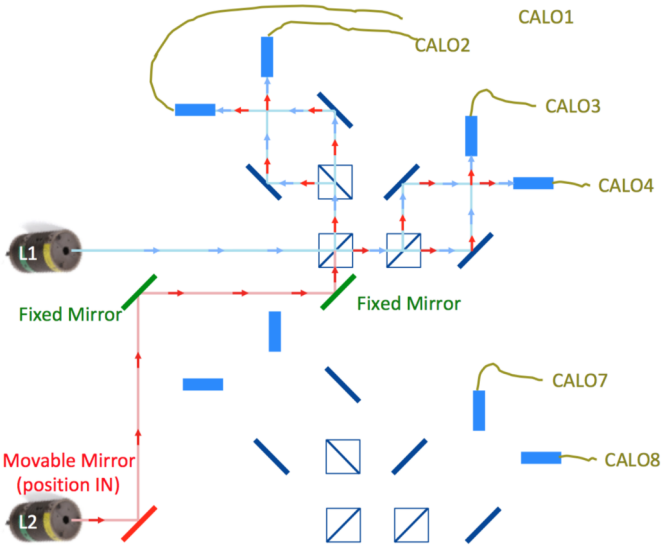

Figure 6.2: Double pulse laser setup. One set of lasers is reflected onto a different optical path with a movable mirror (red), and the reflected laser receives a trigger delayed with respect to the non-reflected laser trigger.

communication via its USB plug, and since it provides a voltage of 5 V, it is possible to generate a TTL signal using the Request-To-Send (RTS, green wire) bit. All the six cables are connected to an USB hub (Fig. 6.4), interfaced to a control computer in the Laser Hut.

Finally, a driver has been written in C++ to send the signals using the serial communication of the USB ports. This allows the remote control of the mirrors, provided a remote connection to the Laser computer. With this driver is possible to move each mirror individually or in groups: in the typical scenario of a Double Pulse acquisition run, the odd or even mirrors are moved simultaneously.

6.1.2 The delay generator

With the mirrors in place, the laser heads are triggered with a programmable delay. The electronic module used for this job is a Digital Delay Generator (DG) *SRS DG645*, a device that, provided an external trigger, is capable to generate a pattern of pulses with very precise delays, with an error of less than 100 ps.

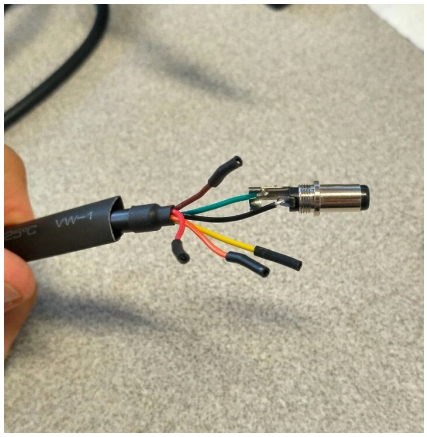

Figure 6.3: Open wires of one cable. The black and green wires are soldered to a 2.5mm co-axial plug.

Figure 6.4: The six USB-to-TTL cables are plugged into the same USB hub.

The trigger is given by the Laser Control Board (LCB) [70], at a rate of about 10 Hz, and the output is given by two separate channels. This device supports TCP/IP communication, so we connected it to the laser computer with an Ethernet cable. In particular, I coded a driver in C++ by which it is possible to reprogram the settings remotely, both with interactive commands and bash scripts. This is necessary to change the delays automatically for the Double Pulse acquisition runs, as it is desirable to scan over a range of delays. The ranges which are relevant for the calorimeter response are [0-100] ns, relative to the short-timescale gain recovery following a significant pulse, and [0-100] μs, relative to the gain response to a high sustained rate of light pulses [69].

Each output channel of the DG drives 3 lasers, the ODD lasers and the EVEN ones, respectively. To operate the laser both in the standard mode and in the double pulse mode, a logical FI/FO NIM module is used as an OR gate having, as input, the DG and the LCB signals. This allows to operate the laser without passing through the Delay Generator. The outputs finally reach the device that actually fires the lasers: the controller *PicoQuant* PDL 828 "Sepia II". The full diagram is shown in Fig. 6.5.

An additional feature of the DG, which turns out to be very useful in signal normalization, is the *prescale* option: each DG output can be independently prescaled by a factor $N = 1 - 10000$, such that only 1 signal every N triggers is actually issued. This feature is used to prescale the *prompt* signal. If P is the prompt signal and T is the delayed (or *test*) signal, then by using the prescale it is possible to build the following

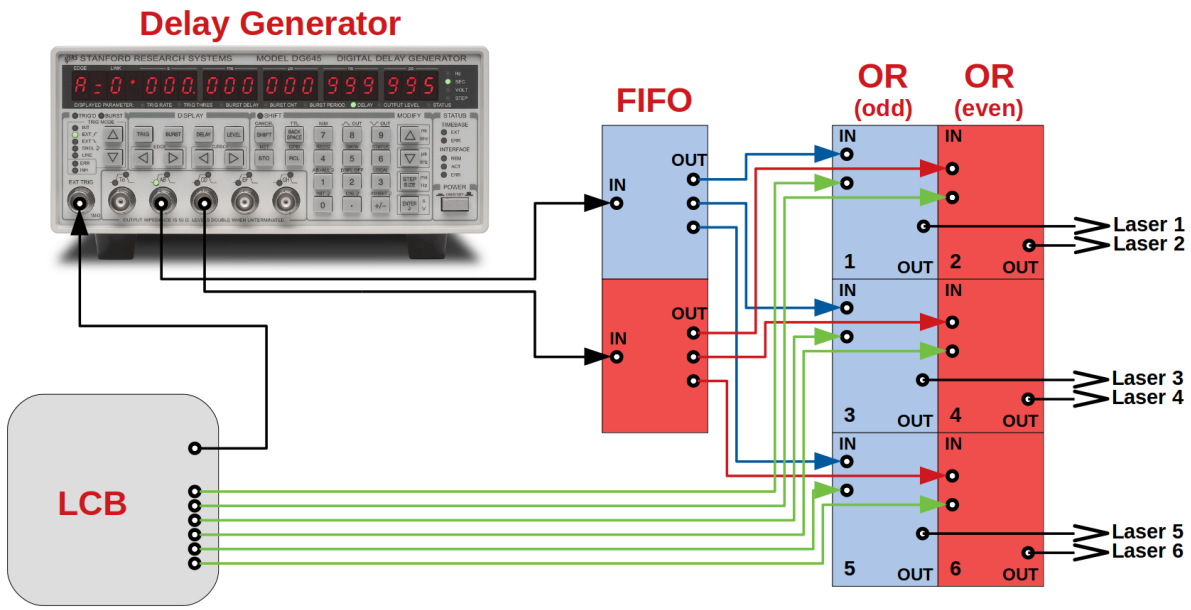

Figure 6.5: Schematic of the NIM logic used to trigger the lasers both with the LCB and the Delay Generator.

sequence of pulses:

$$P + T; T; P + T; T; ... \tag{6.1}$$

This sequence allows to use the T-only signals as normalization. The whole system is controlled by the data acquisition (DAQ) software, that supplies the triggers and records the data coming from the calorimeters. The trigger structure for Double Pulse runs is represented in Fig. 6.6. In addition, using a feature of the DG called *burst mode*, it is possible to increase the collected statistics for the short-term study by firing four (or more) Double Pulse events for every fill. The same option is used to fire a burst of many impulses for the long-term study.

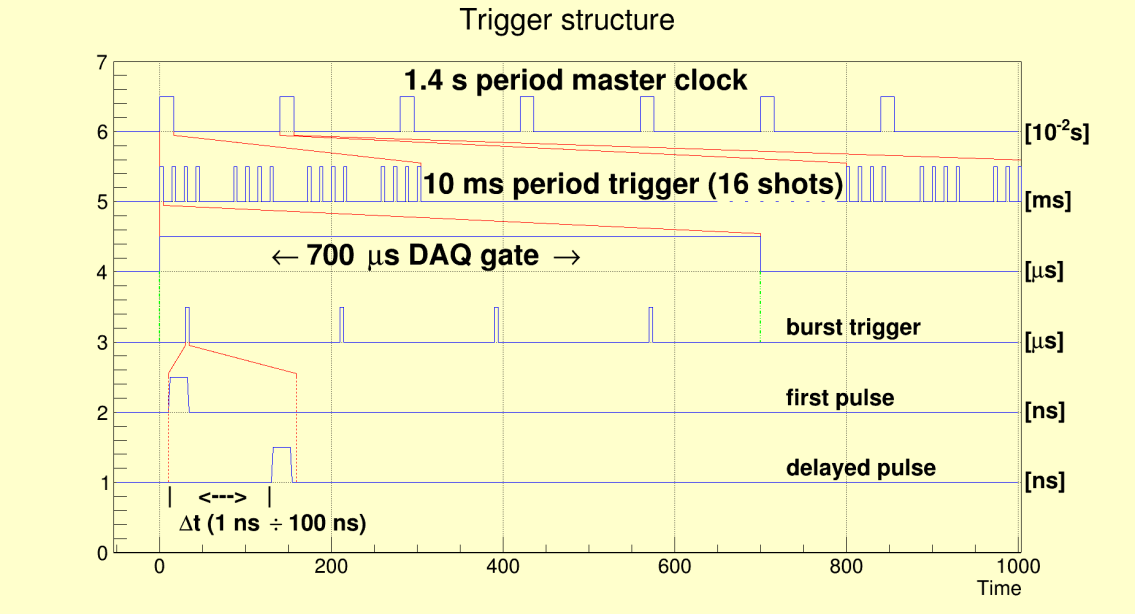

Figure 6.6: Trigger structure of the Double Pulse mode. The bottom two lines are the first and the second (delayed) pulses.

6.2 Short Time Double Pulse

With the Short Time Double Pulse (STDP) analysis, we want to study the response of the silicon photomultipliers (SiPM), to two signals hitting the same channel few nanoseconds apart. The SiPM response depends on the Front End Electronics, as described in detail in [69]. Briefly, when a SiPM fires, it delivers charge, which is replenished afterwards. The delivered charge comes from all available sources, particularly the SiPM array itself. The SiPM array behaves as a charged capacitor; i.e., the bias voltage experienced by the SiPM array drops momentarily before the charge is recovered. As an example, suppose that 1600 pixels fired simultaneously on the SiPM board, 100 pixels ineach of the 16 channels. The charge delivered by a fired pixel is $1.5 \cdot 10^6$ electrons, for a total charge for each channel of 24 pC. This results in a voltage drop of 96 mV, taking into account the 250 pF capacitance of each of the 16 channels [69]. The relative voltage drop is 4% compared to the typical operating over voltage bias of 2.5 V. The charge is replenished from the capacitors on the SiPM board. The only available path for the charge to the SiPM pixel goes through its quenching resistors. The product of the pixel capacitance, 55.8 fF, and the value of the quenching resistor, 100 kΩ, sets the expected timing constant for the charge recovery of about ∼6 ns.

The Short-Time gain study can be performed by inserting the movable mirrors and by operating the Delay Generator as described in the previous section. The delays that separate the two pulses range from 0 ns up to 80 ns. One double pulse event is shown in Fig. 6.7.

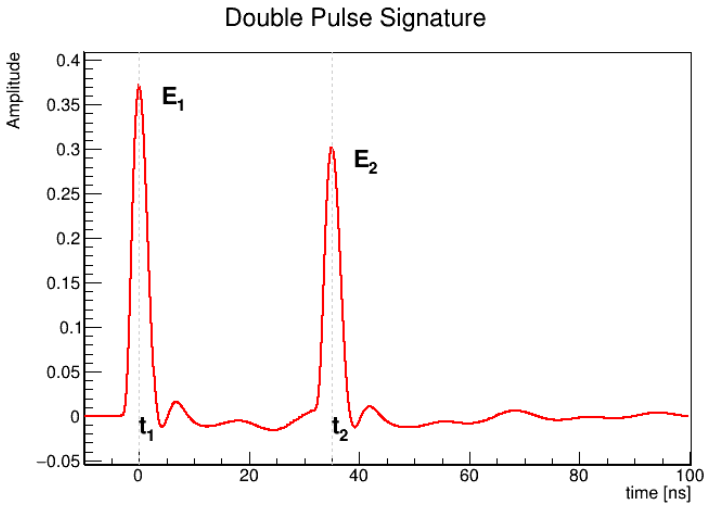

Figure 6.7: Example of a double pulse signal shape.

6.3 Reconstruction software

The STDP data is analyzed using the g-2 software, developed within the *art* framework [71, 72]. The analysis procedure is divided in three steps:

- Step 1 - **Pulse reconstruction**. In this step the raw data acquired during the dedicated STDP runs is processed. Each individual signal recorded by a SiPM is fitted with a template fit. The templates used for the pulse fit are collected using dedicated runs. In particular, they are characterized for each crystal and for each *type* of signal: positrons and laser hits have different templates. In addition, the light from two laser heads hit the same SiPM during a STDP run: the first is called *standard* and the second *crossed*, since it is reflected from its normal path using the extra mirrors as described in section 6.1. The standard and crossed templates are very similar (Fig. 6.8a), but a closer look to the difference (Fig. 6.8b) shows a % change, a variation that has to be accounted for in these precision studies [73]. The reconstruction module detects if two signals are close in time ($\Delta t < 100$ ns) and

then applies a particular *multi-fit* with the respective templates added together, as defined in Eq. 6.2.

$$f_{STDP}(b, a_1, t_1, a_2, t_2) = b + a_1 \cdot f_{std}(t_1) + a_2 \cdot f_{cross}(t_2) \tag{6.2}$$

where f_{std} and f_{cross} are the standard and crossed templates for that particular SiPM. a_1 (a_2) and t_1 (t_2) represent the amplitude and time of the first (second) peak, while b is the baseline. Each fit gives, among other information like χ^2, the two main variables that we want to extract: energy and time.

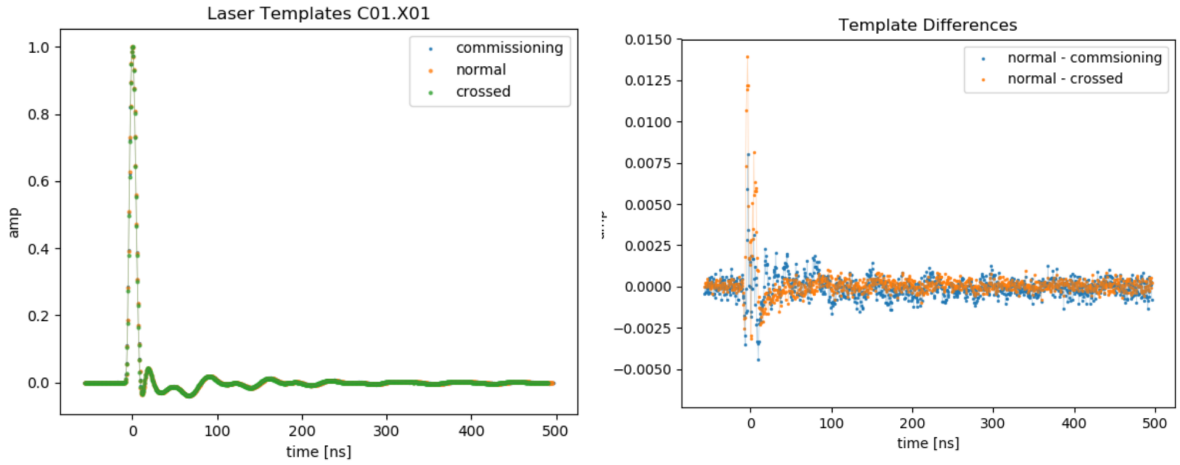

(a) (b)

Figure 6.8: (a) *Standard* and *crossed* laser templates for one SiPM (Calo01, Xtal01). The commissioning template (blue) represents a standard template taken 4 months earlier. (b) Difference between the new standard templates and the other templates. Percent level changes are visible in the difference which cause percent level changes in the extracted amplitude (energy).

- Step 2 - **Dataset creation**. After the reconstruction of each pulse from the raw data, the second step puts together the information extracted to form a STDP analyzable data set. Thus, this step extracts the double pulse information from the *art* data and builds a reduced ROOT-tuple. Recalling Eq. 6.1, if there is more than one Test pulse for each Double pulse, the average energy of the n available test pulses is taken. The overall sequence is represented in table 6.1. Usually our STDP acquisition runs have $b = 4$ burst pulses and $n = 2$ test pulse fills.

Fill number	Burst number 1	2	⋯	b
0	$(DP)_1$	$(DP)_2$	⋯	$(DP)_b$
1	T_1^1	T_2^1	⋯	T_b^1
2	T_1^2	T_2^2	⋯	T_b^2
⋮	⋮	⋮		⋮
n	T_1^n	T_2^n	⋯	T_b^n

Table 6.1: Schematic view of the STDP data structure. For each fill there are b repetitions both for Double Pulse and for Test pulses. If $n > 1$, the normalization energy is taken as the average $E_{norm} = \frac{1}{n}\sum_{i=1}^{n} T^i$.

- Step 3 - **Gain analysis**. For each SiPM, the gain is analyzed by plotting the ratio E_2/E_{norm} versus the measured delay $\Delta t = t_2 - t_1$. For each time delay set with the Delay Generator there are few thousands double pulse events. The ratio can be determined either by the average of the ratio $\left\langle \frac{E_2}{E_{norm}} \right\rangle$ or the ratio of the averages $\frac{\langle E_2 \rangle}{\langle E_{norm} \rangle}$. The latter is preferred since systematic variations in the energy of the test pulses (due to temperature, for example) are not expected in the time scale of a STDP run (few minutes for each delay). For each delay we expect the distribution of E_2 and E_{norm} to be Gaussian, so that the average corresponds to the peak value. Otherwise, if the distribution is skewed, a bias could be introduced by taking the bare average. A check on the distributions shows that they are indeed Gaussian (Fig. 6.9), so that the usage of the ROOT `TProfile` object is adequate for this task.

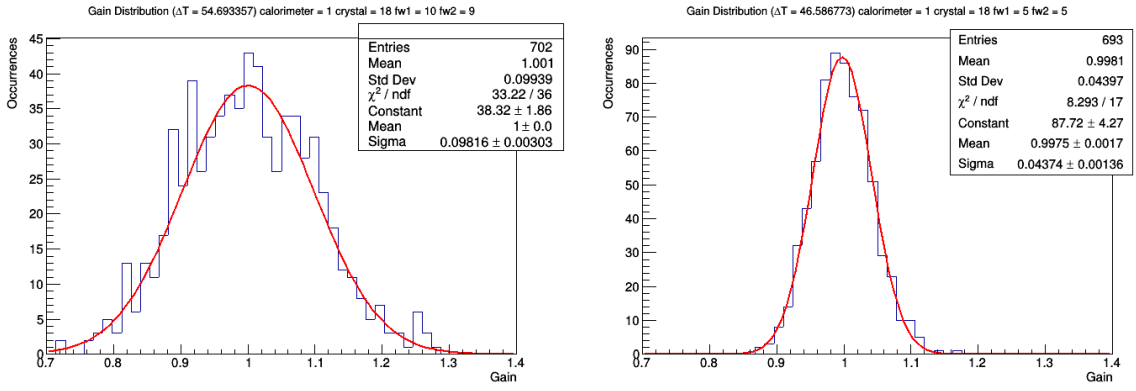

Figure 6.9: Distributions of E_2/E_{norm} for two different SiPMs, Δt and Filter Wheels. The average value is always compatible with the fitted Gaussian mean.

6.3.1 Preliminary results

During the spring of 2018, before the first beam run of the E989 experiment, a data set of STDP runs was taken with only one Filter Wheel combination. More details on the use of Filter Wheels for this STDP study will be given in section 6.5. For this preliminary data taking, no test pulse was injected, so the gain shape is evaluated only using the energy of the second pulse. In Fig. 6.10 the profiles for the energies of the two pulses are shown as a function of Δt. The energy of the first pulse remains constant as expected, while the energy of the second pulse shows an exponential drop at low Δt. Note that the measured points oscillate around the exponential function: this effect is not physical and will be resolved in later analyses. The function used to fit the graph is an exponential with three free parameters:

$$E_2 = E_{inf} \cdot \left(1 - a \cdot e^{-\frac{\Delta t}{\tau}}\right) \tag{6.3}$$

a represents the extrapolated intercept at $\Delta t = 0$, while τ is the recovery constant. Since the energy is not normalized here, E_{inf} is the fitted asymptote at $\Delta t \to \infty$. A study on all the 1296 SiPMs shows that the two gain parameters are on average $a \approx 0.1$ and $\tau \approx 15$ ns.

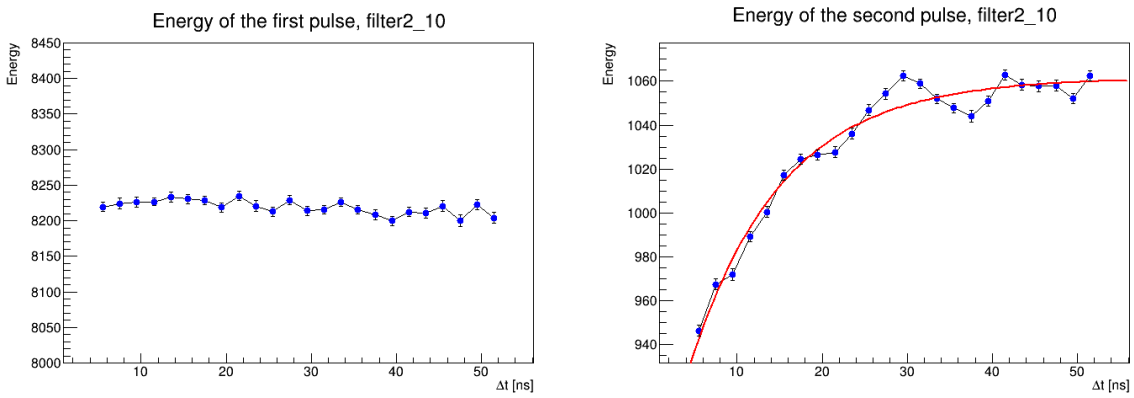

Figure 6.10: Profiles of the energy of the first pulse (left) and second pulse (right) as a function of the time separation, for one SiPM.

6.4 STDP correction in the ω_a analysis

As discussed before, the systematic error budget on the measurement of the anomalous precession frequency ω_a is 70 ppb. In particular, each contribution and correction to

the data has to be evaluated by terms of how much the correction influences the ω_a measurement. The STDP gain correction has to be applied to the positron data, since the gain recovery of the SiPM is an expected and now observed phenomenon. Its effect is nonetheless expected to be small, since the gain correction is at the percent level and the probability of two positrons hitting the same SiPM in a 100 ns window is again at the percent level.

The correction has been tested on a data set called *60h dataset*, acquired in the days from 22nd to 25th April 2018, for a total of $\sim 10^9$ positrons with $E > 1.8$ GeV. In this first study a unique correction is applied to hits which are closer in time than 80 ns:

$$G(\Delta t) = 1 - 0.1 \cdot e^{-\frac{\Delta t}{15.0}} \tag{6.4}$$

The energy of the second cluster is thus modified as follows:

$$E_2' = E_2 - E_2^{over} \cdot \left(1 - \frac{1}{G(t_2 - t_1)}\right) \tag{6.5}$$

where E_2^{over} is the energy deposited by the second particle to the SiPMs shared by both clusters. Note that, since $G < 1$, the correction is always positive, so that $E_2' \geq E_2$. This correction is applied in chronological order, so that if three particles produce signals in the defined time separation window, the second particle is corrected first and the third particle is corrected last.

6.4.1 Fitting the wiggle plot

First of all, we want to determine how much the STDP correction affects the measurement of the ω_a value. The analysis is based on the techniques described in section 3.4.2. Figure 6.11 shows the *wiggle plot* with and without the STDP correction. Here, the histograms are filled using the T-Method with an energy threshold of 1.7 GeV. The fit performed has nine parameters: the standard five parameters (N_0, τ, A, ω_a, ϕ) and the four CBO parameters, and the fit range is $[40, 400]$ μs. The fit procedure is blinded, so that instead of ω_a the value R is shown. The difference in the value of R is $\sim$40 ppb. Increasing the fit range to $[32, 400]$ μs (Fig. 6.12), we see that ΔR is $\sim$200 ppb. This is expected, since the muon decay rate increases exponentially going backward in time, and so the probability of double pulses.

The aim of this analysis is only to have a preliminary idea of the impact of the STDP

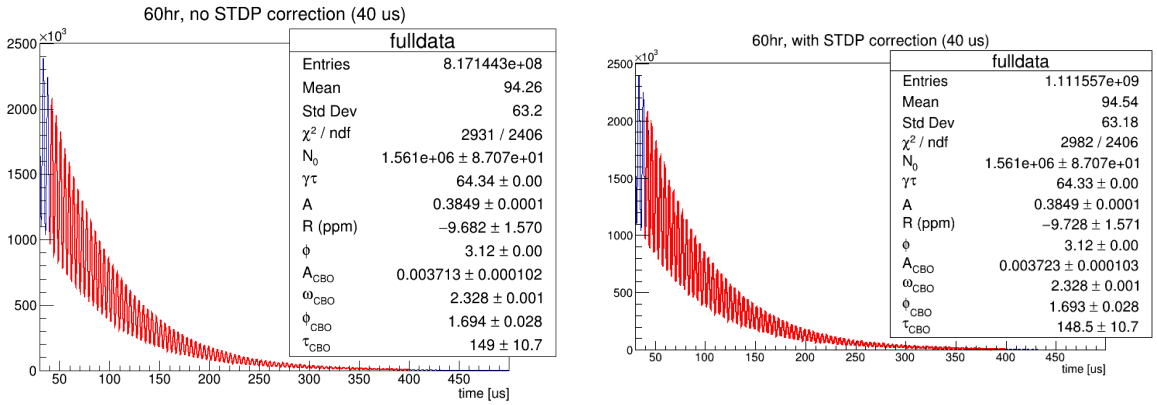

Figure 6.11: Wiggle plot before (left) and after (right) the STDP correction. The fit is performed using the 9-Parameter function in the range $[40, 400]$ μs.

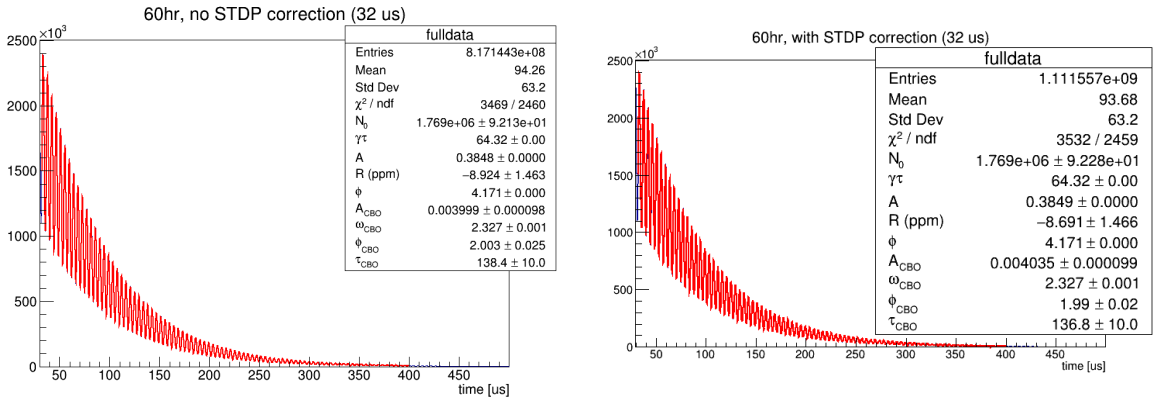

Figure 6.12: Wiggle plot before (left) and after (right) the STDP correction. The fit is performed using the 9-Parameter function in the range $[32, 400]$ μs.

correction on positron data as a first-order approximation. The important conclusion is that the STDP correction affects the ω_a measurement at the level of $\mathcal{O}(100)$ ppb, in particular when the fit is performed from early ($<$40 μs) times.

6.4.2 Double Pulse events in beam data

We expect the distribution of double pulse events to be uniform, since the events are independent and the time gap is much smaller than the muon decay time $\gamma\tau = 64.4$ μs. Figure 6.13 shows a flat distribution, as expected, but with an initial transition that starts from 3.75 ns and reaches the plateau at 6.25 ns. These two values correspond to 3 and 5 clock ticks respectively, and this slope can be explained by an inefficiency of the

reconstruction software ability to distinguish two pulses that are very close. Such events are considered *pileup*.

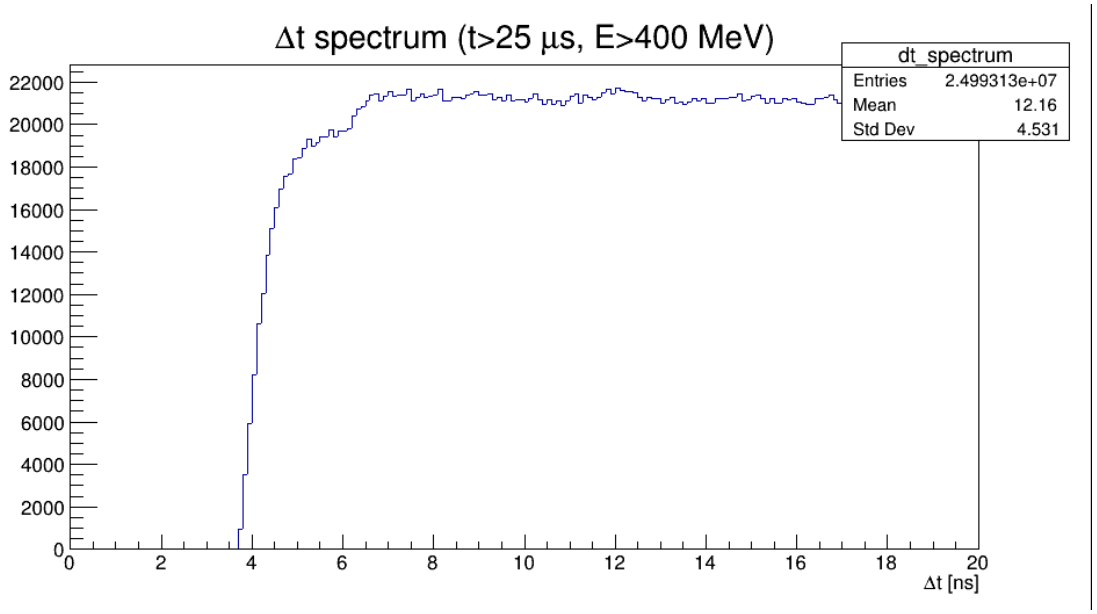

Figure 6.13: Distribution of the time separation of positrons that fall in the STDP condition. A time cut of $t > 25$ μs and an energy cut of $E > 400$ MeV have been applied to remove Lost Muons events.

The fraction of STDP events over the time of a fill is shown in Fig. 6.14 together with the wiggle plot of Fig. 6.11, in logarithmic scale. The blue graph is the distribution of the positrons with energy greater than 1.7 GeV, and its slope represents the exponential decay of the muons, with lifetime $\tau = \gamma\tau_\mu \approx 64$ μs. The black graph is the distribution of the positrons that are affected by the STDP correction, again with the $E > 1.7$ GeV cut applied. We expect that the distribution of STDP events decays with half the lifetime of the muon. In fact, the probability of having two muon decays in a time window $t + \delta t$ is

$$p(t+\delta t)^2 \xrightarrow{\delta t \to 0} \left(e^{-\frac{t}{\tau}}\right)^2 = e^{-\frac{t}{\tau/2}} \tag{6.6}$$

A 5-Parameter fit shows an exponential decay with a lifetime of $\tau_{STDP} \approx 32$ μs.
Figure 6.15 shows the ratio between these two distributions. We can see then that the fraction of positrons affected by STDP is around 3% at the beginning of the fill and decays to $\approx 0.1\%$ after 250 μs. This correction has more effect at early times, as already demonstrated in Fig. 6.12.

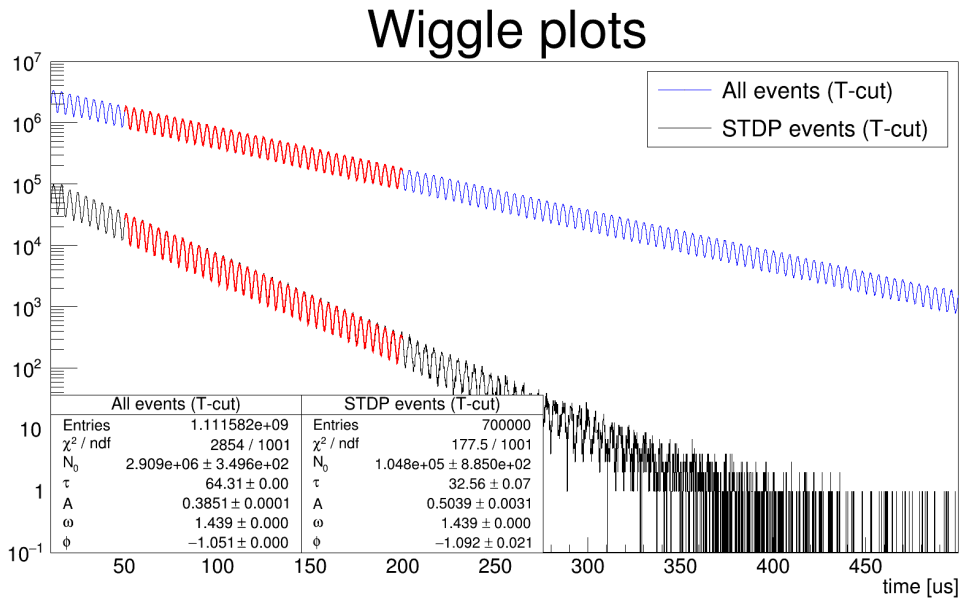

Figure 6.14: Distribution of positrons (blue) and STDP (black) events in the fill time scale (700 μs). A TMethod-like energy cut of 1.7 GeV has been applied. Both distributions have been fitted with a 5-Parameter function in a small time range.

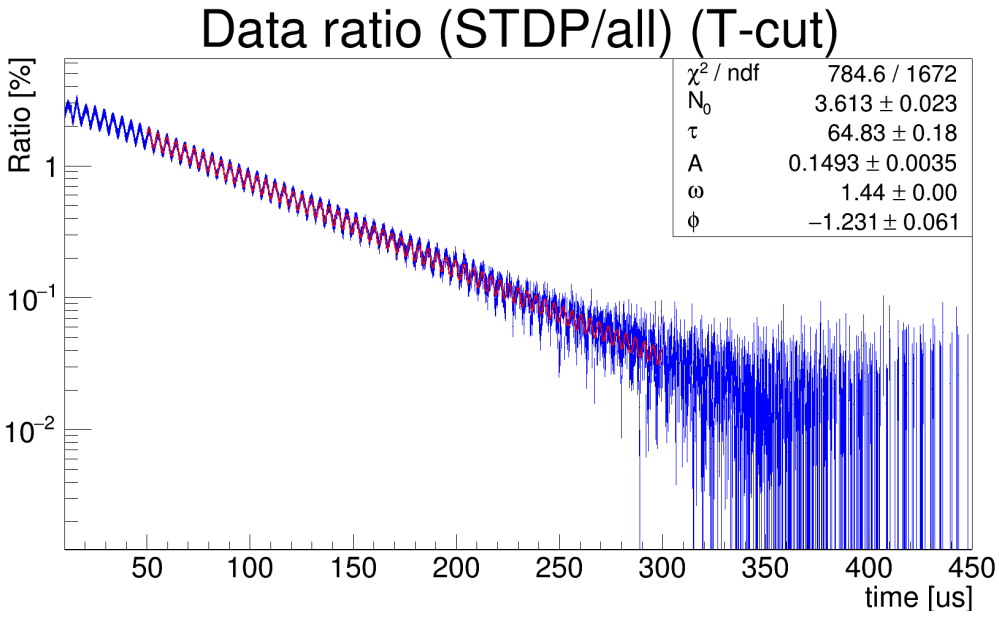

Figure 6.15: Ratio of the two distributions of Fig. 6.14. The STDP events correspond to ∼3% of all data at early times, decaying to less than 0.1% after 250 μs.

Muons that have a momentum that is too far from the "magic" one of 3.094 GeV/c are scraped out of the storage region. They then curl inward and hit one or more calorimeters, producing signals characteristic of minimum ionizing particles (MIP). In fact, they deposit on average ∼170 MeV of energy in one crystal, and when they hit two or more consecutive calorimeters they can be tagged using a coincidence time window corresponding to the Time Of Flight (∼6 ns). Figure 6.16 shows the energy spectrum of STDP events between 0 and 1 GeV. Several peaks are visible: the first one is the 170 MeV signal, and the others are pileup events of 2 or more muons in the same crystal. The blue curve is the spectrum before the correction, while the orange curve is after the application of STDP. A Gaussian fit on the first peak shows a 5 MeV shift to the right.

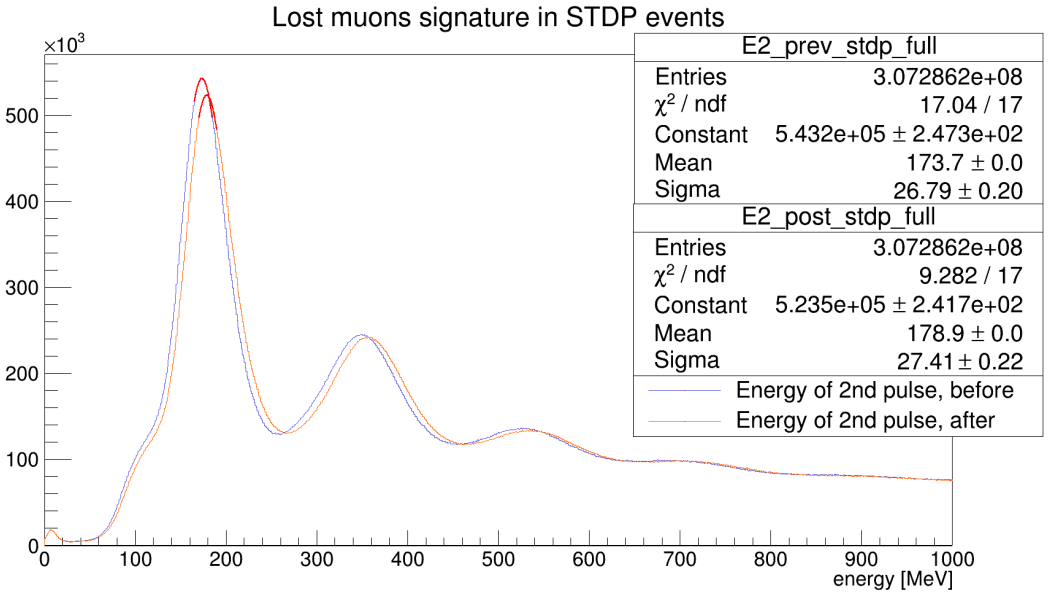

Figure 6.16: Energy spectrum of the detected particles in the 0-1 GeV range. The several peaks correspond to single and multiple (pileup) lost muons events. The application of the STDP correction shows a 5 MeV shift to the right of the first peak.

6.5 Study on energy dependence

As discussed in section 6.2, the STDP gain effect is related to the recovery time of the individual pixels of the silicon photomultipliers. While the time constant τ depends on the electronics, the gain drop a is expected to depend on the energy of the first pulse. In fact, as the energy is higher, more pixels are fired and have to recover. When the second

pulse arrives, it will "see" a reduced amount of available pixels, this effect being higher if the first pulse was very energetic.

The energy dependence of STDP is investigated with a simple toy Monte Carlo simulation (section 6.5.1), and has been studied with great depth with dedicated STDP laser runs (section 6.5.2). In the first case, it is sufficient to simulate different numbers of photons that hit the SiPM for the first pulse. In the laser STDP runs, different amount of energies are studied thanks to the use of Filter Wheels.

6.5.1 Toy Monte Carlo simulation

To predict and interpret the behavior of the gain shape with different energies for the two pulses, I developed a small Monte Carlo simulation. Here a SiPM with 57600 Geiger-like pixels is simulated, with a recovery time for every pixel set at 12 clock ticks (15 ns). Two particles are then simulated with various arrival times, with the second one delayed from -20 to 60 c.t. with respect to the first one. A particle is simulated as a number of photons hitting the pixels in a instantaneous time window, uniformly distributed over the surface of the SiPM. The signal of real positrons develops in few nanoseconds, so this simulation has some limits for small Δt.

Different particle energies are simulated using different number of photons. Figure 6.17 shows three gain shapes, with the energy of the first pulse going from 1000 to 3000 photons and the energy of the second pulse fixed at 1000 photons. Here the gain is defined as the ratio between the number of photons observed and the number of photons simulated, for the second pulse. The gain curve is fitted with the exponential function $G(\Delta t) = N(1 - ae^{-\Delta t/\tau})$. We observe that different energies for the first pulse only vary the gain drop amplitude a (Fig. 6.17). The recovery time constant is measured to be 12 c.t. as expected. The asymptote doesn't reach 1, so for 1000 photons there's a non-linear response, with a 1% difference with respect to the linear case. This is coherent to what is expected as seen in Eq. 3.1. Figure 6.18 shows again three gain shapes, but now varying the energy of the second pulse, from 500 to 1500 photons. The exponential fits show that the a and τ parameters remain constant, while the only difference is caused by the non-linearity of the detector. We observe a 0.5% difference at 500γ, and a 1.3% difference at 1500γ.

With this simulation we can conclude that the parameter a is expected to depend on the energy of the first pulse ($E1$) but not on the second pulse. On the other hand,

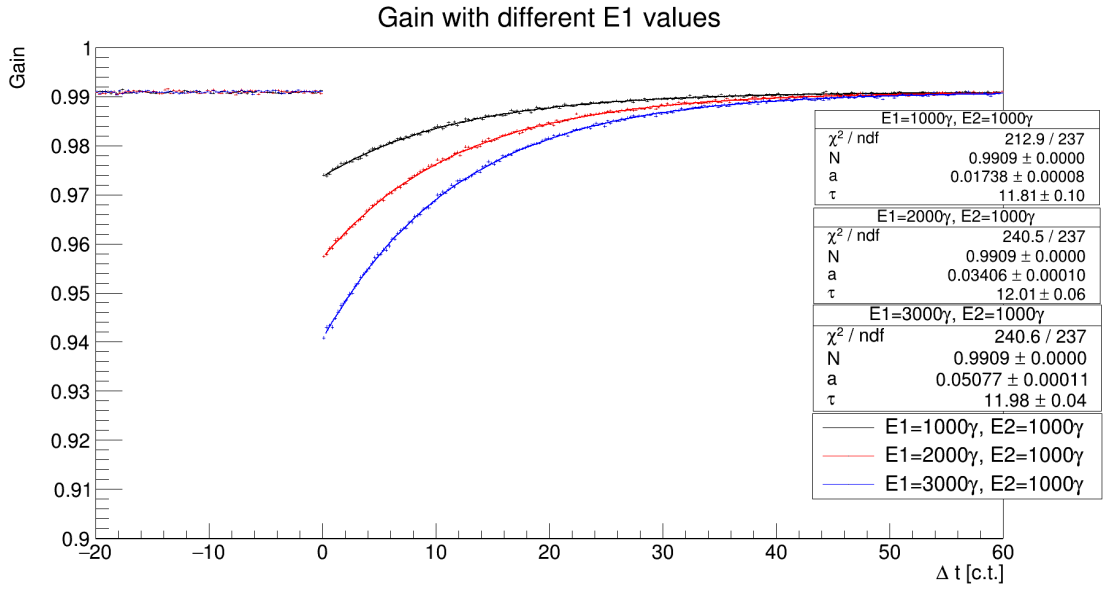

Figure 6.17: Simulated gain shape with different energy values for the first pulse (1000, 2000 and 3000 photons). The energy of the second pulse is fixed at 1000 photons.

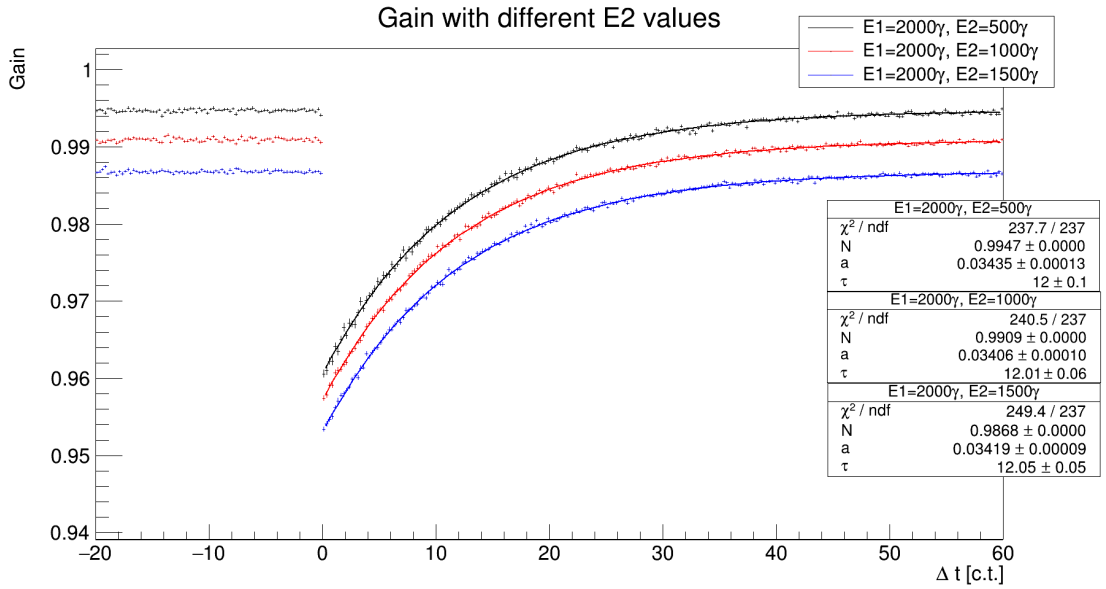

Figure 6.18: Simulated gain shape with different energy values for the second pulse (500, 1000 and 1500 photons). The energy of the first pulse is fixed at 2000 photons.

the parameter τ is expected to be independent on energy. To further investigate the parameter $a(E1)$, a scan from 0 to 4000 photons for the first pulse has been simulated, with a step of 200 photons. Figure 6.19 shows the values of a, with a linear fit on top. The dependence is linear, with an intercept compatible with 0 and a slope of 0.00168 $\%/\gamma$. The photon-to-energy conversion is approximately 1 detected photon per MeV [74], so that the observed slope here is $\approx$2 %/GeV.

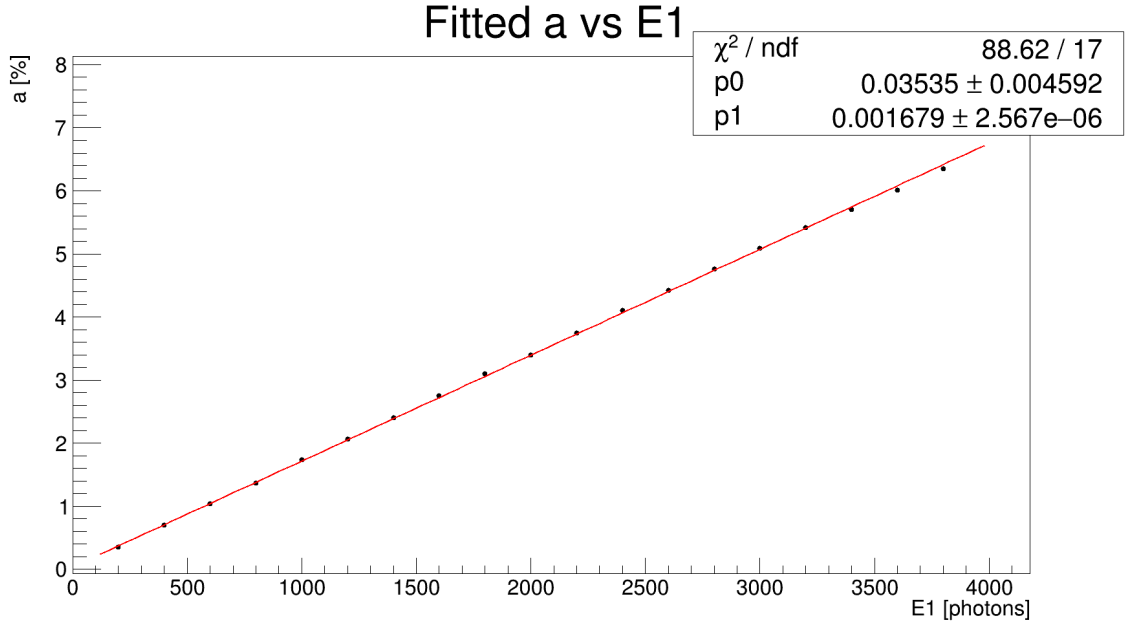

Figure 6.19: Values of a as a function of simulated photons for the first pulse. The points are fitted with a linear function. $p0$ is the intercept and $p1$ is the slope.

6.5.2 Analysis of the STDP laser runs

The study on the energy dependence of the STDP gain shape has been performed analyzing dedicated laser runs. In particular, the energies of the two pulses can be modified thanks to the presence of the Filter Wheels on the optical table. Since the two pulses are generated from two different laser heads, the two Filter Wheels allow independent choice on the two energies.

Several analyses and optimizations of the procedure has been performed in the months from October 2018 to February 2019. This section will describe only the latest and official analysis, ignoring the hardware and software problems that had to be overcome.

The final data set of STDP laser runs was acquired varying the delay between the pulses from 0 to 60 clock ticks, at 2 c.t. steps. For each delay, few thousand laser event are triggered over a time period of 5 minutes. The whole sequence has been repeated for 18 combinations of the Filter Wheels. Calling FW_1 the Filter Wheel of the first pulse and FW_2 the one of the second pulse, the combinations used six values for FW_1 (from 5 to 10) and three for FW_2 (5, 7, 9). These numbers label the filters inside the Filter Wheels, with higher numbers corresponding to higher Optical Density, and therefore to lower transmittivity. Table 6.2 relates each number with its transmittance factor. This whole acquisition is repeated two times, for the calorimeters illuminated by the *odd* and *even* lasers respectively. This is needed since the double pulse system redirects half of the lasers on top of the other half. At the end, the STDP data set is composed of $30 \cdot 18 \cdot 2 = 1080$ runs that have to be reconstructed first and then analyzed.

Filter number	1	2	3	4	**5**	**6**	**7**	**8**	**9**	**10**	11
Nominal transmittance [%]	100	79	65	50	**47**	**36**	**26**	**21**	**17**	**13**	5

Table 6.2: Transmittance values for each filter number. The highlighted values correspond to the ones used for this STDP analysis.

The goal of this analysis is to find the energy dependence of the parameters a and τ of the gain shape defined as:

$$G(\Delta t; i, E1, E2) = 1 - a(i, E1, E2) \cdot e^{-\frac{\Delta t}{\tau(i,E1,E2)}} \tag{6.7}$$

where i represents the SiPM number. In addition, another functional form that describe a smooth return to $G = 1$ at $\Delta t = 0$ is named *Lognormal* and defined as:

$$G(\Delta t) = 1 - a \cdot e^{\frac{1}{2}\left[\log^2(\Delta t/\tau)\right]/\left[\log^2(t_M/\tau)\right]} \tag{6.8}$$

where t_M and a are the position and the amplitude of the minimum, while τ is the recovery time. An example of the two fits is shown in Fig. 6.20 for one SiPM. The two functions mostly overlap for $\Delta t > 10$ c.t.. For this Double Pulse analysis only the exponential function will be considered. In the final reconstruction of the positron data, an artificial dead time of 2-4 ns (corresponding to the first point of Fig. 6.20) is set as a lower limit on the time separation between two signals. Thus, the two gain shapes are effectively equivalent.
For each SiPM the ratio between the energy of the second pulse and the normalization energy is computed for each delay, and fitted with the function of Eq. 6.7. This is

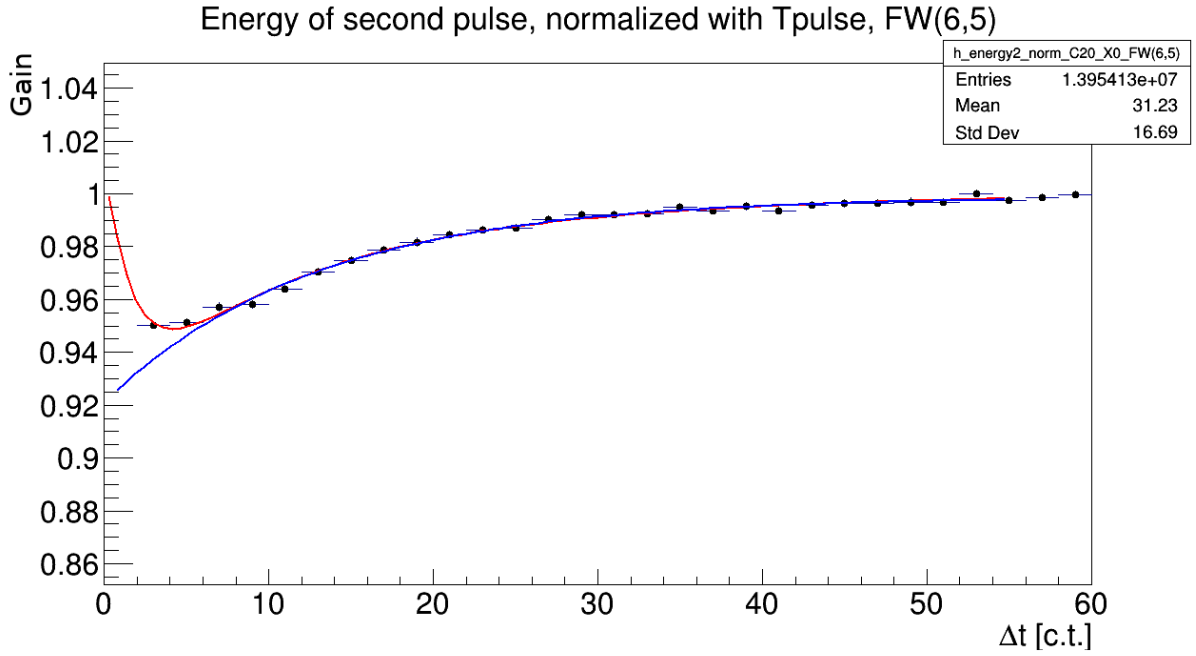

Figure 6.20: Gain recovery of one SiPM. The blue curve is the exponential function, while the red curve is the Lognormal function.

repeated for every combination of FWs. As a first qualitative study, the values of a and τ are averaged for each SiPM and plotted as a function of the two FWs (Fig. 6.21). Any dependence of the parameters on the energies would here be visible as a global shift. The values of τ are constant and don't shown any visible dependence on any of the two Filter Wheels. On the other hand, the values of a show a very clear "staircase" shape. They are constant with respect to FW_2, while they decrease in a linear fashion with respect to increasing values of FW_1. This qualitative behavior confirms what has been found with the Monte Carlo simulation of Sec. 6.5.1. Since the parameter τ does not depend on energy, the values for each SiPM are taken from the Filter Wheel combination $(FW_1, FW_1) = (6, 7)$, that provided the most stable fits (Fig. 6.22, right). The few points that appear to be far away from the bulk of the distribution are addressed separately one by one. The parameter a cannot be studied as a function of the FW_1, since the energy deposited by the laser is not uniform among all the 1296 SiPMs. For each SiPM we plot the value of a versus the measured energy of the first pulse, as shown in Fig. 6.23. The six Filter Wheel combinations $(FW_1, FW_2) = (5 \cdots 10, 7)$ are considered for this study. The values of a for each SiPM are fit with a linear function. The linearity is expected from the Monte Carlo Simulations of the previous section. The parameter p0 (intercept) and p1 (slope) are at first left free to float, and their distributions are

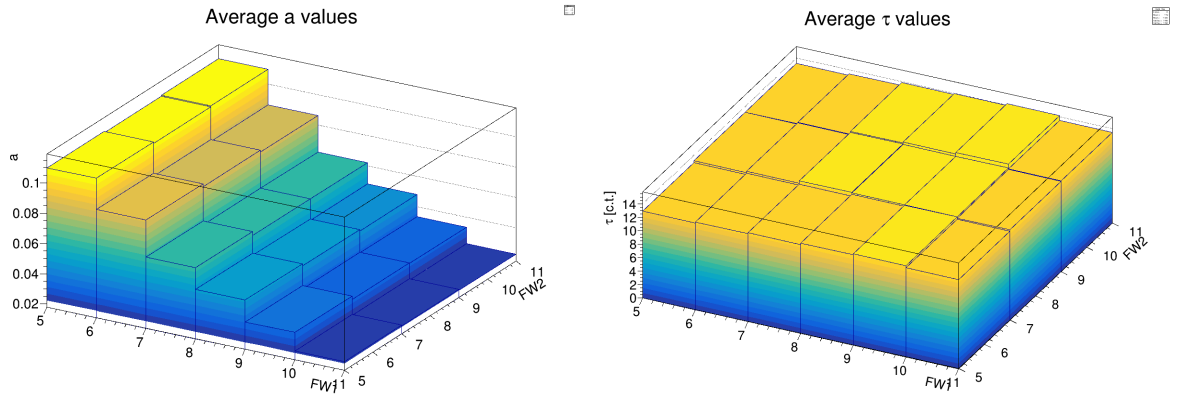

Figure 6.21: Lego plots of the average values of a (left) and τ (right) with respect to FW_1 and FW_2.

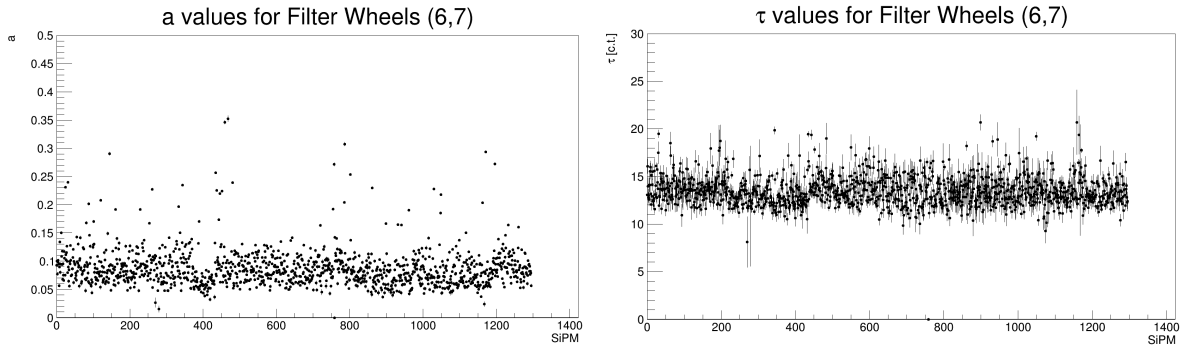

Figure 6.22: Values of a (left) and τ for each SiPM for the Filter Wheel combination (6,7).

shown in Fig. 6.24. The intercept distribution is compatible with zero, with a mean of -0.27% and a standard deviation of 0.36%. The distribution of the slopes shows a peak centered at $\sim$ 4.5%/GeV and some SiPMs distributed as a tail on the right. Since the parameter p0 is compatible with value zero, the linear fits are performed again but now fixing $p0 = 0$. Figure 6.25 shows the two distributions of the slope before (left) and after (right) fixing p0. The change is small, with the mean value shifting from 4.8%/GeV to 4.6%/GeV. Finally, figure 6.26 the two linear fits are shown for one particular SiPM.

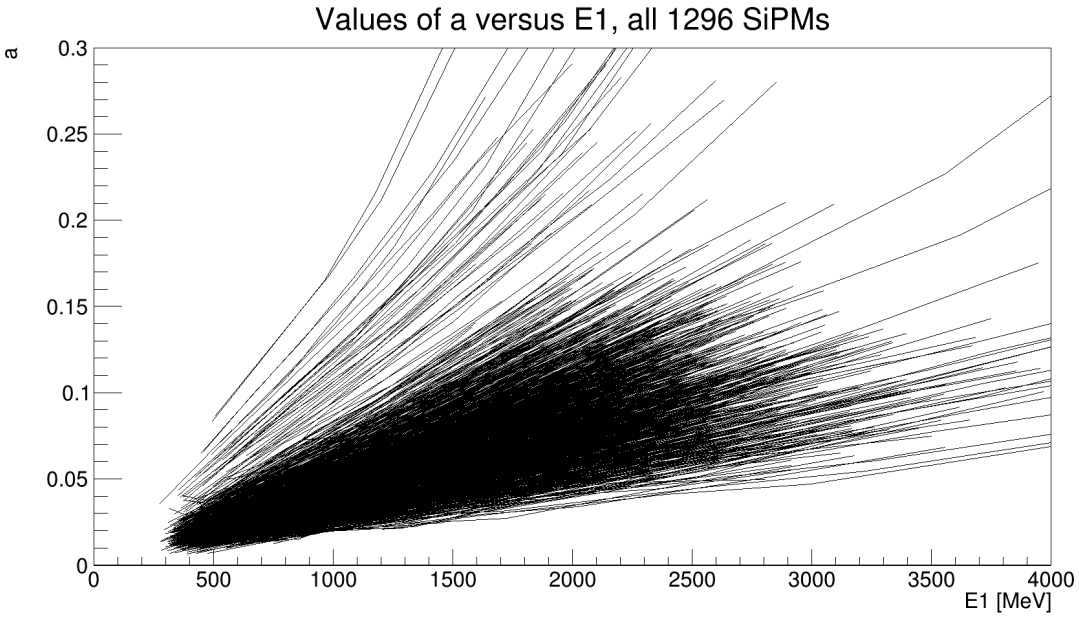

Figure 6.23: This graph shows the parameter a versus the energy of the first pulse, with the values taken from the Filter Wheel combinations that have filter 7 for the second pulse. 1296 lines are drawn, one for each SiPM.

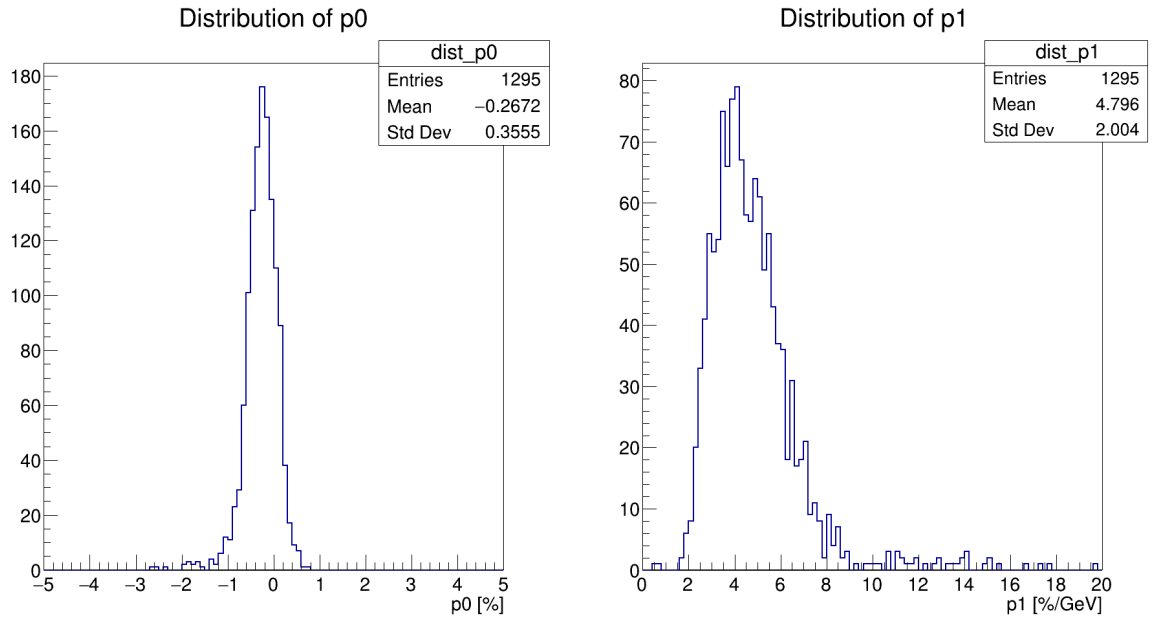

Figure 6.24: Distributions of the intercept (left) and the slope (right) of the linear fit applied to the values of a versus the energy of the first pulse. The mean value of the intercept is compatible with zero.

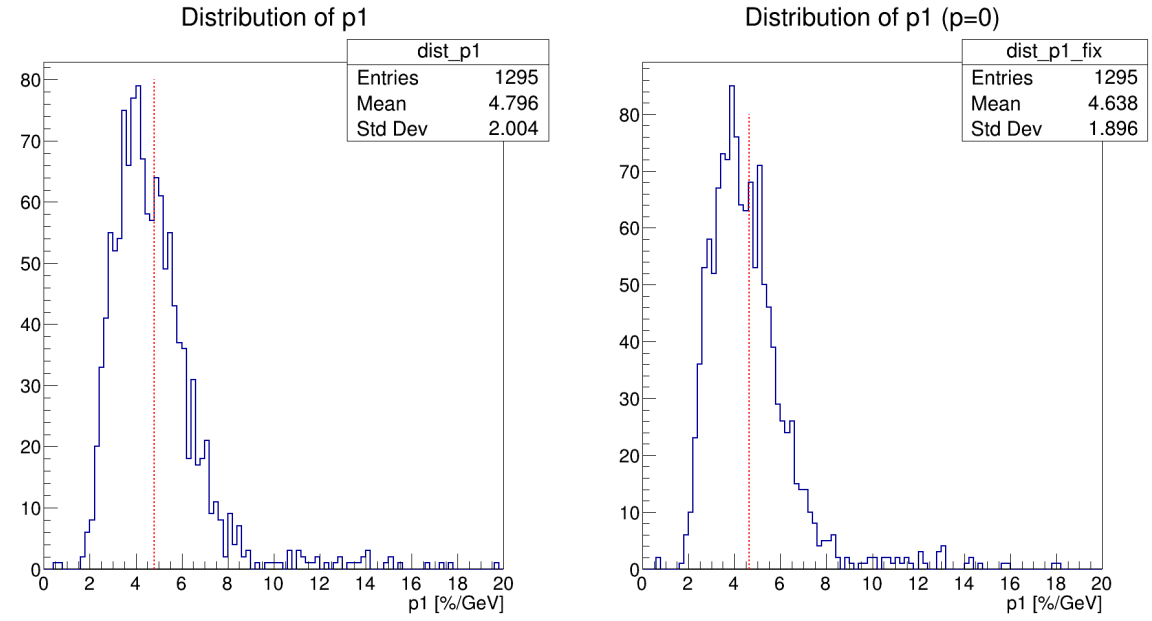

Figure 6.25: Distributions of the slope of the linear fits with a floating (left) and fixed (right) intercept.

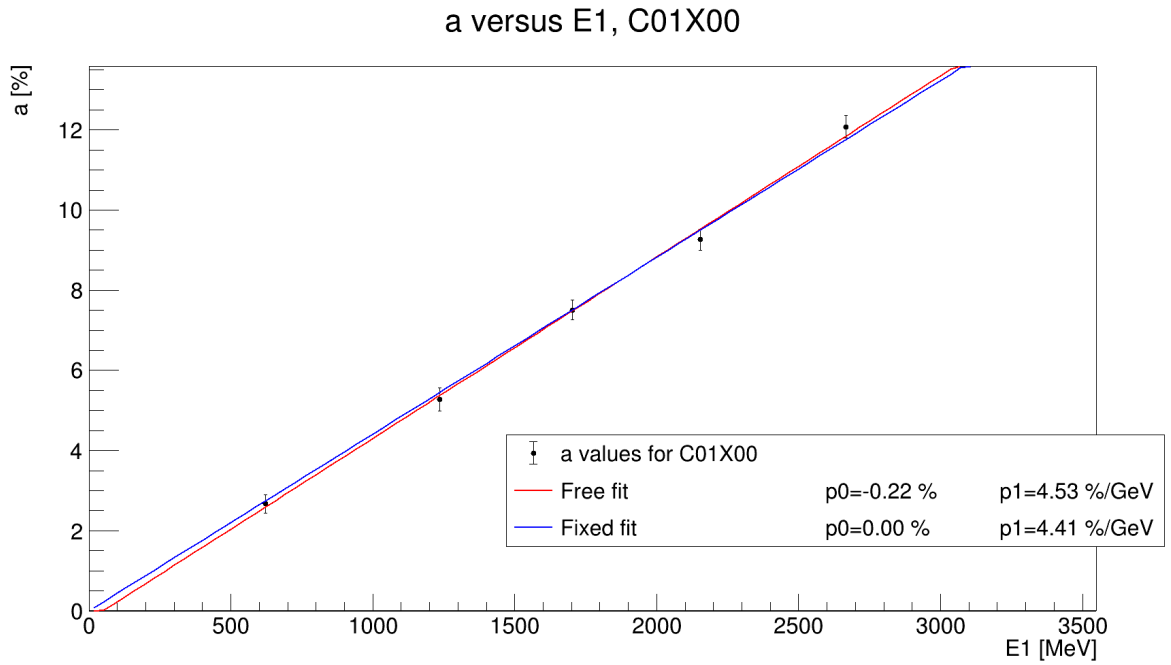

Figure 6.26: The two linear fits applied to one particular SiPM: calorimeter 1, crystal 0.

6.6 Final application to the official dataset

The STDP correction has been applied to the official *60h* dataset. Similarly to what is described in section 6.4, when two signals are produced in the same SiPM in the time window [5,75] ns, the energy of the second signal is corrected with the formula:

$$E_2' = \frac{E_2}{G(\Delta t; E_1)} \tag{6.9}$$

with the gain defined as:

$$G(\Delta t; E_1) = 1 - p_1 \cdot E_1 \cdot e^{-\Delta t/\tau} \tag{6.10}$$

where E_1 is the energy of the first signal, τ is the recovery time of the SiPM, and p_1 is the slope of the linear fit of a versus E_1 for that SiPM as found in section 6.5. After the STDP correction, the histogram of positron counts versus time is constructed with the T-Method technique: only the positrons with $E > 1.7$ GeV are considered. Figure 6.27 shows this histogram (wiggle plot) in logarithmic scale. Every bin is 149.2 ns wide: this value corresponds to the cyclotron period. A function with five parameters is fitted from 30 μs to 650 μs and shown on top. The 5-Parameter function is

$$N(t) = N_0 e^{-\frac{t}{\gamma\tau}} \left[1 + A\cos(\omega_a t + \phi)\right] \tag{6.11}$$

The analysis on the 60h dataset reported here was performed in collaboration with the European analysis team, one of the six independent groups contributing to the ω_a measurement of the experiment [75]. Due to a blinding procedure, the ω_a frequency returned by the fit is actually an adimensional parameter R defined as the fractional offset, in ppm, from a given and unknown reference value. The residual of the histogram with respect to the fitted function is then analyzed with a Fast Fourier Transform (FFT) technique, that serves to identify and quantify the oscillation frequencies that the fit is not addressing. Figure 6.28a shows this FFT analysis for the 5-Parameter function: the largest peak corresponds to the expected radial CBO frequency. The results from this fit are given in table 6.3.

Adding three corrections to the wiggle function, namely the radial CBO, the vertical waist and the lost muons correction, we obtain the following 13-Parameter function as

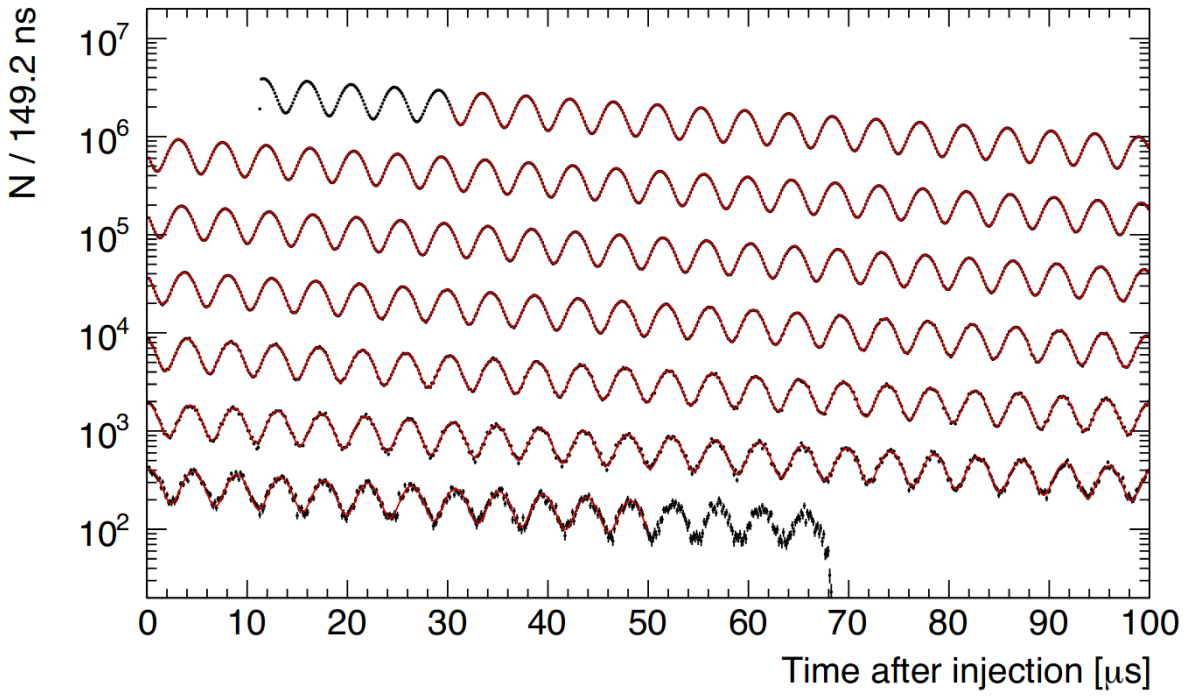

Figure 6.27: Wiggle plot of the 60h dataset for the T-Method. The histogram is wrapped around every 100 μs for aesthetic purposes.

Parameter	Value	Uncertainty
N_0 $[1 \cdot 10^6]$	3.54935	$205 \cdot 10^{-3}$
$\gamma\tau$ [μs]	64.356	$2.10 \cdot 10^{-3}$
A	0.36434	$4.28 \cdot 10^{-5}$
R [ppm]	-44.1541	1.34
ϕ [rad]	2.0913	$2.19 \cdot 10^{-4}$

Table 6.3: Results from the 5 parameter fit [75].

described in section 3.4.2:

$$\begin{aligned} N(t)^{13par} = N(t)^{5par} &\cdot \left[1 - e^{-t/\tau_{CBO}} A_{CBO} \cos(\omega_{CBO} t + \phi_{CBO})\right] \\ &\cdot \left[1 - e^{-t/\tau_{VW}} A_{VW} \cos(\omega_{VW} t + \phi_{VW})\right] \\ &\cdot \left[1 - K_{LM} \cdot J(t)\right] \end{aligned} \tag{6.12}$$

The function $J(t)$ is an estimation of the number of observed lost muons at a given time, evaluated from the same dataset. The parameters written in Eq. 6.12 are 14, but the

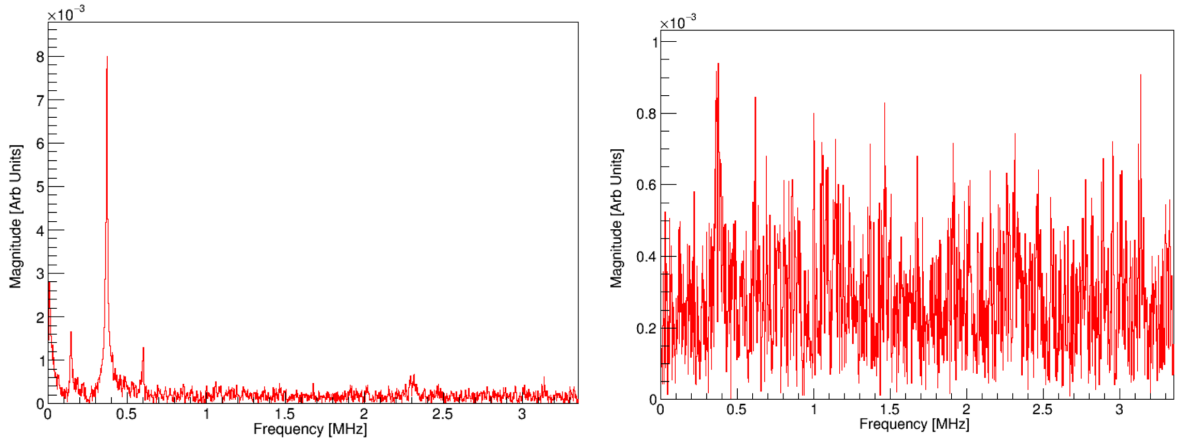

(a) (b)

Figure 6.28: Fast Fourier Transform of the residual between the fitted function and the histogram of Fig. 6.27. On the left the 5-Parameter fit, on the right the 13-Parameter fit.

parameter τ_{VW} is fixed at the value

$$\tau_{VW} = \tau_{CBO} \frac{\omega_{CBO}}{\omega_{VW}} \tag{6.13}$$

The reason is that the vertical oscillation is difficult to measure, because its lifetime is shorter than the radial CBO lifetime and dies out in $\simeq 60$ μs. The number of free parameters is then 13, and their fitted values are listed in table 6.4. Figure 6.28b shows the FFT of the residuals of the 13-Parameter fit, and the larger peaks are not visible anymore. Some improvements can still be achieved with more corrections, but they are not discussed here.

The effect of the Short-Time-Double-Pulse correction on the parameter R is now investigated. To evaluate the effect of the STDP on the parameter R, the gain correction $G(\Delta t)$ is multiplied by an artificial factor, ranging from 0 to 2, and applied to the data. After the reconstruction, the 13-parameter fit is repeated and the new R value evaluated. Fig. 6.29 shows the behavior of ΔR as a function of the multiplier. A linear trend is visible, with an effect on R of ~ 28.6 ppb per multiplier. In particular, the difference between no correction and nominal STDP correction is 20 ppb (leftmost point in the plot). Note that, although negligible with respect to the statistical error for this subsample, a shift of 20 ppb corresponds to the full admitted budget for the gain calibration error (see Table 4.1), thus its application will become fundamental once the full statistics will be collected.

Parameter	Value	Uncertainty
N_0 $[1 \cdot 10^6]$	3.57407	$918.5 \cdot 10^{-3}$
$\gamma\tau$ $[\mu s]$	64.4406	$3.77 \cdot 10^{-3}$
A	0.36436	$4.335 \cdot 10^{-5}$
R [ppm]	-42.7109	1.3416
ϕ [rad]	2.0910	$2.20 \cdot 10^{-4}$
τ_{CBO} $[\mu s]$	158.598	12.1348
A_{CBO} $[1 \cdot 10^{-3}]$	4.42	0.16
ω_{CBO} [rad/μs]	2.3271	$5.10 \cdot 10^{-4}$
ϕ_{CBO} [rad]	2.929	0.038
A_{VW} $[1 \cdot 10^{-3}]$	1.92	0.44
ω_{VW} [rad/μs]	14.399	0.015
ϕ_{VW} [rad]	2.75	0.66
K_{LM} $[1 \cdot 10^{-3}]$	12.55	0.45

Table 6.4: Results of the 13-Parameter fit.

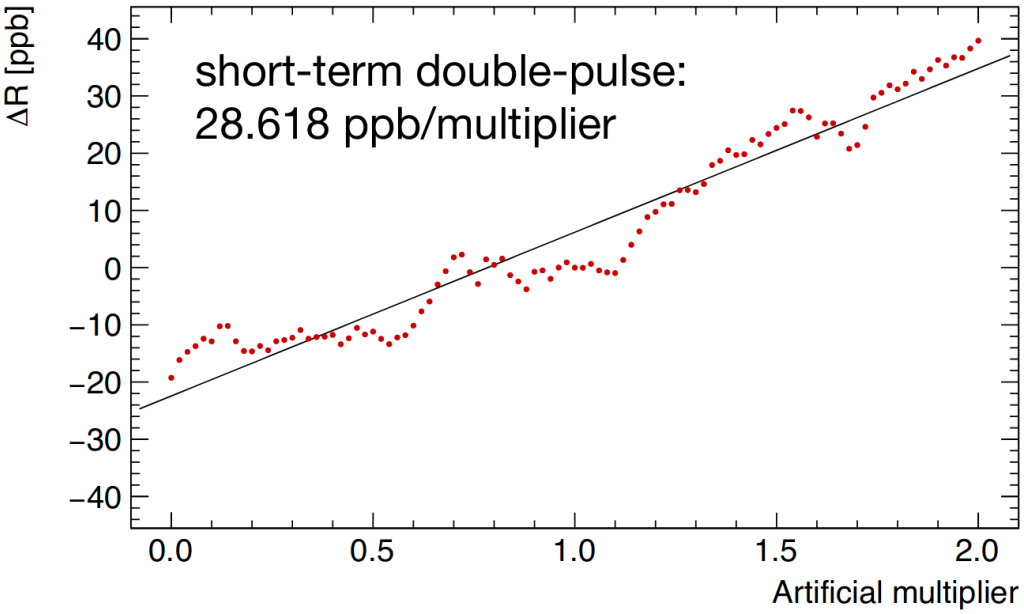

Figure 6.29: Scan of the STDP correction effect on the R value, varying an artificial factor that scales the STDP gain functions [76]. A factor < 1 means that the gain correction is reduced, while for values > 1 is enhanced. A linear fit shows a slope of 28.6 ppb per multiplier.

The shift on R due to a wrong, or missing, STDP correction is also coupled to the fit start time. Figure 6.30 shows the variation on R caused by the STDP correction at different

starting times for the wiggle fit. The difference is evaluated with respect to the nominal correction (black points). An oscillation corresponding to the ω_a frequency is visible for no correction applied (blue) and for a doubled correction (red). This is expected, since the number of positrons corrected by the STDP is dependent on the detected positron rate, which in turn is correlated with the spin direction, as high energy positrons are emitted mostly in the forward direction, and thus to the anomalous precession frequency. Again, the difference between correction and no correction at the typical starting value of 30 μs is 20 ppb.

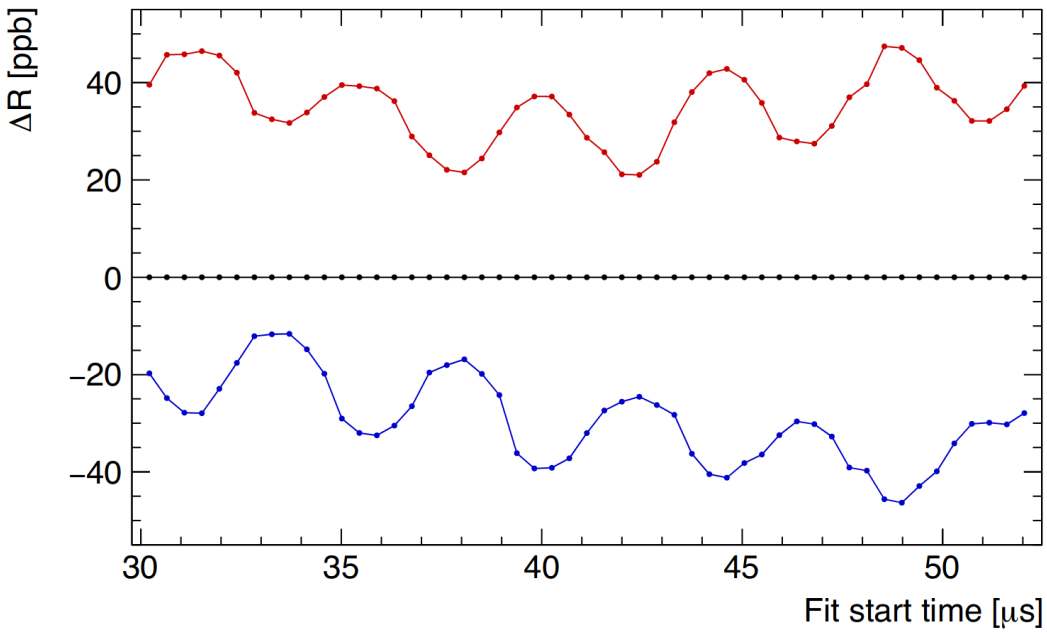

Figure 6.30: Scan of the STDP correction effect on the fit start time [76]. The blue curve corresponds to no STDP correction applied, while the red curve shows the effect of a doubled correction. The values are compared to the nominal correction (black).

In conclusion, the Short-Time Double-Pulse correction evaluated with the laser calibration system has been applied to the official reconstruction with success. In particular, its effect on the very recent analysis of the 60h dataset is visible at the 20 ppb level on the ω_a measurement.

Conclusions

A precise measurement of the muon anomalous magnetic moment a_μ is a very sought-after quantity, given the discrepancy of 3.4 σ measured by the E821 experiment at BNL with respect to the Standard Model prediction. The new *Muon g-2* (E989) experiment at Fermilab (FNAL) aims to investigate this discrepancy by reducing the experimental error by a factor 4, with a final goal of 140 ppb. This error is the quadrature sum of the statistical error of 100 ppb and an equal systematic error of 100 ppb. In particular, the measurement of the anomalous magnetic moment implies the measurement of two values: the anomalous precession frequency of the muon ω_a and the proton Larmor frequency ω_p, when the particles are placed in an uniform magnetic field. These two quantities will be measured with an expected systematic error of 70 ppb each. The measurement of ω_a involves a system of 24 calorimeters, each one composed of a 6 by 9 array of PbF_2 crystals coupled with silicon photomultipliers (SiPM). One of the factors that contribute to the 70 ppb systematic uncertainty of the ω_a measurement is the gain stability of the SiPMs. A new Laser Calibration System is used to monitor such fluctuations, granting a stability level of 10^{-4} both in the short and long time scales. The systematic error budget relative to the gain will be then reduced with respect to the E821 experiment from 120 ppb to 20 ppb. In this thesis, two analysis have been discussed, both of them making use of the Laser Calibration System.

The first one is a time synchronization of the 1296 SiPMs. The ω_a measurement involves the detection of the decay positrons in the calorimeters, that have the job to measure the energy of the particle and its time of arrival. It is therefore important to have all the SiPMs synchronized in order to make use of all calorimeters together. This analysis has been described in chapter 5.
With the use of a laser pulse at the beginning of each muon fill, and the signals produced by muons that are lost from the storage region, it is possible to determine a relative synchronization of all the SiPMs at the 100 ps level, only being limited by the time spread of the electromagnetic showers within a calorimeter. This value is much smaller

than the sampling frequency (800 MHz, that is one sample every 625 ps), so a successful synchronization is achieved.

The second study of this work, described in chapter 6, is a measurement of the gain response of the SiPMs to signals closer than 100 ns in time. After the detection of a signal, the SiPM sensitive pixels recover with a characteristic lifetime of $\sim$15 ns. If another signal is detected after less than 5-6 lifetimes, many pixels still have to recover, so the measured energy is lower than the true value. This analysis probes this effect using a new appositely-built operating mode of the Laser Calibration System called *Short Time Double Pulse*. The gain is studied for each SiPM using couples of laser pulses fired at various delays and with different intensities. A preliminary Monte Carlo simulation has also been conducted to predict the behavior of the SiPMs. The gain correction obtained has been then applied to a dataset containing beam data acquired in March 2018 during a period of 60 hours. The effect of this STDP correction on the positron data has been investigated, and results in a visible shift of the ω_a value at the 20 ppb level. At this moment, the statistical error on ω_a is still at the 1.3 ppm level.

Acknowledgments

At the end of this thesis work, I would like to thank many important people. First of all, thanks to Prof. Stefano Zucchelli that assisted me in this final step of the degree, and that made this work possible. My warm thanks to Prof. Marco Incagli, that guided me during these months, correcting and teaching me what a physicist is. Without his faith in me and his support I would not be here now. Thanks to all the Italian team of the experiment, in particular to Matthias and Anna that always kindly answered my uncountable questions.
A huge thanks to my family, that always supported me and never let me lack anything, even if I am a "girandolone". Thanks to my friends of the *Band of Physicists*, with whom I always shared happily the joyful and stressful moments of these years of study. Last but not least, a profound thank you goes to my love and astro-mate Martina, who is an essential piece in my life, with whom I share every beauty of this world and of the cosmos, and who really believes in me.

———— ○ ————

Alla fine di questo lavoro di tesi, vorrei ringraziare molte persone importanti. Innanzitutto, un grazie va al Prof. Stefano Zucchelli che mi ha assistito in questa fase finale della laurea e che ha reso questo lavoro possibile. Un sentito grazie al Prof. Marco Incagli, che mi ha guidato in questi mesi, correggendomi e insegnandomi il mestiere di fisico. Senza la sua fiducia e il suo supporto non sarei arrivato a questo punto. Grazie a tutto il team italiano dell'esperimento, in particolare a Matthias e Anna che hanno sempre risposto alle mie innumerevoli domande.
Un grande grazie alla mia famiglia, che mi ha sempre supportato e non mi ha mai fatto mancare nulla, anche se sono sempre un "girandolone". Grazie agli amici della *Band of Physicists*, coi quali ho sempre condiviso felicemente i momenti di allegria e quelli di stress di questi anni di studio. Infine, un profondo grazie va alla mia Martina, che è un tassello davvero importante nella mia vita, mi è vicina e mi supporta sempre, e con la quale condivido tutte le bellezze di questo mondo e dell'universo.

Bibliography

[1] W. Gerlach and O. Stern: *Zeitschrift für Physik 9, 353* (1922).

[2] I. Estermann, O. Simpson and O. Stern: *Phys. Rev. 52, 535* (1937).

[3] P. Kusch and H. Foley: *Phys. Rev. 74, 250* (1948).

[4] R. Feynman: *The Character of Physical Law*, 1st ed. (MIT Press, Cambridge, 1965).

[5] T. Aoyama, M. Hayakawa, T. Kinoshita, and M. Nio: *Phys. Rev. D 91, 033006*, 2015.

[6] T. Aoyama, M. Hayakawa, T. Kinoshita, and M. Nio: *Phys. Rev. D 96, 019901*, 2017.

[7] R. VanDyck, P. Schiwinberg and H. Dehmelt: *Phys. Rev. Lett. 59, 26* (1987).

[8] Particle Data Group: *Phys. Rev. 38, 090001*, 2015.

[9] T. Kinoshita and W. B. Lindquist: *Phys. Rev. Lett. 47, 1573*, 1981.

[10] G. W. Bennett et al. [Muon g-2 Collaboration]: *Phys. Rev. D 73 072003*, 2006.

[11] M. Davier, S. Eidelman, A. Hocker and Z. Zhang: *hep-ph/0208177*.

[12] M. Acciarri et al., L3 Collaboration: *Phys. Lett. B434, 169*, 1998.

[13] M. A. Samuel, G.-W. Li and R. Mendel: *Phys. Rev. Lett. 67, 668*, 1991.

[14] S. Gasiorowicz and J. L. Rosner: *Am. J. Phys. 49, 954*, 1981.

[15] J. Grange et al.: *Muon (g-2) Technical Design Report*, 2015.

[16] D. Hanneke, S. Fogwell Hoogerheide, and G. Gabrielse.: *Phys. Rev. A, 83:052122*, 2011.

[17] F. Jegerlehner and A. Nyffeler: *The Muon g-2. Phys. Rept., 477:1–110*, 2009.

[18] T. Aoyama, M. Hayakawa, T. Kinoshita, and M. Nio, *Phys. Rev. Lett. 109, 111808*, 2012.

[19] M. Knecht: *The Muon Anomalous Magnetic Moment, arXiv:1412.1228v1*, 2014.

[20] Hagiwara et al.: *JPG 38, 085003*, 2011.

[21] P. J. Mohr, B. N. Taylor and D. B. Newell, CODATA Group: *Rev. Mod. Phys 84, 1527*, 2012.

[22] R. Bouchendira et al.: *Phys. Rev. Lett. 106,080801*, 2001.

[23] R. Jackiw and S. Winberg: *Phys. Rev. D5, 2396*, 1972.

[24] C. Gnendiger, D. Stöckinger and H. Stöckinger-Kim: *Phys. Rev. D88 053005*, 2013.

[25] M. Davier et al.: *EPJ C71, 1515*, 2011.

[26] V.W. Hughes: *J. Phys. G 29 181*, 2003.

[27] A. Czarnecki and W. J. Marciano: *Muon anomalous magnetic moment: A harbinger for "new physics", Phys. Rev. D, 64:013014*, 2001.

[28] P. Fayet: *Phys. Re. D75 115017*, 2007.

[29] D. Tucker-Smith and I. Yavin: *Phys. Rev. D83 101702*, 2011.

[30] T. Lee and C. Yang: *Phys. Rev. 104, 254*, 1956.

[31] C. Wu et al.: *Phys. Rev. 105, 1414*, 1957.

[32] R. Garwin, L. Lederman and M. Weinrich: *Phys. Rev. 105, 1415*, 1957.

[33] D. Hutchinson et al.: *Phys. Rev. Lett. 131, 1315*, 1963.

[34] W. Louisell et al.: *Phys. Rev. 91, 475*, 1953.

[35] G. Charpak et al.: *Phys. Rev. Lett. 6, 128*, 1961.

[36] J. Bailey et al.: *Nuovo Cimento Soc. Ital. Fis. A9, 369*, 1972.

[37] J. Aldins et al.: *Phys. Rev. Lett. 23, 441*, 1969.

[38] M. Gourdin and E. de Rafael: *Nucl. Phys. B10, 667*, 1969.

[39] V. Auslander et al.: *Phys. Rev. 91, 475*, 1953.

[40] J. Augustin et al.: *Phys. Lett. 28B, 517*, 1969.

[41] D. Hutchinson et al.: *Phys. Rev. Lett. 24, 1254*, 1970.

[42] R. D. Voe et al.: *Phys. Rev. Lett. 26, 213(E)*, 1971.

[43] K. Crowe et al.: *Phys. Rev. D 5, 2145*, 1972.

[44] CERN Muon Storage Ring Collaboration, J. Bailey et al.: *Phys. Lett. B67, 225*, 1977.

[45] T. Kinoshita, B. Nizic and Y. Okamoto: *Phys. Rev. Lett. 52, 717*, 1984.

[46] H. N. Brown et al.: *Revised rates for muon storage in the g-2 ring, Muon g-2 Internal Note No. 185*, 1994.

[47] Muon g-2 Collaboration (G. W. Bennet et al.): *Phys. Rev. D73, 072003*, 2006.

[48] T. P. Gorringe, D. W. Hertzog: *Precision Muon Physics, arXiv:1506.01465v1*, 2015.

[49] A. Anastasi et al: *The Calibration System of the new g-2 experiment at Fermilab, Nucl. Instrum.Meth. A824 716-717*, 2016.

[50] O. Rifki: *The muon anomalous magnetic moment: a probe for the Standard Model and beyond, Report approved for the H.L.Dodge Department of Physics and Astronomy*, 2014.

[51] M. E. Shenk: *A straw tube tracking detector for the new muon g-2 E989 experiment*, 2014.

[52] D. Hertzog: *Next Generation Muon g-2 Experiments, arXiv:1512.00928v1*, 2015.

[53] R. Carey et al.: *FERMILAB-PROPOSAL-0989*, 2009.

[54] A. Yamamoto et al.: *The superconducting inflector for the BNL g-2 experiment, Nucl. Instrum. Meth., A491:23–40*, 2002.

[55] W. Gohn: *Data Acquisition for the New Muon g-2 Experiment at Fermilab, J. Phys. Conf. Ser.*, 2015.

[56] A. T. Fienberg: *Measuring the Precession Frequency in the E989 Muon g-2 Experiment, PhD thesis*, 2019.

[57] J. Kaspar et al.: *Design and performance of SiPM-based readout of PbF 2 crystals for high-rate, precision timing applications.*, JINST, 12(01):P01009, 2017.

[58] Peter J. Mohr, David B. Newell, and Barry N. Taylor.: *CODATA recommended values of the fundamental physical constants: 2014.*, Rev. Mod. Phys., 88:035009, Sep 2016.

[59] M. Sorbara: *Analysis of the anomalous precession frequency in the Muon $g-2$ (E989) Experiment at Fermilab: the Lost Muons correction*, Master thesis, 2018.

[60] A. Driutti et al.: *The Calorimeter Gain Sag(a) Chapter 3 - the Tests, E989 internal note*, 2018.

[61] A. Anastasi: *The Calibration System of the E989 Experiment at Fermilab, PhD Thesis*, 2016.

[62] A. Anastasi et al.: *The Muon g-2 laser calibration system*, 2016.

[63] G. Venanzoni: *The New Muon g-2 experiment at Fermilab (E989), (HEP-EPS 2015)*, 2015.

[64] E. Rossi: *The laser calibration system of the muon g-2 experiment at Fermilab*, Master thesis, 2016.

[65] M. Karuza et al.: *The Fermilab Muon g-2 experiment: laser calibration system, JINST 12 C08019*, 2017.

[66] K. S. Khaw: *Recon West update: a tale of time and energy, E989 internal note n. 11055-v7.*

[67] J. Stapleton: *Crystal Timing Calibration, E989 internal note n. 9182-v1.*

[68] R. Bjorkquist: *Crystal timing shift systematic study, E989 internal note n. 2274-v1.*

[69] J. Kaspar et al.: *Design and performance of SiPM-based readout of PbF_2 crystals for high-rate, precision timing applications, JINST 12 no.01, P01009*, 2017.

[70] S. Mastroianni: *The Readout Controller for the Calibration System of the Muon g-2 Experiment, IEEE Transactions on Nuclear Science, vol.65, no.4, pp.1033-1039*, 2018.

[71] C. Green, J. Kowalkowski, M. Paterno, M. Fischler, L. Garren and Q. Lu: *The Art Framework, J. Phys. Conf. Ser.396, 022020*, 2012.

[72] K. S. Khaw: *Muon g-2 reconstruction and analysis framework for the muon anomalous precession frequency, J.Phys.Conf.Ser. 1085 no.3, 032039*, 2018.

[73] P. Girotti, M. Smith: *E989 Internal Note 157: Short-Time Double Pulse: Initial Tests*, 2018.

[74] A. T. Fienberg et al.: *Studies of an array of PbF2 Čerenkov crystals with large-area SiPM readout, Nuc. Ins. and Met. A, 783*, 2014.

[75] E. Bottalico et al.: *The 60h dataset relative unblinding; fitting procedure for waeuropa, E989 internal note*, 26 Feb 2019.

[76] D. A. Sweigart: *Preliminary Analysis of the 60 h. Data Set, E989 internal note*, 24 Feb 2019.